

DISSERTATION

submitted to the

Combined Faculty of Natural Sciences and Mathematics
of Heidelberg University, Germany

for the degree of

Doctor of Natural Sciences

Put forward by

PHILIPP HOTTINGER

born in: LANGEN (HESSEN), GERMANY

Oral examination: May 23th, 2023

Integrated Tip-Tilt Sensing for Single-Mode Fiber Coupling

Referees: Prof. Dr. Andreas Quirrenbach
Prof. Dr. Thomas Henning

Abstract

This thesis presents the development and on-sky tests of the novel Microlens-Ring Tip-Tilt (MLR-TT) sensor. The sensor consists of a micro-lens ring (MLR) that is printed directly on the face of a fiber bundle with a central single-mode fiber (SMF) accepting the light almost unclipped if the beam is aligned. The edge of the beam, however, is refracted by the MLR to couple into six surrounding multi-mode fibers (MMFs). Detecting the flux in these sensor fibers allows reconstruction of the beam position, i.e. the tip and tilt aberrations of the wavefront.

The lenses are manufactured in collaboration with Karlsruhe Institute for Technology (KIT) with state-of-the-art two-proton polymerization, a novel technology that allows the fabrication of very precise and freeform lenses. The sensor is integrated with the instrument's fiber link and features a small physical size of 380 μm . This novel integration of a sensor into existing components reduced opto-mechanical footprint and complexity, as well as reducing non-common path aberrations (NCPAs) to a bare minimum.

This thesis describes the various steps that were part of this development, starting with designing, optimizing, and characterizing the sensor itself, setting up a corresponding laboratory environment, and developing a control system for on-sky testing. The system is tested on-sky with iLocator fiber coupling front-end (acquisition camera) at the Large Binocular Telescope (LBT). It was found that principle reconstruction is possible but the observed accuracy is $\sim 0.19 \lambda/D$ both for tip and for tilt. With this accuracy, it was not possible to improve the resulting SMF coupling efficiency. A strong correlation between sensor accuracy and the instantaneous Strehl ratio (SR), i.e. residual adaptive optics (AO) aberrations, is found. Additionally, the corresponding power spectral density (PSD) reveals that most of the reconstruction inaccuracy occurs in low temporal frequencies. This suggests that the dominating limitations of the accuracy of the MLR-TT sensor arise from residual AO aberrations and the false signal they introduce in the sensor.

These findings are discussed in detail and the future prospects of further analysis and development are outlined in the context of the most beneficial application environment.

Zusammenfassung

In dieser Arbeit wird die Entwicklung des neuartigen Microlens-Ring Tip-Tilt (MLR-TT) Sensors vorgestellt und die Ergebnisse dessen Tests am Teleskop präsentiert. Der Sensor besteht aus einem Mikrolinsenring (MLR), der direkt auf die Oberfläche eines Faserbündels aufgedruckt ist, wobei eine zentrale Singlemode-Faser (SMF) das Licht nahezu ungestört aufnimmt, wenn der Teleskopstrahl korrekt ausgerichtet ist. Der Rand des Strahls wird durch die Linsen gebrochen, um das Licht in sechs umliegende Multi-Mode-Fasern (MMF) einzukoppeln. Das Signal aus diesen sechs MMF kann dann genutzt werden um die Position des Strahls zu rekonstruieren.

Die Linsen wurden in Zusammenarbeit mit dem Karlsruher Institut für Technologie (KIT) mittels modernster Zwei-Protonen-Polymerisation hergestellt, einer neuartigen Technologie, die die Herstellung von sehr präzisen und frei geformten Linsen ermöglicht. Der Sensor ist in die Faserverbindung des Instruments integriert und weist eine geringe Größe von <1 mm auf. Diese neuartige Integration eines Sensors in bestehende Komponenten reduziert die opto-mechanischen Komplexität und Größe des Systems und vermeidet die sogenannten non-common path Aberrationen auf ein Minimum.

Diese Arbeit beschreibt die verschiedenen Schritte, die Teil dieses Projekts waren, beginnend mit dem Design, der Optimierung und der Charakterisierung des Sensors, dem Aufbau einer entsprechenden Laborumgebung und der Entwicklung eines Kontrollsystems für die Tests. Das System wurde am Teleskop mit dem iLocator Faserkopplungs Front-End des in Entwicklung stehenden iLocator Spektrographen am Large Binocular Telescope (LBT) getestet. Es wurde festgestellt, dass eine prinzipielle Rekonstruktion der Strahlposition möglich ist, aber die beobachtete Genauigkeit in jeder Raumrichtung nur $\sim 0.19 \lambda/D$ beträgt. Mit dieser Genauigkeit war es nicht möglich, den SMF-Einkopplungswirkungsgrad zu verbessern. Es wurde eine starke Korrelation zwischen der Sensorgenauigkeit und dem entsprechenden Strehl-Verhältnis (SR), d.h. den Restabbildungsfehler der adaptiven Optik (AO), festgestellt. Darüber hinaus zeigt die entsprechende spektrale Leistungsdichte (PSD), dass der größte Teil der Ungenauigkeit der Rekonstruktion bei niedrigen Zeitfrequenzen auftritt. Dies deutet darauf hin, dass die vorherrschenden Einschränkungen der Genauigkeit des MLR-TT-Sensors aus den verbleibenden AO-Aberrationen und dem Störsignal, das sie in den Sensor einbringen, resultieren.

Diese Ergebnisse werden im Detail diskutiert und die zukünftigen Aspekte der weiteren Analyse und Entwicklung werden im Kontext der nützlichsten Anwendungsumgebung skizziert.

Contents

1	Introduction	11
1.1	Development of astronomical observations: enhancing resolution and sensitivity	11
1.2	Single-mode fibers: enabling small instruments	12
1.3	Integrated instruments: advantages and challenges	12
1.4	MLR-TT sensor: the integrated tip-tilt sensor for SMF coupling	14
2	Theoretical background of physics	17
2.1	Fundamental concepts of light propagation	17
2.1.1	Geometric propagation	17
2.1.2	Wave propagation	17
2.1.3	Fraunhofer diffraction	18
2.1.4	Diffraction of the telescope aperture	18
2.1.5	Wavefront error	20
2.2	Optical waveguides	22
2.2.1	Light propagation in MMFs	22
2.2.2	Light propagation in SMFs	25
3	Astronomical instrumentation	31
3.1	Telescope optics - basic concept and context	31
3.2	Adaptive optics - atmospheric disturbance and its correction	33
3.2.1	Atmospheric Seeing	33
3.2.2	Telescope vibrations	35
3.2.3	Wavefront sensing	35
3.2.4	Wavefront control	36
3.2.5	Controlling	37
3.3	Integrated optics - fibers & astrophotonics	37
3.3.1	Optical fibers at telescopes	38
3.3.2	SMFs at telescopes	38
3.3.3	Integrated optics in AO	40
4	Introducing MLT-TT sensor and KOOL laboratory	45
4.1	Introduction	46
4.2	Design considerations	47
4.2.1	iLocater spectrograph	47
4.2.2	Single mode fiber coupling	48
4.2.3	Tip-tilt vibrations	49

Contents

4.3	Preliminary design	51
4.3.1	Modeling	53
4.3.2	Tip-tilt correction	56
4.3.3	Manufacturing	57
4.4	KOOL: AO system testbed	58
4.5	Discussion	59
4.5.1	Comparison to prototype	61
4.6	Conclusion	61
5	Laboratory characterization and integration	65
5.1	Introduction	66
5.2	Design	68
5.2.1	Optical principle	68
5.2.2	Manufacturing	69
5.2.3	Correction	70
5.3	Results	70
5.4	Discussion	71
5.5	Conclusion	72
6	On-sky results	75
6.1	Introduction	77
6.2	Design and methods	79
6.2.1	Fiber bundle design	80
6.2.2	Lens design	80
6.2.3	Lens manufacturing	82
6.2.4	Laboratory sensor response	82
6.2.5	Signal processing	83
6.2.6	Reconstruction and calibration	83
6.2.7	On-sky integration	85
6.2.8	Simulations of on-sky results	86
6.3	Results	86
6.3.1	Sensor calibration	88
6.3.2	Closed-loop performance	89
6.3.3	Reconstruction accuracy	90
6.3.4	Impact of AO performance	92
6.3.5	On-sky sensor simulations	93
6.4	Discussion	94
6.4.1	Sensor reconstruction limitations	95
6.4.2	Loop performance	95
6.4.3	Sensor optimization	96
6.4.4	Future applications	96
6.5	Conclusion	96

7	Discussion	99
7.1	Summary	99
7.2	System overview	99
7.3	Mathematical framework	100
7.4	Reconstruction error and noise	104
7.5	Noise	106
7.5.1	Reference error	107
7.6	Latency	107
7.7	Controlling	109
7.8	Optical design	113
7.9	Co-design of the whole system	114
7.10	Project continuity	115
8	Conclusion and future prospects	117
	Publications	121
	Acknowledgments	123
	Acronyms	127
	List of figures	129
	Bibliography	137

1 Introduction

1.1 Development of astronomical observations: enhancing resolution and sensitivity

Ever since the beginning of astronomical observations, telescopes have been increasing in size. This is because the larger diameter of the telescope's primary mirror enables improved measurement quality, where the two most important enhancements are increased sensitivity as more photons are collected in the same amount of time and the reduced diffraction limit enables higher angular resolution. On telescopes with larger primary pupil size, atmospheric turbulence leads to Seeing, limiting the angular resolution to that of a ~ 20 cm diameter when working in the visible wavelength range (Rigaut, 2015). In order to reach the theoretically possible diffraction limit, modern telescopes need to be equipped with AO systems that correct for atmospheric disturbances and active optic systems that counteract mechanical and gravitational deformations. It should be noted that higher angular resolution can also be achieved with interferometry, providing a larger effective aperture. However, increased sensitivity can only be achieved with a larger pupil size or longer exposure times and enables observation of fainter targets as it increases the signal and subsequently the signal-to-noise ratio (SNR).

Both of these improvements also play a crucial role when building a spectrograph. With increasing spectral resolution, ever more light is needed for a sufficient SNR across the whole spectral range because the photons are spread out over an increasing number of pixels. This is particularly important for high-precision radial velocity observations, as this technique requires a high SNR to detect these slight spectral shifts. However, the larger telescope aperture leads to increased wavefront disturbance by sampling more atmospheric turbulence, effectively increasing the size of the observed point spread function (PSF) and introducing temporal variability. To compensate for these effects, the dispersion element of the spectrograph, usually a grating, needs to increase, and hence the size of the whole instrument.

In addition to this, larger instruments are usually associated with higher developing and manufacturing costs, which is obviously not desirable. It can also come with unwanted scaling challenges for both the hosting observatory and the instrument itself. These include mechanical and thermal stability which are particularly important in the realm of high-precision radial velocity.

1.2 Single-mode fibers: enabling small instruments

The size of a spectrograph's dispersion element and with it the size of the instrument is governed by the étendue of the optical system. With that comes a quadratic dependence with the angular width of the PSF and the diameter of the pupil. Because optical étendue is conserved, it cannot be reduced by simple re-imaging optics. However, the width of the PSF can be reduced by employing AO, reducing atmospherically induced wavefront distortions. But as the size of the PSF is reduced, temporal and chromatic variability of the PSF have a larger relative impact on the performance of the spectrograph as it can introduce variability in the centroid of the line spread function (LSF).

Optical fibers have been used in astronomical observatories for decades and have gained in importance since their first use (Heacock and Connes, 1992; Parry, 1998). They can be used to transport light from the telescope to a spectrograph at a different location, where the mechanical and thermal environment can be controlled in an easier manner.

The variability of the PSF is then observed as a variability of the intensity of the different propagation modes of the fiber. This modal noise can limit the spectral resolution of the spectrograph, especially for few-mode fibers. Traditionally, in order to reduce the impact of modal noise, the most prominent solution is the use of fiber scramblers that intentionally stimulate modal coupling, reducing both chromatic and temporal variability of the fiber output.

However, the most desirable solution would be the use of SMFs to transport light as they only have one, the fundamental, mode that can be excited. They have also the advantage that they feature the minimal possible optical étendue. Furthermore, the output of SMFs is spatially stable, removing any modal noise. This enables particularly small instruments with sizes independent of the telescope's primary mirror diameter. But in order to efficiently couple light into a SMF, the telescope beam needs to match the near-Gaussian intensity profile of the fundamental mode. This can be done with the Airy disk shape of a diffraction-limited system but to achieve this, powerful AO correction such as extreme adaptive optics (ExAO) is required that performs a particularly good wavefront correction. Especially tip-tilt variations need to be controlled because mechanical movement and vibrations of the telescope can introduce much stronger aberrations at particular frequencies than can be expected from atmospheric perturbations. Fig. 1.1 shows the degradation of the coupling efficiency compared to the residual tip-tilt aberrations at the focal plane as simulated with wave optics.

1.3 Integrated instruments: advantages and challenges

As only one mode can propagate within a SMF, the output wavefront is truly coherent and optically well defined. This enables a wide range of integrated components that manipulate the light either within optical waveguides or in a very restricted space. These integrated components, commonly referred to as photonic instruments, have a long history in the technological context of optical telecommunication. With the respective research and development being focused on the needs of this industry, they

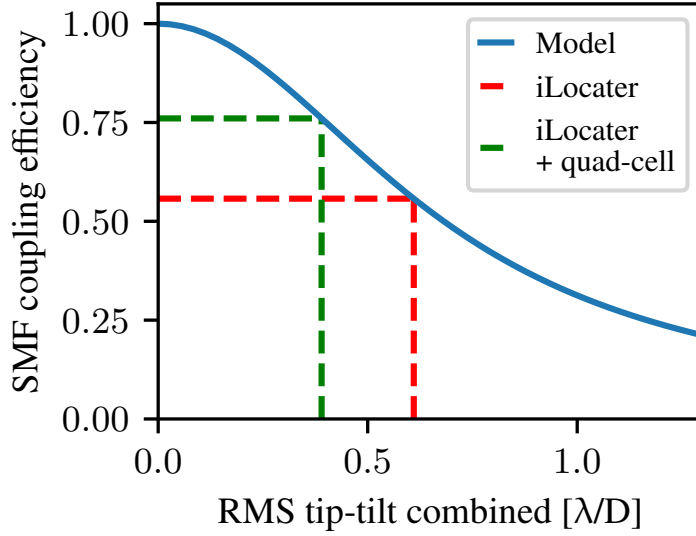


Figure 1.1: Sensitivity of SMF-coupling depending on tip or tilt.
(Reprinted from Hottinger et al., 2021)

lack the fulfillment of many requirements that are particularly important in the area of astronomical observations. This includes tight constraints on throughput, broadband wavelength coverage, and employment in the tough mechanical and thermal environment of observatories.

These photonic components used in the astronomical context, often referred to as astrophotonics, bring the possibility to enhance conventional systems as we know them today. The success and nowadays widespread use of optical waveguides, including MMFs, shows that they can benefit astronomical optical systems. Photonic components can incorporate many functionalities in a small physical domain, while the electromagnetic (EM) field is closely coupled to them, providing stability and reducing both mechanical and optical complexity. These advantages can lead to a reduction in development, manufacturing, and operating costs. Astrophotonics could potentially incorporate wavefront sensing and controlling where otherwise a complex conventional optical system would be needed. Subsequently, it can potentially enable more widespread use of these complex optical components, enabling more functionalities at observatories. The wide variety of functionalities thus brings the development of advanced instrument concepts to fruition, which would otherwise not be feasible.

1.4 MLR-TT sensor: the integrated tip-tilt sensor for SMF coupling

In this thesis, the micro-lens ring tip-tilt sensor (MLR-TT sensor) is presented, which integrates wavefront sensing with the SMF-coupling optics. It is an integrated component with its vital optical part, the micro-lens ring, sitting on top of the SMF face. The sensor's lenses simply refract misaligned light to be coupled into the MMFs that transport the wavefront sensing light to a separate detector. The general setup is presented in Fig. 1.2.

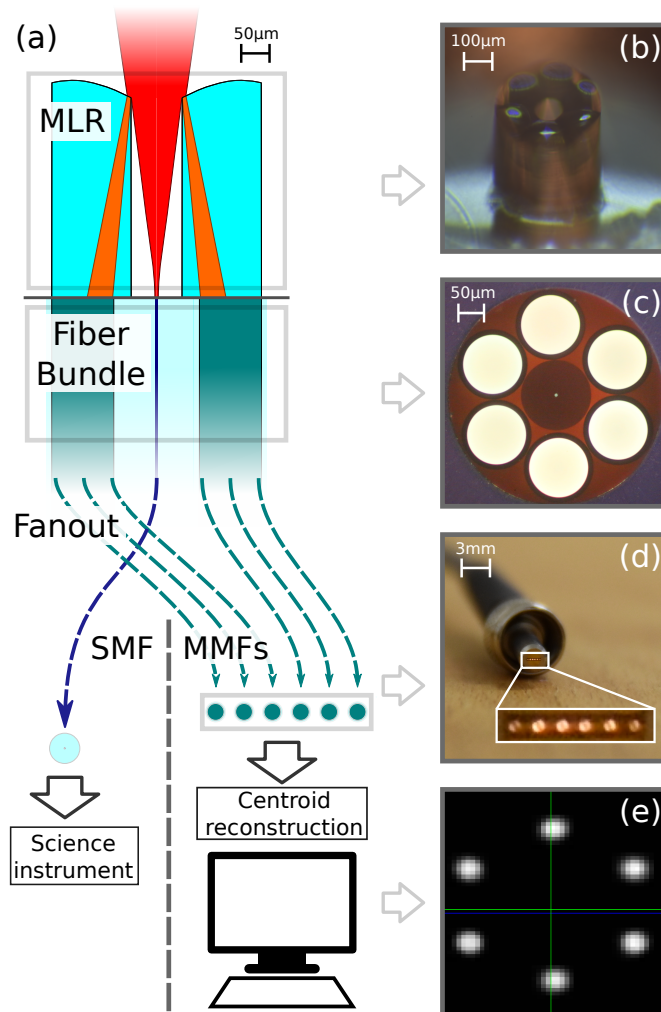


Figure 1.2: Overview of the micro-lens ring tip-tilt sensor (MLR-TT).
(Reprinted from Hottinger et al., 2021)

This is an excellent example of a novel integrated component that functions in a small physical footprint. It can replace conventional optical components such as quad cell

detectors that measure the PSF asymmetry in the focal plane or pin-hole mirrors that enable imaging of the outer edges of the PSF to reconstruct the PSF's centroid position.

The sensor provides many advantages, such as potentially providing more intrinsic stability through in situ alignment and significant reduction of NCPA effects. It is enabled by new advances in optical component manufacturing, namely the two-photon polymerization technique by nanoscale, with high accuracy and with the appropriate optical properties (Dietrich et al., 2018). This novel technology is relatively straightforward to manufacture and reliable in operation.

The MLR-TT sensor is suitable to provide functionality that new SMF-coupling approaches require but is increasingly difficult to accomplish with conventional optical components. This project focuses on the employment of the MLR-TT sensor on the LBT, an 8m-class telescope with an ExAO system. This does not necessarily mean that this is the most suitable use case for the concept but other environments such as small diffraction-limited telescopes could benefit more from the sensor or a derivative of it.

Structure of this thesis

This work gives an overview of the development of the MLR-TT sensor and the different technical aspects that were involved in the practical application on-sky. It provides an analysis of the performance and the next steps that need to be addressed for further development of the concept.

First, the *theoretical principles* of light propagation and optics are introduced in chapter 2 to set the foundations to understand the underlying physics. This includes the optics as encountered in optical waveguides and SMFs in particular. Chapter 3 then covers the instrumentation specifics that arise in the optics of telescopes, focusing on *application of AO and optical fibers*.

The following chapter 4 introduces the *concept and the design of the MLR-TT sensor* as well as the laboratory setup used for testing and development. Chapter 5 presents *laboratory test results and integration* with the iLocator spectrograph fiber coupling optics. In chapter 6 the *on-sky experiment* with the sensor is shown. The observational setup and the results are presented and interpreted.

The final chapters 7 and 8 summarize the findings and discuss the results in detail before ending this thesis with concluding remarks on the project and its future developments and prospects.

2 Theoretical background of physics

The fundamentals that are needed to understand and describe astronomical telescopes originate in basic physical principles. It is their interaction that leads to the quality and repeatability of scientific observations. First, these physical principles are outlined in Sec. 2.1, then the associated physics for fiber-based optics and photonics is introduced in Sec. 2.2 to introduce the reader to the application-specific physics employed in this work.

2.1 Fundamental concepts of light propagation

The most accurate physical description of light is the quantum mechanical treatment of photons. But in many applications, various degrees of approximation suffice to predict the behavior of optics.

2.1.1 Geometric propagation

A simple description is the *geometric approximation* that treats light as particles that propagate through space. Within an optically homogeneous medium, particularly with a constant refractive index, photons move in a straight line from their source. They will then refract or reflect on optical surfaces. The photon paths in this model are called rays; the model itself is therefore also referred to as *ray optics*. This approximation suffices for many optical systems because it is capable of accurately reconstructing the image that the optical system produces. By examining the differential path length of the rays, it is also able to approximate the phase of the resulting wavefront, just by considering the wavefront as produced by a single radiating source point to spherical direction outwards. This reveals the observed optical aberrations and can therefore be used to optimize both system layout and individual components. The simplicity of the model and the resulting computational inexpensiveness make it very useful for large and complex optical systems.

2.1.2 Wave propagation

Geometric optics treats light only as particles, but, as Young discovered in 1802 and demonstrated with his well-known double-slit experiment (Young, 1804), it also shows characteristics of wave-like behavior. This means that the propagation of light can also be approximated by Huygens' principle. The propagation of multiple waves into the free space involves the interaction between them. Thus, this leads to interference of the wave and is observed as diffraction when detecting the photons. To fully understand the

2 Theoretical background of physics

behavior of single photons, one must consider the physics of quantum mechanics, but for the observed intensity profile the wave approximation is sufficient. For this, the electric part of the EM field created by the photons is considered. The behavior of the electric field is described by the differential wave equation (Hecht, 2002)

$$\nabla^2 \psi = \frac{1}{v^2} \frac{\partial^2 \psi}{\partial t^2} \quad , \quad (2.1)$$

where ψ is the electrical field with its spatial divergence ∇ and its temporal derivative $\frac{\partial^2}{\partial t^2}$.

For different environments and with different boundary conditions, different solutions exist. In free-space propagation, a common approximation is the Fresnel-Kirchhoff diffraction equation. Although some constraints are used in this approximation, it is valid in most practical optical systems. A detailed derivation of the Fresnel-Kirchhoff equation, as well as the corresponding transformations to the following approximations, is covered in Hecht (2002).

2.1.3 Fraunhofer diffraction

Two special cases for the Fresnel-Kirchhoff diffraction are widely used. The behavior of the near-field is described by the *Fresnel diffraction* formula and covers the diffraction before the focal plane at various distances. The far-field behavior is described by *Fraunhofer diffraction* and corresponds to the diffraction pattern observed at the focal plane itself.

It is the latter, Fraunhofer diffraction, that is therefore rather important for optical systems, as it describes the transition of the EM field from the pupil to the focal plane and vice versa. The EM field distribution as described by Fraunhofer diffraction is given by,

$$\psi_{\text{Focus}}(\vec{r}, t) = \int_{\text{Aperture}} \psi_{\text{Pupil}}(\vec{r}', t) \cdot e^{-\frac{i2\pi}{\lambda}(\vec{r}' - \vec{r})} d\vec{r}' \quad , \quad (2.2)$$

where ψ_{Focus} is the EM field at the focal plane position \vec{r} by integrating the source field ψ_{Pupil} over the pupil aperture for a chromatic wave with wavelength λ . The Fraunhofer equation (eq. 2.2) can be identified as the Fourier transform, which makes it computationally very convenient. It is also the reason for the conventional name of *Fourier optics* used for the description of optical systems in the context of Fraunhofer diffraction.

2.1.4 Diffraction of the telescope aperture

To estimate the image at the focal plane of a telescope, Fraunhofer diffraction is used. In an idealized case, a monochromatic and coherent wavefront with a homogeneous intensity distribution enters the telescope and is cut into a circular top-hat distribution by the primary mirror. It then propagates through the optical path of the telescope and is eventually focused at the image plane of the telescope. The diffraction at the primary mirror acting as an aperture results in a diffraction pattern at the focal plane.

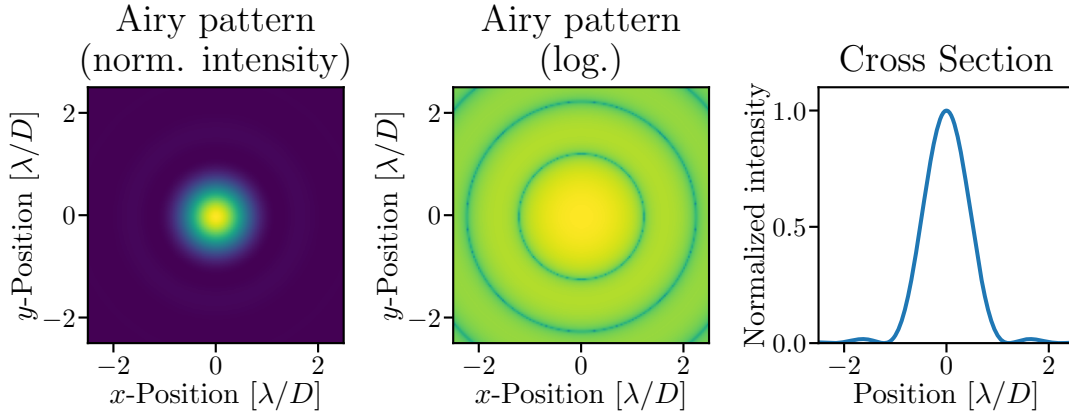


Figure 2.1: Diffraction from a circular aperture resulting in an Airy pattern in focus. **Left panel:** normalized intensity of Airy pattern; **center panel:** logarithmic scale thereof; **right panel:** cross-section of normalized intensity.

The diffraction pattern of an evenly illuminated circular aperture is described by an Airy pattern (see Fig. 2.1). This Airy pattern overlays any astronomical observation, and a point-like object will be imaged as such a pattern. The image of any source is then the convolution of the source intensity distribution with the Airy diffraction pattern.

Under realistic observation conditions, several aspects modify this pattern. First, the obscuring secondary mirror that is placed in front of the primary and the mounting structure, colloquially referred to as telescope spiders, which are present in most modern telescopes, change the cross-section of the aperture, leading to a modified Airy pattern. Fig. 2.2 shows the respective diffraction pattern for a variety of increasing central obscuration by a secondary mirror where the general central shape is conserved but increasingly more light is diffracted into the outer lobes. Second, atmospheric turbulence disturbs any coherent wavefront, which can result in a significantly degraded image (see Sec. 3.2). The specific pattern generated by a coherent point source in the image is called point spread function (PSF) and is characterizing the optical properties of the system, environment, and observing conditions.

Diffraction limit

This diffraction imposes a fundamental limit on the angular resolution capability of any telescope and, in fact, of any optical system. The most prominent effect is the inability to distinguish multiple sources that have an angular separation smaller than the Airy disk width. In astronomy, the *Rayleigh criterion* has been established as an appropriate quantification. It states that two point sources can be distinguished as long as the first diffraction minimum of the first source coincides or is further away from the main diffraction center of a second equally bright source. This results in a resolving limiting

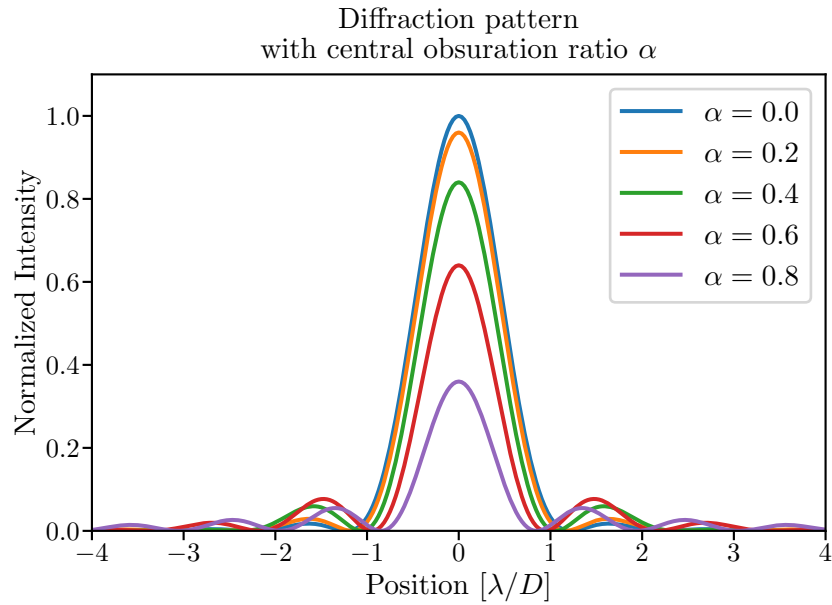


Figure 2.2: Cross section of the diffraction pattern with different sizes of the secondary mirror, labeled by obscuration ratio $\alpha = D_{\text{obs.}}/D$ between the diameter of the obscuring (secondary) mirror $D_{\text{obs.}}$ and the primary mirror D .

angle Θ_0 for a diffraction-limited observation of

$$\Theta_0 \sim 1.22 \lambda/D \quad . \quad (2.3)$$

Note that the angular precision is not necessarily restricted by the diffraction limit, because the position of an Airy disk can be reconstructed much more accurately. For example, the extraordinary angular precision of the space-based *Gaia* telescope reaches up to $7 \mu\text{as}$ while the Rayleigh criterion of its 0.5×1.45 m rectangular primary mirrors corresponds to a diffraction limit of 52 mas.

2.1.5 Wavefront error

As noted, diffraction to an Airy pattern assumes a coherent incoming wavefront, loosely referred to as a flat wavefront as it has a constant phase across the aperture. In practice, there are many optical effects that will degrade the coherence of the wavefront. The two main influences that should be mentioned are optical aberrations from within the telescope and atmospheric Seeing. The seeing disturbance is caused by atmospheric turbulence and is covered in more detail in Sec. 3.2.

Aberrations induced by optics

Optical aberrations that can occur from within the telescope system can be classified into two groups. Firstly, they may occur during the manufacturing of the optical surfaces and the corresponding surface irregularities. Secondly, optical misalignment can degrade optical performance because the optical elements are not properly positioned in both location and angle. Both effects have a static component, but they usually also have a dynamic component, resulting from a changing telescope orientation and the corresponding gravitational forces or from temperature variations and gradients that will substantially impact the optical components.

These negative effects can be reduced in design and manufacturing but are often also addressed by active optics that will detect and compensate for misalignment on <1 Hz timescales. These can be implemented both in the primary mirror, as this is the largest mirror in any telescope and hence impacted the most by gravitational deformation, but will often also include tip-tilt mirrors to adjust alignment further down the optical train. In this context, optical misalignment from vibrations throughout the telescope plays a special role, as it occurs on much higher frequencies and requires a different correction strategy (see Sec. 3.2.2).

Zernike modes

Optical aberrations are most commonly quantified with the Zernike mode basis. This is an orthogonal basis of two-dimensional functions that describes the phase of a circular wavefront. Both circular coverage and meaningful parametrization make this the most widely established mode basis in astronomical contexts. Other commonly used mode bases are the Gram-Schmidt orthogonalization for annular optical cross sections common in Cassegrain telescope designs or the Legendre polynomial for rectangular beam footprints, as they frequently occur in laser systems.

The Zernike polynomial, parameterized by Noll (1976) with polar parametrization r and θ over a pupil with unit radius, is expressed as (Roddier, 1999)

$$Z_n^m = \sqrt{n+1} (A_{nm} \cos(m\theta) + B_{nm} \sin(m\theta)) \cdot R_n^m(r) \quad , \quad (2.4)$$

where

$$R_n^m(r) = \sum_{s=0}^{\frac{n-m}{2}} \frac{(-1)^s (n-s)!}{s! \left(\frac{n+m}{2} - s\right)! \left(\frac{n-m}{2} - s\right)!} (r)^{n-2s} \quad . \quad (2.5)$$

Here, the index notation describes the radial degree n and the azimuthal frequency m , as well as its orientation A and B . The first Zernike polynomials are listed in Tab. 2.1 with their respective normalized radial and angular dependence. The table also lists the names of the corresponding aberration nomenclature that are linked to common optical occurrences with misalignment of optical elements or manufacturing errors. Fig. 2.3 shows some of the corresponding phase distortions with their respective

2 Theoretical background of physics

Z	n	m	A/B	mode name	rad. term	azim. term
Z_1	0	0		Piston	1	
Z_2	1	1	A	Tip	$2r$	$\cos(\theta)$
Z_3	1	1	B	Tilt	$2r$	$\sin(\theta)$
Z_4	2	0		Focus	$\sqrt{3}(2r^2 - 1)$	
Z_5	2	2	A	Astigmatism 1	$\sqrt{6}r^2$	$\cos(2\theta)$
Z_6	2	2	B	Astigmatism 2	$\sqrt{6}r^2$	$\sin(2\theta)$
Z_7	3	1	A	Coma 1	$\sqrt{8}(3r^3 - 2)$	$\cos(\theta)$
Z_8	3	1	B	Coma 2	$\sqrt{8}(3r^3 - 2)$	$\sin(\theta)$
Z_9	3	3	A	Trefoil 1	$\sqrt{8}r^3$	$\cos(3\theta)$
Z_{10}	3	3	B	Trefoil 2	$\sqrt{8}r^3$	$\sin(3\theta)$

Table 2.1: First Zernike modes and their radial and azimuthal terms.

diffraction pattern.

2.2 Optical waveguides

Optical waveguides, such as optical fibers, are employed at many modern observatories. In its simplest configuration, optical waveguides consist of a core and surrounding cladding. Both these components are translucent but feature slightly different refractive indexes. Light can then be confined within the core through internal reflection.

2.2.1 Light propagation in MMFs

Fig. 2.4 shows a schematic representation of an optical multi-mode fiber (MMF). Photons within the waveguide are internally reflected at the boundary layer between the fiber core and its surrounding cladding due to the core's higher reflective index n_1 compared to the reflective index of the cladding n_2 . This means that light is confined to the fiber's core with a reasonable amount of loss as a result of absorption from the fiber material. In practice, additional losses occur when the fiber is bent and the corresponding geometric deformation occurs.

The minimum angle of reflectance or total internal reflection within the fiber governs the numerical aperture (NA) of the fiber. The NA is defined as the tangent of the angular extend θ of the cone of light in conjunction with the refractive index n of the surrounding medium that propagates in any optical system and is expressed as

$$NA = n \cdot \tan(\theta), \quad (2.6)$$

which relates to the F-Number with

$$F/\# = \frac{1}{2 \cdot NA}. \quad (2.7)$$

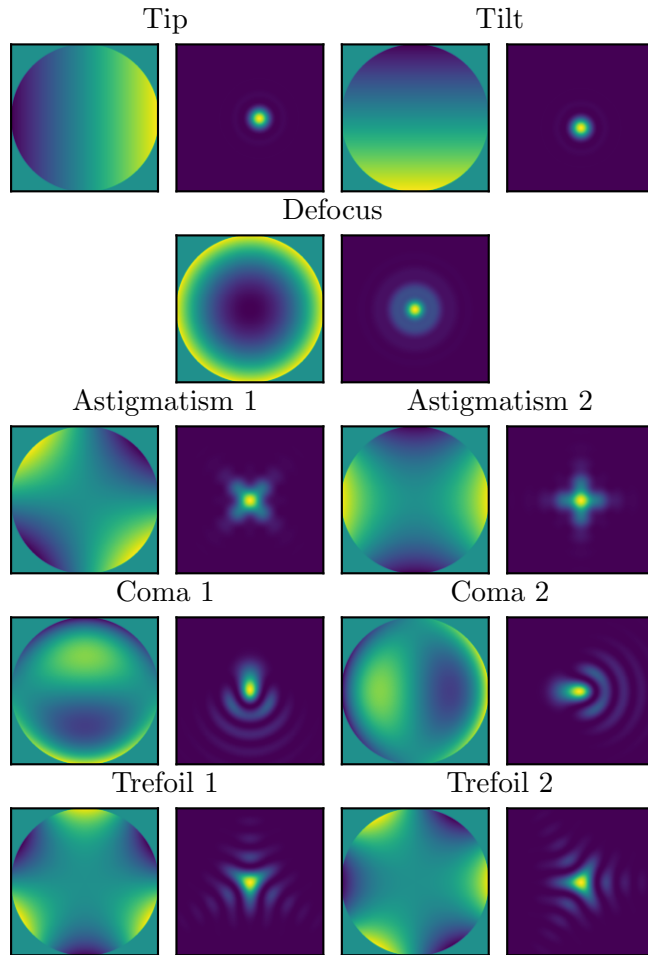


Figure 2.3: Zernike polynomials in Noll indexing order. **Left panels:** Phase of the wavefront in the pupil plane; **right panels:** Respective diffraction pattern as seen in the intensity of the light in the focal plane. Both phase and intensity are normalized to the corresponding maximum value, $Z = 1$ for each aberration.

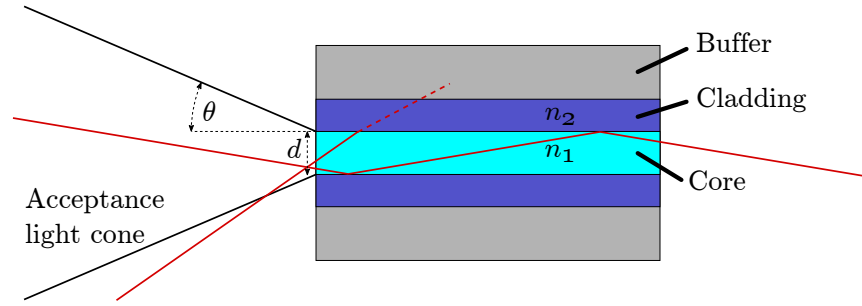


Figure 2.4: Light rays coupling to a fiber according to the geometrical ray model. Light rays (red) are internally reflected at the boundary between the core (cyan) and cladding (blue) as the larger refractive index of the core n_1 is larger than the cladding's refractive index n_2 . If the incident angle of a light ray is larger than the acceptance angle θ , the light is not confined to the core but refracted into the cladding (dashed red line). The image represents a typical multi-mode fiber (MMF) with a core diameter of $d = 50 \mu\text{m}$, a cladding diameter of $125 \mu\text{m}$ and a protective buffer with a diameter of $250 \mu\text{m}$.

For internal reflection within the optical waveguide, this refers to the light cone that efficiently couples into the fiber and then exits the fiber. The slight mismatch between the light entering and exiting is commonly called focal ratio degradation (FRD).

Based on the Fresnel law, the NA of a MMF with a step function refractive index profile can be expressed as

$$\text{NA}_{\text{MMF}} = \sqrt{n_1^2 - n_2^2} \quad . \quad (2.8)$$

Propagation modes

The description above is only a geometric approximation of the physics involved. A more accurate treatment is obtained by solving the wave equation (Sec. 2.1.2) in this specific environment.

The calculations involved are outside the scope of this work, but it should be mentioned that the specific solutions obtained from this exercise result in a number of different modes in which the EM field can propagate. The number of modes that a waveguide can host depends on the geometric layout and the wavelength λ .

When working with a circular fiber with a step-index refractive index profile with a core diameter d , the dimensionless characteristic **V-number** of the waveguide (Mitschke, 2016)

$$V = \frac{\pi d \text{NA}}{\lambda} \quad (2.9)$$

is a measure for the one-dimensional optical phase space. This can be used to approximate the number of different modes that the fiber can transport. For MMFs with a

large number of modes $N \gg 1$ and, accordingly, $V \gg 1$ this approximation yields the number of modes

$$N \sim \frac{V^2}{4} . \quad (2.10)$$

2.2.2 Light propagation in SMFs

As suggested by eq. 2.9 and eq. 2.10, the number of supported modes decreases linearly with decreasing core cross-sectional area. At a threshold of

$$V < 2.405, \quad (2.11)$$

only one mode per polarization state is coupled into the waveguide. The waveguide is then in the single-mode (SM) regime, and the propagated mode is referred to as the *fundamental mode*.

In the common case of a step-index fiber, the fundamental mode involves the Bessel function (Mitschke, 2016). However, the intensity I in dependence on the radial coordinate r perpendicular to the propagation direction can be closely modeled by a Gaussian profile

$$\Rightarrow I \underset{\sim}{\propto} \exp\left(\frac{-r^2}{2 \cdot \sigma}\right) . \quad (2.12)$$

Gaussian beam

This Gaussian intensity profile resembles a *Gaussian beam*. The Gaussian beam is a solution to the wave equation for free-space optical propagation. It features the unique optical characteristic that it does not change its profile shape when it propagates from near-field to far-field, e.g. when it is focused or when it is collimated.

This is a direct consequence of the Fourier optics, as outlined in Sec. 2.1.3 because the Fourier transform of a Gaussian is again of the same shape. This makes it very convenient to use in optical systems.

A Gaussian beam is sufficiently characterized by its beam waist radius w_0 corresponding to the radius at the waist of the beam where the intensity has decreased to $1/e^2$. In the context of SMFs this is often also described by the $1/e^2$ -intensity mode-field diameter (MFD) with $\text{MFD} = 2w_0$.

The intensity I of the Gaussian beam along its propagation axis z and its distance from the optical axis r is (Hecht, 2002)

$$I(r, z) = I_0 \left(\frac{w_0}{w(z)}\right)^2 \exp\left(\frac{-2r^2}{w(z)^2}\right) , \quad (2.13)$$

where I_0 is the maximum beam intensity and is related to the total power of the beam

2 Theoretical background of physics

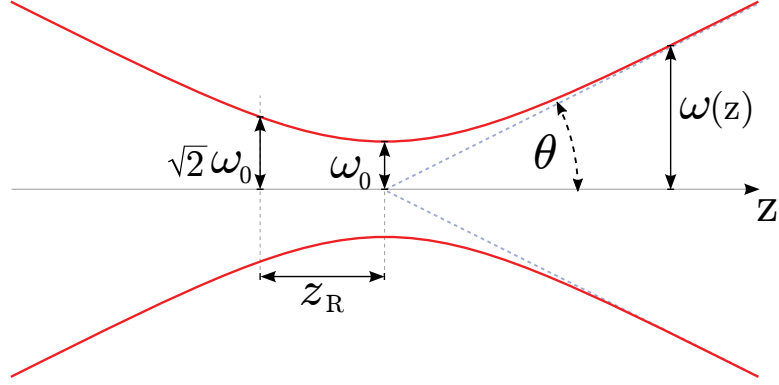


Figure 2.5: Gaussian beam waist shape and the respective parameters.

Source: GaussianBeamWaist (<https://commons.wikimedia.org/wiki/File:GaussianBeamWaist.svg>) by Rodolfo Hermans, DrBob used under CC BY-SA 3.0 (<https://creativecommons.org/licenses/by-sa/3.0/deed.en>) / modified parameters.

P_0 with

$$I_0 = \frac{2P_0}{\pi w_0^2} . \quad (2.14)$$

The evolution of the width of the beam $w(z)$ is

$$w(z) = w_0 \sqrt{1 + \left(\frac{z}{z_R}\right)^2} , \quad (2.15)$$

where z_R is the Rayleigh range

$$z_R = \frac{\pi w_0^2 n}{\lambda} , \quad (2.16)$$

with the index of refraction n of the propagation medium.

The beam divergence and with that the NA of a Gaussian beam rely solely on these equations. Because the beam profile does not feature any sharp edges, it is not well defined, but parallel to the definition of the waist, it is also conventionally termed the divergence angle at which the intensity has decreased to $1/e^2$ of the central value. For a linearly diverging beam, as is approximately the case far from the waist $z \gg z_R$, the NA of the Gaussian beam can be expressed as

$$\text{NA} \sim \frac{\lambda}{\pi n w_0} . \quad (2.17)$$

Therefore, the NA of a SMF fundamentally differs from that of a MMF as it is the Gaussian beam that approximates the fundamental mode that describes the behavior of

the propagating light.

Coupling efficiency

The fraction of the EM field that is bound to the fiber's core corresponds to the radiation that matches the fundamental mode of the fiber itself. Mathematically, this can be calculated with the overlap integral between the incoming field $\psi_{\text{Tele.}}$ and the accepted field ψ_{SMF} to produce the coupled amplitude (Ruilier, 1998).

The overlap integral of the surface s between two fields X and Y is expressed as

$$\langle X|Y \rangle = \int \int_{\mathbb{R}^2} X(\vec{s}) \cdot Y^*(\vec{s}) d^2s \quad (2.18)$$

and the total summed amplitude of a field X is expressed as

$$\|X\| = \sqrt{\langle X|X \rangle} \quad . \quad (2.19)$$

With that, one can calculate the fractional coupled amplitude

$$A = \frac{\langle \psi_{\text{Tele.}} | \psi_{\text{SMF}} \rangle}{\|\psi_{\text{Tele.}}\| \cdot \|\psi_{\text{SMF}}\|} \quad , \quad (2.20)$$

eventually yielding the fraction of the total power that is injected into the fiber, commonly referred to as *fiber coupling efficiency*

$$\rho = \|A\|^2 \quad . \quad (2.21)$$

Due to Parseval's theorem, this calculation can also be performed in the pupil plane (Ruilier and Cassaing, 2001).

SMF coupling at telescope

The intensity profile encountered in a telescope does not match that of the Gaussian beam, but rather features the circular step function profile with additional modifications (see Sec. 2.1.4). However, the central main maximum of the resulting Airy disk can be approximated by a Gaussian waist, see Fig. 2.6.

Ruilier (1998) analytically calculated the resulting coupling efficiency of a circular aperture with a central obstruction (ratio α) to

$$\rho(\beta) = 2 \left(\frac{e^{-\beta^2} (1 - e^{\beta^2(1-\alpha^2)})}{\beta \sqrt{(1-\alpha^2)}} \right)^2 \quad (2.22)$$

with

$$\beta = \frac{\pi}{2F/\#} \frac{w_0}{\lambda} \quad . \quad (2.23)$$

2 Theoretical background of physics

For an unobstructed pupil ($\alpha = 0$), a Gaussian beam waist w_0 of

$$w_0/F/\# = 0.71 \lambda/D \quad (2.24)$$

yields the maximum achievable efficiency of 81%. Taking into account the Fresnel reflections on the fiber face, this is reduced to 78% (Shaklan and Roddier, 1988; Ruilier, 1998). Fig. 2.6 shows the Airy disk and the best-fit Gaussian profiles.

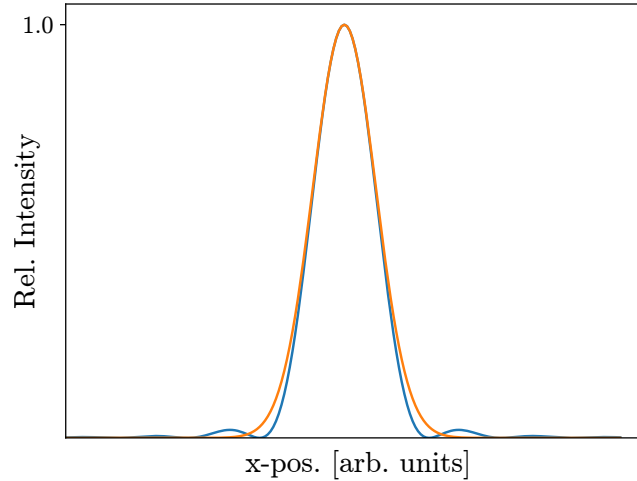


Figure 2.6: Cross section of the Airy disk (blue) and the best Gaussian fit (orange)

Modified coupling at telescopes

This achievable efficiency is further reduced if a disturbed wavefront is coupled to the SMF. Fig. 2.7 shows the impact of different Zernike modes on coupling efficiency. For a more detailed analysis that also covers the impact of atmospheric turbulence and the correction of AO, the interested reader is referred to Ruilier and Cassaing (2001).

On the other hand, the use of phase-induced amplitude apodization (PIAA) (Guyon, 2003) to modify the shape of the intensity profile in the pupil can be used to better match the fundamental mode of the SMF. With this, the coupling efficiency can be significantly improved (Guyon, 2003; Jovanovic et al., 2017b).

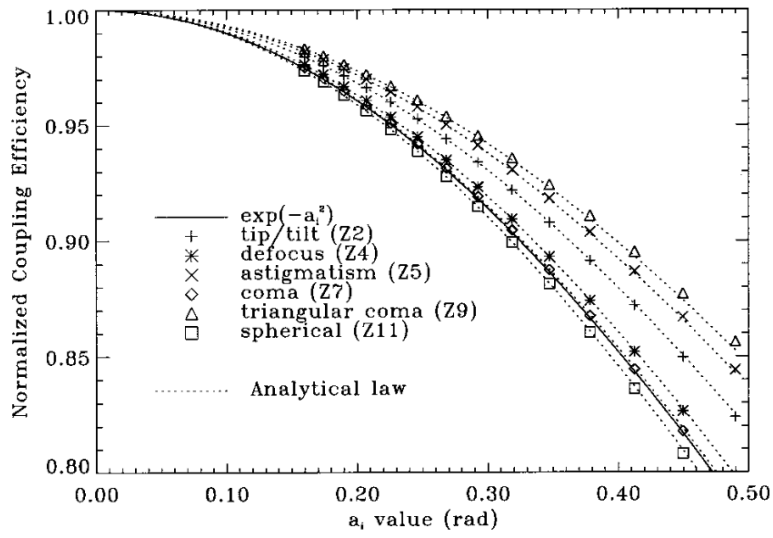


Figure 2.7: SMF coupling as a function of RMS wavefront distortion denoted by the coefficient a_i of a single Zernike mode. Shown for simulations of different modes (markers) and the corresponding analytical solution (dotted line). (Reprinted from *Ruilier and Cassaing, 2001*)

3 Astronomical instrumentation

The previous chapter covered the physical principles that are needed to describe the concepts presented in this work. This chapter now focuses on the specific applications as they are encountered in astronomy while relating to those concepts. Namely, this chapter covers general optical telescope design, fundamentals of AO systems, and the role of integrated optics, including optical fibers, in telescopes.

3.1 Telescope optics - basic concept and context

Optical observations are the most natural form of astronomical data collection, and historically gazing at the stars has played an important role in many cultures not only for the astronomical understanding of the observed sky but also for spatial and temporal navigation, with plenty of room for religious and cultural interpretation.

Optical telescopes have been the most essential cornerstone of astronomical observations for centuries. They can detect most astronomical phenomena and do so both at high angular resolution and with very high sensitivity. As they can cover a large wavelength range from ultraviolet (UV) through to mid infrared (mid-IR), they allow the extraction of meaningful spectroscopic information corresponding to various astrophysical phenomena.

The basic forms of refractive and reflective manipulation of light have been practically understood since the invention of glass, which also led to the development and deployment of the first telescopes. Today, a wider range of observational strategies are pursued to use all information that is transmitted from astronomical sources from the high-energy gamma radiation to the long-wavelength radio frequencies of the electromagnetic spectrum. More recently, these observations have been supplemented with data from unconventional measurements, such as neutrino detection and, most recently, observations of gravitational waves.

The development and use of optical telescopes is still the most important method of data acquisition in astronomical research. The spectral and angular resolution achieved at state-of-the-art observatories is at a very high qualitative level. However, there is still plenty of improvement to be made in terms of sensitivity and information drawn from the incoming photons. This is done by increasing the size of the telescope and instrument, while correspondingly improving the quality of the employed optics. It is also done by optimizing light manipulation and developing ever-new technological approaches.

In its basic principle, optical telescopes focus incoming light onto photon-detecting surfaces. This basic function is shared by most imaging systems, such as microscopes and consumer cameras. The very specific requirements to observe most astronomical

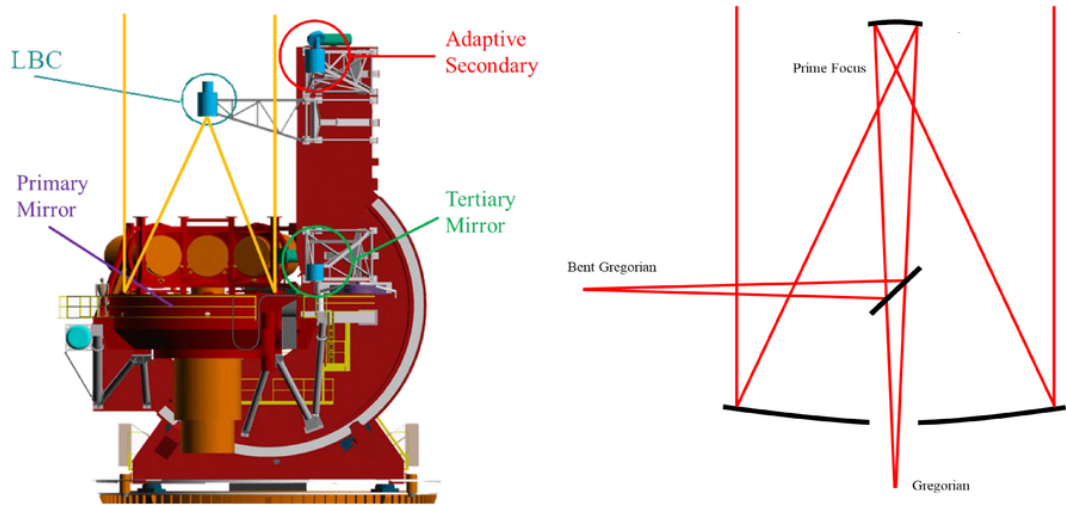


Figure 3.1: Schematic representation of the LBT in its prime focus usage (left) and in its Gregorian configuration (right). The light enters the telescope from the top and is then reflected by the large primary mirror either directly onto a camera or with an additional secondary mirror extending its focal length. *(Reprinted from Rodriguez et al., 2020)*

targets lead to a very specialized telescope design that has evolved with theoretical and technological advancements over history.

Fig. 3.1 shows a schematic representation of a Gregorian telescope, namely the LBT with its optical path. For a simple overview, the LBT is a great representation of a very flexible telescope, but one should bear in mind that there are a number of different telescope designs that are used in large observatories throughout the world. In its prime-focus operation mode (Fig. 3.1, left panel), the LBT can be used in a single-mirror configuration and a camera (in this case, Large Binocular Cameras, LBC) is mounted by a swing arm and sits above the primary mirror. More universal optics can be employed if the light beam is instead reflected by a secondary mirror (Fig. 3.1, right panel) that extends the focal length and additionally corrects the focus to form a plane surface opposed to the curved prime focal surface. A retractable tertiary fold mirror can redirect the light pass to be accessed at the bent Gregorian focus, where additional instruments can be mounted with less gravitational lever.

At the focal point, a simple telescope setup can already deploy a prime-focus instrument such as an imaging detector array. More advanced systems will reimagine the light to achieve the desired optical magnification, spectral filtering, or spectrally resolving the light. The two main optical parameters that describe the geometry of the incoming light of a telescope at the focal point are its field-of-view (FoV) and its plate scale p . The FoV is the angular extent over which the system is capable of transmitting light rays and over which it is capable of producing sufficient optical performance. The deployed

3.2 Adaptive optics - atmospheric disturbance and its correction

photon detector will only be feasible to extend across this field. If downstream optics are employed, an optical field stop will be placed to block unwanted stray light that might negatively impact the performance even within the FoV.

The plate scale p governs the scaling between the angular distances of the astronomical sources $\Delta\theta$ and their corresponding linear separation Δs at the focal plane. It corresponds to the inverse of the focal length f as

$$p = \frac{\Delta\theta}{\Delta s} = \frac{1}{f} \quad . \quad (3.1)$$

3.2 Adaptive optics - atmospheric disturbance and its correction

In many modern telescopes, adaptive optics (AO) systems are a crucial part, as they drastically improve the telescope's angular resolution capabilities. This is particularly important for large telescopes including the new era of 30-40 m extremely large telescopes (ELTs) that are highly Seeing-limited due to atmospheric perturbation. AO can improve the efficiency of observatories in the sense that a sharper PSF will achieve a given SNR more quickly, but even more so, it can enable more qualitative observations. This technique is therefore fundamental for many state-of-the-art science cases, particularly including, but not limited to, exoplanet detection and direct observation with its stringent requirements on angular resolution, contrast, and spectral resolution. The field of AO is broad with a wide range of different concepts and components. This section will focus on the exoplanet science case with the corresponding AO approach of particularly good correction over a small FoV, commonly referred to as extreme adaptive optics (ExAO, sometimes XAO or eXAO). ExAO employs the fundamental AO concepts without referring to more complicated approaches but does so in a very stringent way to optimize image quality.

3.2.1 Atmospheric Seeing

For most telescopes, atmospheric perturbations have a particular impact on the incoming wavefront and dominate the degradation of the optical performance. This phenomenon is referred to as *Seeing* and describes the aberration of light through variations in the refractive index of the atmosphere's air and the resulting perturbations in the wavefront. As different parts of the atmosphere can vary widely in temperature, density, pressure, and chemical composition, the refractive indices associated with the corresponding atmospheric layer can vary widely as well. These spatial inhomogeneities are associated with turbulent cells of different sizes and will also vary temporally. Naturally, the exact behavior of the atmosphere is complex and very chaotic, and hence difficult to simulate and nearly impossible to predict accurately.

Parametrization

The two main parameters that are used to quantitatively describe the encountered Seeing are the coherent length and time scales r_0 and τ_0 , respectively. This parametrization is used to describe the general Seeing conditions both at a particular telescope site and to describe the conditions for a certain observation.

The length scale r_0 , also called Fried parameter, describes the spatial extent over which the wavefront can be considered coherent. This is quantified as an RMS wavefront error of $\lesssim 1$ rad, as this results in image aberrations similar to the impact by diffraction. The length scale refers to the physical size of the turbulent cells as imaged onto the telescope's pupil. The corresponding angular extent of the observed aberrations and the effective angular resolution is called the Seeing parameter θ_0 .

The coherence time τ_0 corresponds to the time it takes for the turbulent atmospheric layer to move the distance of the Fried parameter r_0 . If the associated layer moves with a wind velocity v_0 , the coherence time can be described as

$$\tau_0 = \frac{r_0}{v_0} \quad . \quad (3.2)$$

The coherence time governs the timescale over which a Seeing-corrected wavefront remains corrected, and thus defines the required frequency at which an AO system needs to correct for it.

These two characteristic parameters vary strongly between different observing sites but can also change significantly between seasons, nights, and even during the observation night itself. For the selection of good observatory site locations, the altitude of the site and the amount of turbulent airflow above are the most important selection criteria. For more elevated observatories, the light reaching the telescope passes through shorter air columns and omits the lower atmospheric layers, which feature a higher density and hence contribute the largest fraction of the atmospheric aberrations. These factors alone already point to the most used observatory locations around the world, such as the Atacama desert in Chile with its peaks at altitudes around 4000 m and its laminar air flow currents. Other locations with similar properties are La Palma and the Mauna Kea mountain in Hawaii, which also host a large number of state-of-the-art optical observatories.

Kolmogorov turbulence

Turbulence in the atmosphere is known to behave closely to Kolmogorov cascading (Kolmogorov, 1941; Tatarski et al., 1961). This predicts the transfer of energy from large-scale perturbations into smaller turbulent cells (eddies) before eventually discharging into internal energy, i.e. heat. The resulting RMS wavefront error σ is then predicted to be related to the primary mirror diameter D with

$$\sigma^2 = 1.03 \left(\frac{D}{r_0} \right)^{\frac{5}{3}} \quad . \quad (3.3)$$

3.2 Adaptive optics - atmospheric disturbance and its correction

The same absolute path-length difference will affect coherence more for smaller wavelengths. This results in a reduced Fried parameter and coherence time, scaling with

$$r_0 \propto \tau \propto \lambda^{\frac{6}{5}} . \quad (3.4)$$

For instrument development, this means that AO correction at a longer wavelength, i.e. in the infrared (IR) range, is easier achievable, while wavefront control in the regime of visible light becomes more challenging, albeit eventually also enabling a smaller diffraction limit.

Strehl ratio

Although the RMS error describes the quality of the wavefront rather well, it is an optical measurement that is not directly correlated to the resulting observed image. For this, the Strehl ratio (SR) has been established as a measurement of the resulting image quality. The SR is defined as

$$\text{SR} = \frac{\max(I_{\text{PSF}})}{\max(I_{\text{Airy}})} , \quad (3.5)$$

measuring the ratio between the peak intensity of the observed PSF and the theoretically best possible diffraction pattern, the modified Airy disk of the optical system. It should be noted that this quantification does not incorporate some aspects that might be important for observations such as speckle presence or fiber coupling availability and other metrics used for specific applications.

3.2.2 Telescope vibrations

A somewhat separate role plays the impact that vibrations can have on the optics. In contrast to the atmospheric turbulence that causes Seeing, vibrations are caused from within the telescope structure itself. Vibrations can be caused by different origins. The most prominent are the cooling components of the instruments, in particular the powerful cryogenic coolers, telescope movement during slewing and guiding, as well as wind-induced loads on the structure. These movements are especially severe if they coincide with or are indirect aliases to resonance frequencies of the telescope structure. As these resonance frequencies are excited, the corresponding vibrations can have high amplitude. These high power disturbances at otherwise unusual frequencies make handling vibrational disturbances particularly difficult. Fig. 3.2 show the power spectrum at the LBT as observed by the iLocator spectrograph acquisition camera showing the characteristics of the vibrations with its distinctive peaks.

3.2.3 Wavefront sensing

To perform the wavefront correction, the error of it needs to be measured. This is done with a wavefront sensor (WFS). Most WFSs do not measure the phase of the wavefront

3 Astronomical instrumentation

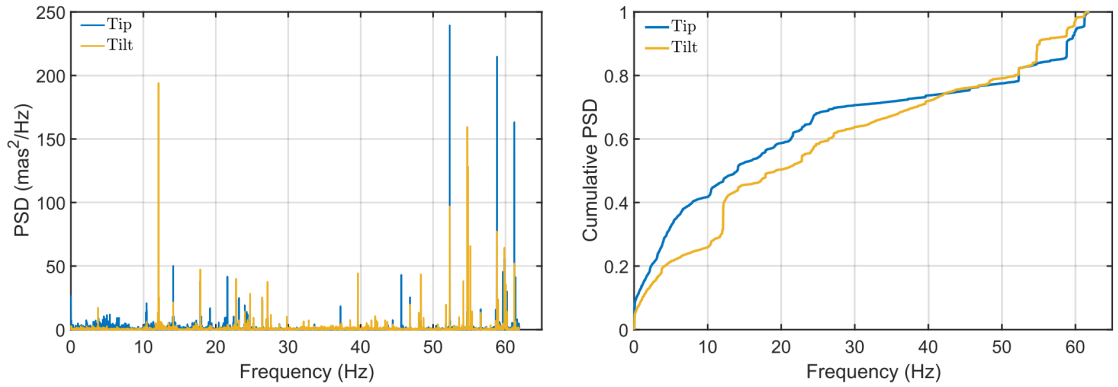


Figure 3.2: **Left:** PSD of LBT as measured by iLocator, with AO correction considering 300 modes; **right:** normalized cumulative representation.
(Reprinted from *Bechter et al., 2019*)

itself, but rather the gradient, which is then integrated to produce the actual phase across the pupil.

The most common WFSs currently in use are Shack-Hartmann WFS (SH-WFS) and Pyramid WFS (PyWFS). But there are other forms of tip and tilt measurements that are additionally employed. This includes the usage of a pinhole mirror, which helps to image the light that is not aligned to the optical axis to reconstruct the centroid of the beam. Another method is the usage of a quadrant detector, commonly called *quad-cell*, which reconstructs the centroid by the differential flux between pixels (Tyler and Fried, 1982). In addition to the above-mentioned optical sensors, there is also the option to use sensitive accelerometers for measuring the mechanical vibrations (Glück et al., 2017).

Most AO applications operate in the photon-starved regime, resulting in reduced performance for faint targets or targets where no natural guide star (NGS) acting as a reference target for the AO system, is located in close proximity (Rigaut, 2015). Therefore, a number of observatories also employ laser guide stars (LGSs) to artificially create such a source for reference measurements.

3.2.4 Wavefront control

In order to correct the disturbances, the wavefront needs to be manipulated with a wavefront correction (WFC) device. Most commonly, this is done with a deformable mirror (DM) that can change its shape dynamically. This is performed with actuators either on a thin mirror that can deform slightly or with a segmented mirror with each segment individually controllable.

Both the frequency of correction and the number of required actuators change with the size of the telescope’s primary mirror. For larger telescope diameters, the low-order spatial modes have an increasingly larger amplitude, but also change at smaller temporal frequencies. At the same time, a larger diameter means that more actuators are necessary to fully correct the wavefront. Therefore, it is common to delegate the

correction between two different DMs, one fast-running, high actuator count mirror, and one low actuator count, slow but large dynamical range mirror. Furthermore, in some applications, tip-tilt mirrors are incorporated that only correct for tip and tilt, but often at higher temporal frequencies where some of the vibrational disturbances may occur.

3.2.5 Controlling

The measured WFS data need to be processed and transformed into a correction signal to send to the WFC. The *controller* handles computerized data processing, including sensor readout, measurement calibration, normalization, and wavefront reconstruction from the WFS measurements.

The core control algorithm then uses the calculated wavefront to evaluate the best shape to be applied to the DM. There is a wide range of different algorithms, but in astronomy, the integrator is used most commonly. The integrator uses the error of the wavefront phase such as,

$$e(\vec{r}, t) = \Phi_{\text{Target}}(\vec{r}, t) - \Phi_{\text{WFS}}(\vec{r}, t) \quad , \quad (3.6)$$

where $e(\vec{r}, t)$ is the offset between the desired wavefront Φ_{Target} and the measured and reconstructed wavefront Φ_{WFS} . This error is converted to the appropriate mirror shape by multiplication with the reconstruction matrix K . The reconstruction matrix provides a method to convert the desired wavefront shape into an applicable mirror shape. The reconstruction matrix is calculated by inverting the interaction matrix IMX that is measured by applying known mirror commands while observing the resulting wavefront. Then, a gain γ is applied to this error to produce the mirror shape Φ_{DM} to be sent to the DM

$$\Phi_{\text{DM}}(\vec{r}, t) = \alpha\Phi_{\text{DM}}(\vec{r}, t - T) + \gamma K [e(\vec{r}, t - \delta T) + w] \quad . \quad (3.7)$$

This is performed in a closed-loop operation. The mirror command from the previous iteration $\Phi_{\text{DM}}(\vec{r}, t - T)$ is maintained but is damped by an integration factor $\alpha \lesssim 1$. This equation also considers the additional noise w that is included in the WFS measurement, as well as the latency δT between the sensor measurement and the final application to the wavefront corrector.

3.3 Integrated optics - fibers & astrophotonics

In Sec. 2.2, the physical principles of waveguides were outlined. In the following section, the application of waveguides to telescopes is shown. Then, some of the concepts for integrated optics and photonics at observatories are introduced, with a focus on integration with AO.

3.3.1 Optical fibers at telescopes

The main benefit of optical fibers is their flexibility in combination with their low complexity. The input to the fiber at the telescope's light path can be positioned precisely on the focal plane with almost arbitrary positioning. The fiber output can be placed very reliably on the instrument input while retaining its high temporal and spatial stability.

Also, the fiber itself can be routed very freely, reducing the complexity of the optical system. This allows the instrument to be placed independently of the telescope structure in a stabilized environment. This includes temperature stabilization that can be achieved much easier, as well as gravitational stability as the instrument does not need to move with the telescope structure. Another important objective is the decoupling from the vibrational characteristics of the other components.

Optical waveguides enable dynamic placement of the fiber and possible combinations of multiple fibers. These allow for very flexible designs of multi object (MO) spectrographs with multiple fibers positioned at will for each integration. They also allow integral-field unit (IFU) spectrographs with fibers tightly packed within one fiber bundle for spatially resolved spectral analysis.

3.3.2 SMFs at telescopes

Fig. 3.3 shows a schematic representation of both the telescope optics that couple an astronomical source into a slit or a fiber and the spectrograph that disperses the light onto a detector. The main optical characteristics of fibers are the diameter of the fiber core and its NA. The beam of the telescope can be reimaged to match the NA of the fiber, the core diameter then governs the area of the focal plane and with that the fraction of the PSF that is coupled into the fiber.

A larger fiber core can collect more light, either from multiple or extended sources or from an uncorrected PSF. This is done in many applications but has two main drawbacks; first, more sky background is coupled into the fiber, causing more background noise in the observations, and second, the working principle of many instruments is highly dependent on both the core diameter of the fiber and its NA. The resolving power of a spectrograph, for example, scales inversely proportional to its input slit width and with that to the diameter of the fiber core feeding the spectrograph.

The spectral resolving power R of a spectrograph is given by (Allington-Smith, 2006)

$$R = \frac{\lambda}{\Delta\lambda} = \frac{m\rho\lambda W}{\chi D} \quad (3.8)$$

$$= \frac{m\rho\lambda W}{2NA d} \quad , \quad (3.9)$$

with the density of the grating ρ , the diffraction order m , the size of the illuminated grating W , the angular slit diameter χ corresponding to a spatial slit or fiber diameter d , and the telescope pupil diameter D , or the NA of the fiber or incoming beam, respectively. To maintain a high spectral resolution, a larger fiber diameter needs to be counteracted by a linearly increasing grating size. In most spectrographs, the grating is already

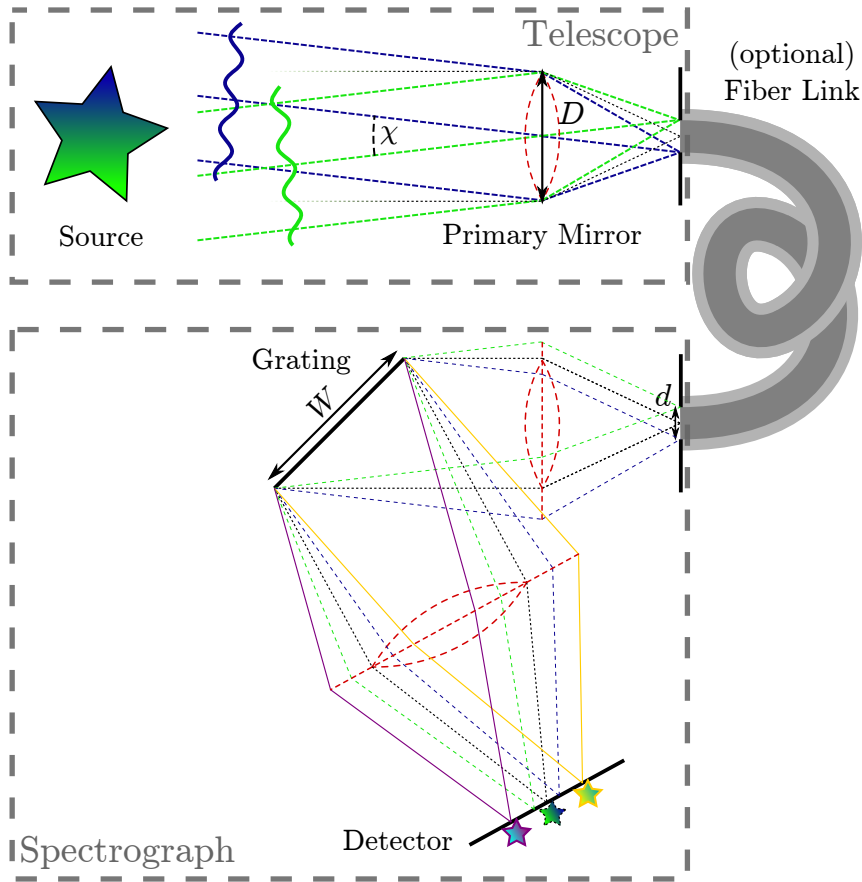


Figure 3.3: *Schematic representation* of telescope and spectrograph. An angular extended source (physically extended or by atmospheric Seeing, green/blue dashed lines) is coupled into a slit or fiber and from there projected onto a grating. The spectrally dispersed slit image (purple/yellow solid lines) or fiber output is then imaged on the detector.

the largest optical component. Increasing its size will therefore increase the overall instrument and, with it, the size of the volume that needs to be stabilized.

For these reasons, it is very beneficial to reduce the size of the fiber. The modes within the fiber in which light propagates have an impact on the shape of the LSF that is convoluted with the spectrum of the source. This effect can be especially strong for small, few-mode fibers where individual modes make up a disproportionately large part of the combined fiber output. This change is temporal and chromatic and can thus significantly change the reconstructed centroid of a spectral line. The noise associated with the measurement is called *modal noise*. Due to its stringent requirements, high-precision radial velocity measurements are especially affected by this (Goodman and Rawson, 1981; Harris et al., 2016).

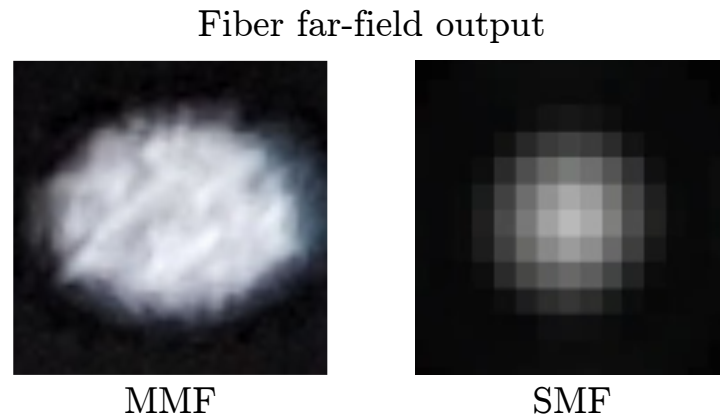


Figure 3.4: Fiber far-field output as measured in the laboratory. **Left panel:** MMF output (slightly out of focus); **right panel:** SMF output (magnified).

In the extreme case of SMFs, this problem is avoided. As there is only one, the fundamental, mode, the output shape of the fiber is temporally stable. Fig. 3.4 shows the output of a MMF and a SMF, with the former showing a complex pattern of differently illuminated modes and the latter a fundamental mode with near-Gaussian intensity profile. Only the coupled intensity of the fiber changes, which is not associated with a shift in the centroid of the spectroscopic lines. It should be noted that there is weaker noise associated with the two polarization modes within the fiber (Halverson et al., 2015).

As seen in eq. 3.9, the resolving power does not scale with the telescope size when using a SMF. For a larger telescope, the size of the spectrograph does not scale with it. These properties make the use of SMFs extremely desirable. However, the corresponding challenge is the massively increased difficulty of coupling light into the fiber. As shown in Sec. 2.2.2, the wavefront from the telescope needs to match the near-Gaussian fundamental mode of the SMF. To achieve this, the wavefront needs to be corrected sufficiently.

3.3.3 Integrated optics in AO

Most of the optical components used in telescopes can be referred to as *bulk optics*. These are conventional mirrors and lenses with the addition of many specific elements, such as gratings and wavelength filters.

One particular exception is optical fibers that manipulate light in a more direct way. Optical fibers can be grouped into the general area of photonics, a class of optical components that confine photons in small spatial scales and are able to include light manipulation and processing. These components can be designed to provide some of the functionality that conventional bulk optics would perform otherwise. This is then an integrated photonic device, potentially reducing the size of the optics and complexity.

The concept of integrated photonic devices that perform many of the necessary functionalities has been in widespread use in the optical telecommunication industry for

decades. In the field of telecommunications, these benefits together with the potential for easy mass manufacturing make them very attractive.

An ongoing effort has been made to bring more photonic technologies into use with astronomical observatories (Bland-Hawthorn and Kern, 2009; Minardi et al., 2021; Labadie, 2022). Specific requirements and applications in astronomy make an unmodified adaptation of telecommunication devices unfeasible, but adapted and specialized *astrophotonic* devices can have an impact in selected use cases. A noteworthy example is the photonic beam combiner employed by Gravity (GRAVITY Collaboration et al., 2017) as arguably the first photonic centerpiece component in a major state-of-the-art instrument.

The main goal of this development is to improve the efficiency of modern observatories. Similarly to the advantages of photonic technologies in telecommunication, using astrophotonics concepts can potentially reduce the instrument footprint while reducing the complexity of the system.

The field of astrophotonics is very wide since many of the conventional optical components can potentially be replaced or supplemented by photonic counterparts. The search for the best use cases in which technology might bring the greatest advantages is continuing.

In the context of this work, the concepts that aim to integrate or replace parts of AO systems are the most important to mention. The following is an excerpt from a publication submitted by a large number of experts in the field of astrophotonics. Under the leadership of Nem Cvetejovic, a thorough overview was written on the current status of the field and the challenges that need to be solved in order for the technology to mature.

2023 Astrophotonics Roadmap: pathways to realizing multi-functional integrated astrophotonic instruments

Excerpt from Jovanovic et al. (2023, under review), section 2: *Symbiosis Between Adaptive Optics and Photonic Components: the Path to Fully Integrated Instruments* by Philipp Hottinger, Olivier Guyon, and Rebecca Jenson-Clem:

“Thanks to excellent AO correction over a small FoV of $\lesssim 50''$ on large telescopes, starlight can now efficiently be coupled into SMFs for high angular and spectral resolution spectroscopy, with an efficiency closely linked to SR. Jovanovic et al. (2017a) achieved coupling efficiencies of over 50% with SRs of 60% in H-Band at Subaru/SCEXAO, Crass et al. (2020) of more than 35% in Y- and J-Band with LBTI/iLocater, and Delorme et al. (2021) aim to reach coupling efficiencies of 60% in K- and L-Band with Keck2/KPIC. Photonic single-mode components extend SMF use to multiple telescopes (GRAVITY Collaboration et al., 2017), and compact integral-field spectroscopy with approaches including hexabundles (Bland-Hawthorn et al., 2011), SCAR (Por and Haffert, 2020; Haffert et al., 2020), and 3D-M3 (Anagnos et al., 2021). [...]

“AO subsystems could individually be replaced by maturing photonic technologies, offering identical or enhanced functionalities in a miniaturized and integrated footprint. The manufacturing processes often allow in-situ alignment (Dietrich et al., 2018) which reduces operational complexity and increases optical stability. One of the most promising

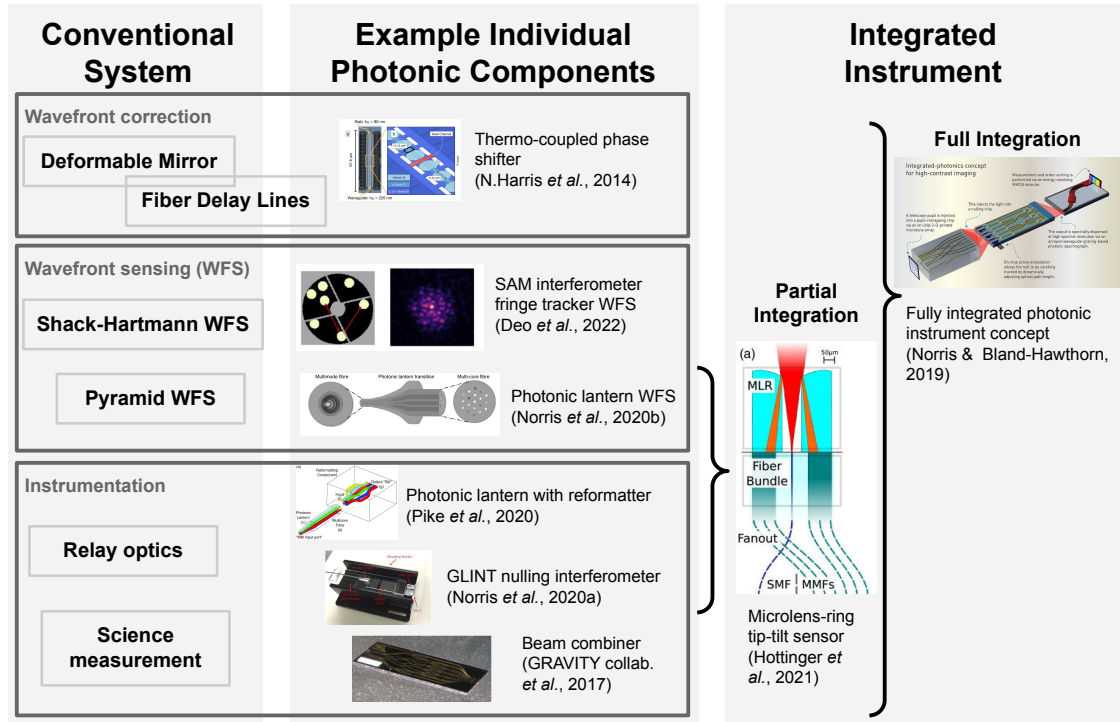


Figure 3.5: Overview of conventional AO systems, potential photonic counterparts and additions, as well as integrated instrumental concepts. Individual components: Thermo-coupled phase shifter (Harris *et al.*, 2014), sparse aperture masking (SAM) interferometry fringe tracker WFS (Deo *et al.*, 2022), photonic lantern WFS (Norris *et al.*, 2020a), photonic lantern with reformatter (Pike *et al.*, 2020), GLINT nulling interferometer (Norris *et al.*, 2020b), Gravity beam combiner (GRAVITY Collaboration *et al.*, 2017), microlens-ring tip-tilt (MLR-TT) sensor (Hottinger *et al.*, 2021), integrated photonic instrument illustration by Phil Saunders (Norris and Bland-hawthorn, 2019). (Reprinted from Jovanovic *et al.*, 2023, under review)

applications is the use of photonic lantern (PL) as focal plane WFS with the potential to supplement well-established pupil plane WFSs. Large systems would benefit from the reduced complexity and smaller footprint of these sensors, enabling better scalability for Multi-Object-AO and Multi-Conjugate-AO systems requiring multiple WFSs. Goodwin et al. (2014) introduced the concept of a miniaturized Shack-Hartmann WFS with similar benefits.

“To optimally exploit photonic technologies, they should not simply replace individual conventional components but rather aim to be integrated as part of the science instrument and the AO system. This type of hybridization will make telescope optics more resource efficient as it reduces optical and mechanical footprint and complexity. One partially integrated approach has been proposed by Dietrich et al. (2017) for reconstructing tip-tilt with a multi-core SMF equipped with a 3D-printed lenslet array and tested on-sky with a refined design utilizing a MLR-TT sensor by Hottinger et al. (2021). There, wavefront sensing is integrated into a vital part of the science instrument, in this case with simultaneous SMF coupling. While tip-tilt sensing is only a limited functionality, it shows the advantages such an integrated approach can have as it reduces complexity by replacing multiple bulk optic components while almost completely eliminating NCPA.

“This interplay between AO and instrument has led to demand and existence of test environments that allow transition of the development from laboratory to on-sky performance in order to mature existing concepts. These are core objectives of the SCExAO test-bench at Subaru (Lozi et al., 2018a) and Canary at WHT (Gendron et al., 2011).”

The MLR-TT sensor

The MLR-TT sensor as introduced in this work stands out as it is arguably the first concept that successfully integrates sensor functionality into an existing part, namely the fiber tip. It is important to particularly mention WFS concepts that utilize PLs (Norris et al., 2020a) or tightly packed fibers (Wright et al., 2022) that show good potential and also aim to integrate sensor functionality as part of an optical fiber.

4 Introducing MLR-TT sensor and KOOL laboratory

The following chapter is a reprint of the publication by Hottinger et al., titled *Micro-lens array as tip-tilt sensor for single-mode fiber coupling*. It is a written proceeding to a presentation at the conference *Advances in Optical and Mechanical Technologies for Telescopes and Instrumentation III* held at *SPIE Astronomical Telescopes + Instrumentation* in Austin, Texas, United States, 2018.

A number of people have been involved in this publication and everybody has made a substantial contribution. I led the manuscript writing, design, and modeling of the micro-lens design and the sensor response, as well as laboratory modification.

Summary and context

This publication gives a general overview of the novel MLR-TT sensor that is a further development based on a micro-lens array (MLA) sensor concept proposed by Dietrich et al. (2017). The sensor's working principles are described and its advantages over existing conventional solutions are discussed.

The lenslet is referred to as an array due to its predecessor, but is, in fact, more accurately described by a ring of lenses. For that reason, it was later renamed to micro-lens ring (MLR) as a more precise description of the physical layout and emphasizes the difference to the predecessor. The usage of an MLR means that a central aperture leaves most of the beam unmodified when the beam is aligned, eliminating the necessity to modify the existing optical system (see Sec. 4.5.1).

The MLR-TT sensor is designed to be tested at the iLocator spectrograph fiber coupling front-end (see Chapter 6). The motivation for detecting and correcting for tip-tilt aberrations is discussed, including the presentation of the previous residual tip-tilt measurements by iLocator.

A preliminary optical design of the MLR is presented as well as the modeled sensor response. The lens optimization and the sensor response are both modeled with geometric optics in *Zemax Optics-Studio* as introduced in Sec. 2.1.1. As outlined in the following chapters, laboratory measurements show that this was not sufficient (see Sec. 5.3 and Sec. 6.2.4) but it should be complemented by wave propagation simulation (see Sec. 7.8).

Furthermore, the Königstuhl Observatory Opto-Mechatronics Laboratory (KOOL) was first introduced as a collaboration between Max Planck Institute for Astronomy (MPIA), Institute for System Dynamics Stuttgart (ISYS), and Landessternwarte (LSW) that was later used for setting up and testing the MLR-TT sensor system.

Proceeding to SPIE, 2018: Micro-lens array as tip-tilt sensor for single-mode fiber coupling

(Reprinted with adapted formatting)

P. Hottinger, R. J. Harris, P.-I. Dietrich, M. Blaicher, M. Glück, A. Bechter, J.-U. Pott, O. Sawodny, A. Quirrenbach, J. Crass, and C. Koos. Micro-lens arrays as tip-tilt sensor for single mode fiber coupling. In R. Geyl and R. Navarro, editors, *Advances in Optical and Mechanical Technologies for Telescopes and Instrumentation III*, volume 1070629, page 77. SPIE, July 2018. ISBN 978-1-5106-1965-4. doi: 10.1117/12.2312015

Abstract

We introduce a design for a tip-tilt sensor with integrated single-mode fiber coupling for use with the front-end prototype of the iLocator spectrograph at the Large Binocular Telescope to detect vibrations that occur within the optical train. This sensor is made up of a micro-lens array printed on top of a fiber bundle consisting of a central single-mode fiber and six surrounding multi-mode fibers. The design is based on a previous prototype that utilized a multi-core fiber with seven single-mode fibers (Dietrich et al., 2017). With this updated design, we are able to achieve a better sensing throughput. We report on the modeled performance: if the beam is perfectly aligned, 69% light is coupled into the central single-mode fiber feeding the scientific instrument. When the beam is not aligned, some of the light will be coupled into the outer sensing fibers, providing the position of the beam for tip-tilt correction. For this design we show that there is a linear response in the sensing fibers when the beam is subject to tip-tilt movement. Furthermore we introduce an adaptive optics testbed, which we call the Koenigstuhl Observatory Opto-mechatronics Laboratory (KOOL), this testbed currently simulates vibrations at the Large Binocular Telescope, and in collaboration we have extended it to allow single-mode fiber coupling tests.

4.1 Introduction

For many years the image quality of ground based telescopes was limited by the atmosphere, known as the seeing limit. However, recent advances in modern adaptive optics (AO) systems are allowing 8-10 m class telescopes to achieve better imaging quality, leading to new and exciting discoveries. In particular ExAO can allow diffraction limited imaging in certain circumstances. Examples of these systems include FLAO at the Large Binocular Telescope (LBT, 2x8.4 m; Esposito et al., 2011), GPI at the Gemini South Observatory (8.2 m; Macintosh et al., 2014), SCExAO at the Subaru Telescope (8.2 m; Jovanovic et al., 2015) and SPHERE at the Very Large Telescope (VLT, 8.2 m; Beuzit et al., 2008).

Conventional fiber-fed spectrographs use MMFs as the different modes of the telescopes PSF need to be propagated. Yet, improved developments in AO open up the new possibility to use spectrographs fed by SM fibers, instead of larger MMFs. Due

to the smaller entrance aperture, or slit, these spectrographs can be reduced in size, reducing stability constraints and are also free of conventional modal noise (Crepp et al., 2016). Several attempts have been made to couple SMFs to these large telescopes, but the coupling efficiency is strongly affected by the quality of initial fiber alignment, as well as beam drifts and higher-frequency tip-tilt motions due to telescope or instrument mechanics and vibrations.

Conventional tip-tilt sensing solutions include imaging of the PSF on a quad-cell detector (Esposito et al., 1997), imaging a pinhole mirror, using the telescopes AO system, or accelerometer based disturbance feed-forward control (Glück et al., 2017). Yet, these approaches can suffer from fundamental limitations that limit their accuracy. These include non-common path (NCP) vibrations, limited dynamical range, low response speed and additional throughput losses. In this work we introduce a tip-tilt sensor consisting of a MLA printed on top of a fiber bundle that overcomes many of these limitations. The design is optimized to perform both tip-tilt sensing using MMFs and simultaneously couple light into a SMF to feed the spectrograph.

This concept is based on a prototype device introduced by Dietrich et al. (2017) but uses MMFs for sensing to improve sensitivity. The MLA will be printed on top of the fiber bundle by in-situ two-proton lithography to produce these free-form lenses and achieve high alignment precision (Dietrich et al., 2018). The design is optimized to be installed in the front-end prototype of the iLocator spectrograph at the LBT to increase SMF coupling efficiency.

In Sec. 4.2 we introduce the iLocator spectrograph, its optical properties and a short analysis of its tip-tilt vibration challenges. Sec. 4.3 describes the preliminary design of the tip-tilt sensor taking into account the requirements of the telescope and instrument including its modeled performance and manufacturing plans. Sec. 4.4 introduces the AO testbed, KOOL where we are performing tests for SMF coupling and tip-tilt sensing. This is followed by Sec. 4.5, which outlines advantages and a comparison to a first prototype described by Dietrich et al. (2017), and Sec. 4.6 summarizes and highlights future work.

4.2 Design considerations

We are developing the tip-tilt sensor to be integrated with the SMF coupling front-end prototype for the iLocator spectrograph. For this it is essential to understand the instrument and its requirements.

This section gives an overview over the iLocator spectrograph (Sec. 4.2.1), its requirements for SMF coupling (Sec. 4.2.2) and the observed vibrations (Sec. 4.2.3).

4.2.1 iLocator spectrograph

iLocator is a high resolution spectrograph for the LBT (Crepp et al., 2016). A fiber injection system feeds the cross-dispersed Echelle spectrograph that operates in the YJ-bands (0.97-1.27 μm). The instrument will deliver a high spectral resolving power ($R \sim 150,000$).

Unlike most conventional high resolution spectrograph, it will be fed by SMFs. For this, light from both 8.4m diameter telescopes of the LBT is corrected by the LBTI AO system (Hinz et al., 2012) and then coupled into the SMFs. The spectrograph accommodates three spectroscopic input channels: one for each telescope and one for the wavelength calibration source fed by a Fabry-Pérot etalon calibration system for radial velocity precision below 10 cm/s (Stürmer et al., 2017).

Using SMFs to feed the spectrograph yields several advantages over traditional MMFs. SMFs feature a smaller output aperture and a lower NA, leading to a compact instrument design while achieving high spectral resolution. The iLocator spectrograph will have a footprint of 50 cm squared (Crepp et al., 2016). When compared with other spectrographs on 8 m class telescopes (e.g. Pepe et al., 2010) this is small, reducing cost and increasing stability. Furthermore, SMFs are free of conventional modal noise, though recent studies have shown that polarization may also cause noise in a high resolution spectrograph (Halverson et al., 2015).

4.2.2 Single mode fiber coupling

While SMFs offer many advantages, efficient light coupling from a telescope into the fibers can prove to be a challenging task and several requirements have to be considered. Within a SMF, light will propagate in only one mode, the fundamental mode with a near-Gaussian intensity profile. Its width (MFD) and the relative refractive indices of the core and cladding govern the NA of the light exiting or entering the fiber as approximated by a Gaussian beam.

The beam from the telescope on the other hand is most similar to an Airy pattern due to diffraction at the primary mirror (though this is slightly altered by secondary obscuration, spiders etc.). The NA at the fiber coupling plane is set by the telescope optics. This diffraction pattern and the NA need to be closely matched with the fundamental mode of the SMF to achieve maximum coupling efficiency. This can be calculated by the overlap integral of the incoming beam and the accepted near-Gaussian intensity profile. As there is still a fundamental mismatch between the Airy intensity distribution and the fundamental mode, the theoretical maximum coupling efficiency is $\sim 80\%$ (Shaklan and Roddier, 1988) without efforts such as pupil apodization attempting to overcome this limitation (Guyon, 2003).

Fig. 4.1a shows the intensity profile of both the Airy pattern of an idealized telescope (red) and the fundamental mode of the fiber (blue) as modeled with the optical design software Zemax (see Sec. 4.3.1), optimized for a SMF with MFD of $5.8 \mu\text{m}$ ($1/e^2$ intensity). Note, as the diffraction limit is usually measured as distance between maximum and first minimum, the size of the diffraction limited PSF is defined somewhat larger ($\sim 10 \mu\text{m}$ diameter between first minima). If the incoming beam is not perfectly aligned to the fiber, the coupling efficiency is further reduced. This is plotted in Fig. 4.1b for a beam gradually misaligned from the SMF by decentering its centroid position, showing a rapid decrease in coupling efficiency. With a beam displacement of $2.8 \mu\text{m}$ corresponding to the mode-field radius of the SMF, the coupling efficiency is reduced to $\sim 26\%$. This shows the precision that is necessary to efficiently couple light from the telescope into

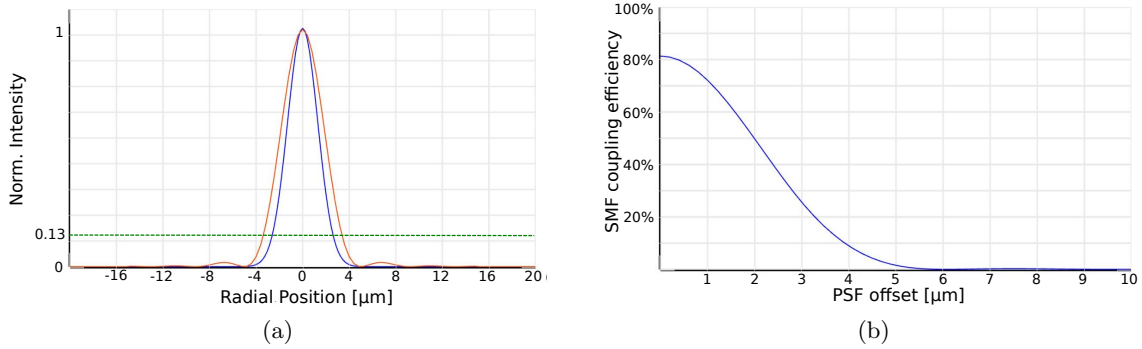


Figure 4.1: Simulated single-mode fiber (SMF) coupling for a mode-field diameter (MFD) of $5.8\ \mu\text{m}$ ($1/e^2$ intensity). Image (a) shows the cross section of the intensity profile for both the fundamental mode of a single-mode fiber (blue) and a diffraction limited point spread function optimized for maximum coupling efficiency into that SMF (red). The green dashed line indicates the $1/e^2$ -intensity (13% of the maximum). Image (b) shows the coupling efficiency if the incoming beam is gradually misaligned with respect to the fiber by shifting the centroid of the point spread function (PSF), resulting in a rapid decrease in coupling efficiency with position. (Reprinted from Hottinger et al., 2018)

the SMF and the large impact a slight misalignment has on throughput.

As the SMF chosen for the iLocator instrument has a MFD of $5.8\ \mu\text{m}$ ($1/e^2$ -diameter) the incoming beam must be optimized for coupling to this. For this, the F/15 beam of the LBT and the diffraction pattern of 60 mas at a wavelength of $1\ \mu\text{m}$ (diameter to the first minima) are re-imaged by the iLocator front-end (Bechter et al., 2015).

4.2.3 Tip-tilt vibrations

It is well known that the LBT, as most telescopes, suffers from vibrations (Brix et al., 2008). This effect is particularly pronounced when ExAO is used, as the vibration relative to PSF size is larger. When testing SMF injection for iLocator with a prototype front-end bench in 2015, coupling of up to 25% was shown (Bechter et al., 2016). This was lower than the theoretical maximum of $\sim 80\%$ (Shaklan and Roddier, 1988) due to several reasons. Extensive tests have shown that most of this is accounted to vibrations throughout the telescope and the fiber injection bench. These vibrations cause tip-tilt wavefront aberrations leading to a movement of the PSF on the focal plane and thus preventing more efficient fiber coupling.

The following data is based on images taken by an ANDOR Zyla 5.5 camera set up at the imaging arm of the iLocator front-end working in a wavelength range between 700 nm and 970 nm (Bechter et al., 2016). The exposure time is $\sim 1\ \text{ms}$ and the sampling

frequency is ~ 125 Hz.

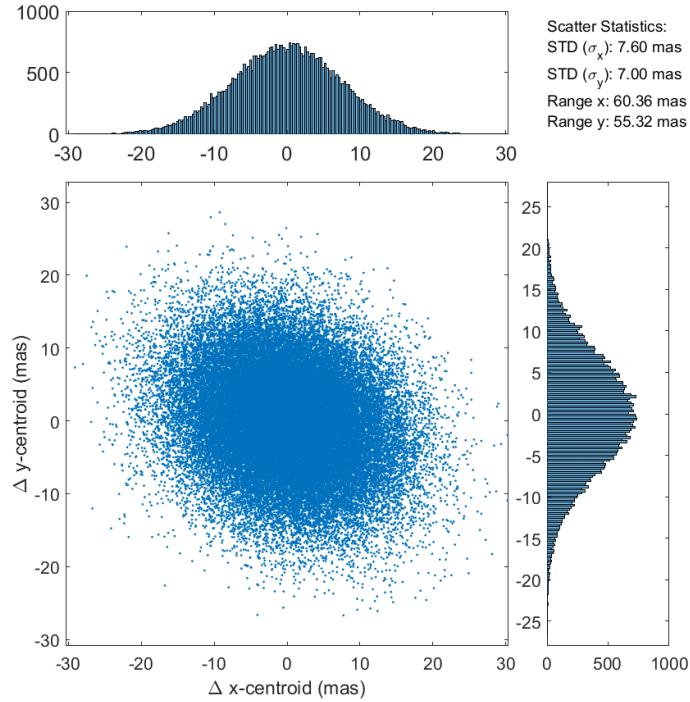


Figure 4.2: Scatter plot of the location of the PSF centroid for each exposure and the corresponding distributions. The wavelength range of 700 nm to 970 nm was imaged by the iLocator front-end prototype as described in Bechter et al. (2016). The diameter of the diffraction limited PSF is ~ 60 mas. (Reprinted from Hottinger et al., 2018)

Fig. 4.2 shows the position of the PSF center for each exposure, both as scatter plot on the image plane and as distribution for each axis. The PSF is misaligned with respect to its mean position by up to 60 mas, corresponding to more than one diffraction limited PSF diameter, leading to loss due to inefficient fiber coupling as outlined in Sec. 4.2.2. To optimize throughput, these tip-tilt vibrations need to be sensed and corrected.

Fig. 4.3 shows stacked images of the PSF. Image (a) shows the sum of all exposures simulating a longer exposure time. Image (b) also shows the sum of all exposures but with the image shifted in such a way that the center of a fitted Gaussian is held constant, effectively simulating a perfect tip-tilt correction. The red circle indicates the diffraction limit at the working wavelength (~ 850 nm). These images illustrate that despite working near the diffraction limited regime, tip-tilt vibrations can smear out the PSF and lead to a seeing limited result complicating SMF coupling. Note that even for the tip-tilt corrected image (b), higher order aberrations are visible. These are most likely static

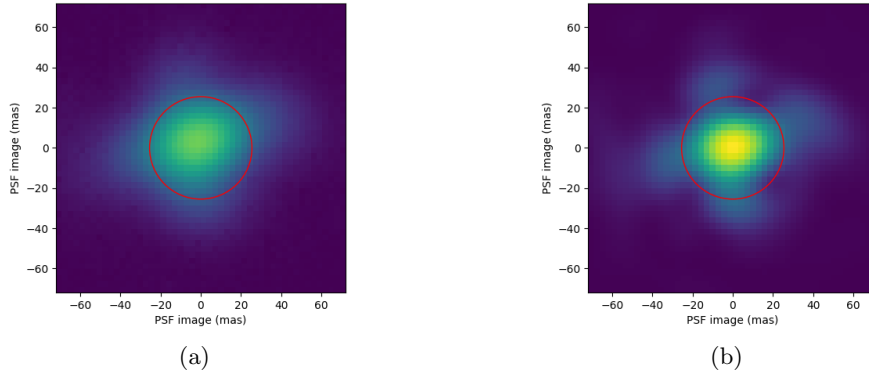


Figure 4.3: Averaged Point Spread Function from the LBT, with (a) no tip-tilt compensation and (b) with tip-tilt compensation calculated by holding the center of a fitted Gaussian constant. Both images have logarithmic intensity scaling and are normalized to the highest pixel value. The red circle denotes the Airy disk diameter at 850 nm, indicating that with vibrational compensation the coupling will be higher. It can also be seen from b) that aberrations in the system need to be compensated for.

(Reprinted from Hottinger et al., 2018)

NCP aberrations that also need to be corrected.

4.3 Preliminary design

To optimize coupling into the SMF and therefore throughput, the tip-tilt motions of the incoming telescope beam as described in Sec. 4.2.3 need to be sensed and corrected for. There are some conventional methods that have been used to do such tip-tilt sensing, yet these can have some fundamental limitations (see Sec. 4.1 and Sec. 4.5).

In this work we present an innovative method for tip-tilt sensing, based upon the work in Dietrich et al. (2017). This sensor consists of a micro-lens array (MLA) printed on top of a fiber bundle made up of a central SMF (MFD of $5.8\ \mu\text{m}$) and six surrounding MMFs (core diameter of $50\ \mu\text{m}$, NA of 0.22) arranged in a hexagonal array with a pitch of $125\ \mu\text{m}$. The MLA itself covers just all fiber cores, has a diameter of $300\ \mu\text{m}$ and a height of $\sim 400\ \mu\text{m}$. The central SMF serves as the fiber that will feed the spectrograph, while the tip-tilt sensing signal will be provided by coupling into the surrounding MMFs. Fig. 4.4 shows a 3D model of this system.

Fig. 4.5 illustrates the working principles of the tip-tilt sensor. It shows the cross-section of the MLA model for four different incoming beam positions indicated by the captions. Image (a) shows a beam perfectly aligned with the SMF. In this case 69% of the light is coupled into this fiber. Only some light will be refracted evenly to the

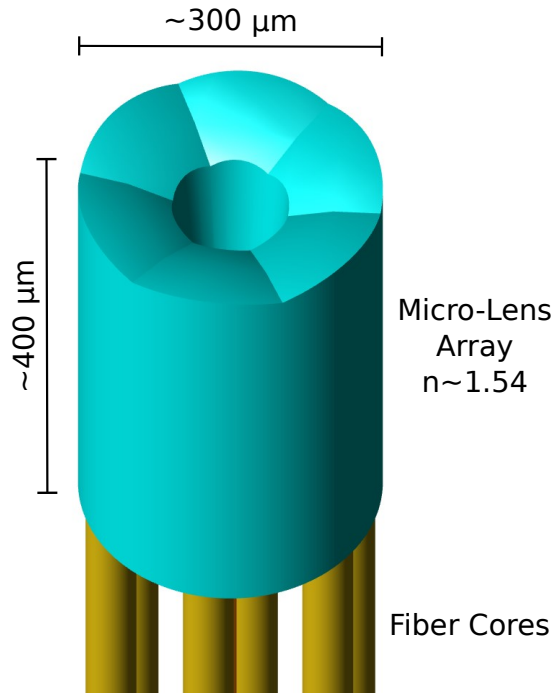


Figure 4.4: Design model of a micro-lens array (MLA) tip-tilt sensor for the front-end prototype of the iLocator spectrograph. The MLA is printed on top of a fiber bundle made of a central single-mode fiber (SMF) (not visible) and six surrounding multi-mode fibers (MMFs) (only fiber cores shown). While the central optical path to the SMF is unobscured, off-centered light will be refracted by the MLA to be coupled into the surrounding sensing MMFs. The pitch between the fiber cores is $125\ \mu\text{m}$. Diameter and height of the MLA are $300\ \mu\text{m}$ and $400\ \mu\text{m}$, respectively. (Reprinted from Hottinger et al., 2018)

six surrounding MMFs. Image (b) shows a slightly misaligned beam, where most of the light is still coupled into the central SMF but more light is coupled into the outer sensing fibers in direction of the decentered beam. In this regime, real time tip-tilt sensing and correction will take place. Image (c) and (d) show even more misaligned beams with hardly any coupling into the central SMF but successively more light coupling into the sensing fiber. As hardly any light is coupled into the SMF if the beam is misaligned this much, this regime is not favorable for real-time correction. Nevertheless, this illustrates the wide dynamical range of the sensor, extending its use to initial fiber and target alignment.

The following section will outline its modeled performance, design considerations (Sec. 4.3.1), correction method (Sec. 4.3.2) and manufacturing plans (Sec. 4.3.3).

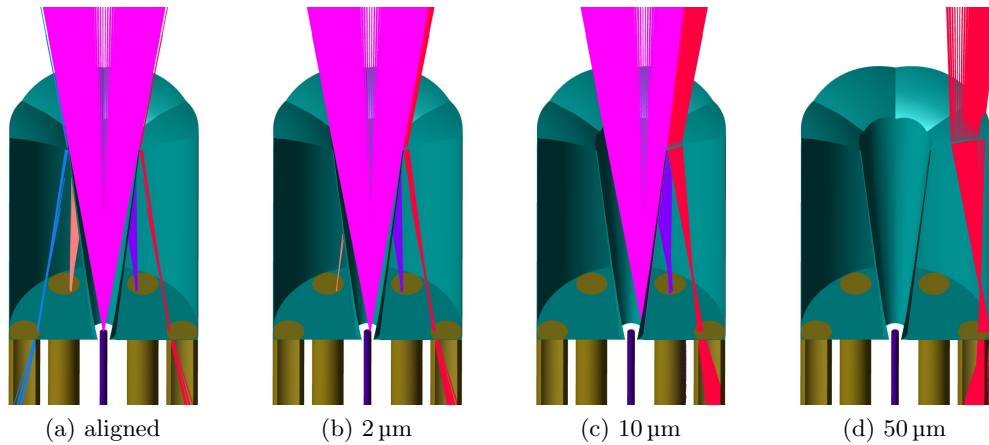


Figure 4.5: Cross section of the micro-lens array (MLA) tip-tilt sensor with incoming beam illustrating the working principle of the device. The color of the rays indicate which fiber the light is coupled into: the central single-mode fiber (SMF) feeding the spectrograph (purple, number of rays does not correspond to coupling efficiency) and the outer sensing multi-mode fibers (MMFs) (red, violet, orange, blue). Rays that are refracted by the MLA and are not coupled into any fiber are not illustrated. If the beam is perfectly aligned **(a)**, most of the light is coupled into the central SMF with some of the rest coupled into the outer sensing MMFs. As the beam is decentered by $2\ \mu\text{m}$ **(b)**, coupling efficiency into the SMF decreases but is still significant while the sensing signal in the outer MMFs increases. For large misalignments of $10\ \mu\text{m}$ **(c)** and $50\ \mu\text{m}$ **(d)** no light is coupled into the central SMF but successively more light is coupled into the sensing MMFs illustrating the wide dynamical range the tip-tilt sensor covers.

(Reprinted from Hottinger et al., 2018)

4.3.1 Modeling

To optimize the MLA and to model its performance, extensive tests were conducted. These were performed with the optical design software Zemax-OpticStudio. *Zemax OpticStudio* uses a ray tracing algorithm for lens design. This is usually not suitable for simulating coupling into SMFs as they do not take into account wave properties of the incoming beam. The wave nature of the beam is of fundamental importance as it forms the diffraction pattern described by wave optics that is responsible for matching the incoming telescope beam to the fundamental mode of the SMF (see Sec. 4.2.2). Because of this, the *Physical Optics Propagation* capabilities of *Zemax OpticStudio* were used which take into account both Gaussian and wave optics for SMF coupling while the ray tracing capabilities were used for MMF coupling.

Sensing performance

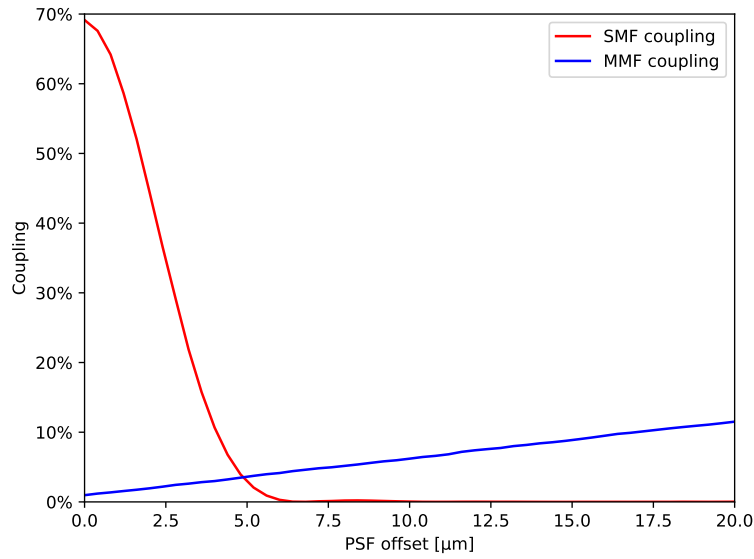


Figure 4.6: Modeled coupling into the SMF (red line) and into the sensing MMF (blue line) for an incoming beam moving from a perfectly aligned position along an axis to this sensing fiber.

(Reprinted from Hottinger et al., 2018)

The modeled coupling efficiencies are shown in Fig. 4.6, with the red line showing the fiber coupling efficiency for the central SMF and the blue line showing the coupling efficiency for one of the sensing MMF as the incoming beam is decentered. The coupling efficiency for the central SMF decreases rapidly as the beam is decentered. When the beam is misaligned by 5 μm, corresponding to the $1/e^2$ -MFD of the modeled fiber, total coupling has already decreased to <5%, which is similar to a standalone SMF (see Sec. 4.2.2). The coupling into the sensing MMF increases linearly starting at ~1% for an aligned beam to roughly 20% for an offset of 20 μm. As the signal for this offset is linear, this design should prove to be easy to integrate with the existing tip-tilt mirror in the iLocator front-end prototype.

Off-axis performance

To examine the performance if the beam is not aligned along an axis of a sensing MMF, the sensing signal is modeled for such misaligned beams. This is plotted in Fig. 4.7b showing a misaligned beam scanning along eleven different axes ranging from alignment to the MMF axis to a rotation of 60° corresponding to the next sensing fiber. This is illustrated on the model in Fig. 4.7a. The linear response that was already observable in Fig. 4.6 is seen to extend up to a misalignment of 70 μm. This is valid for both the aligned beam (0°, blue) and a beam centered exactly between two MMFs (30°, red).

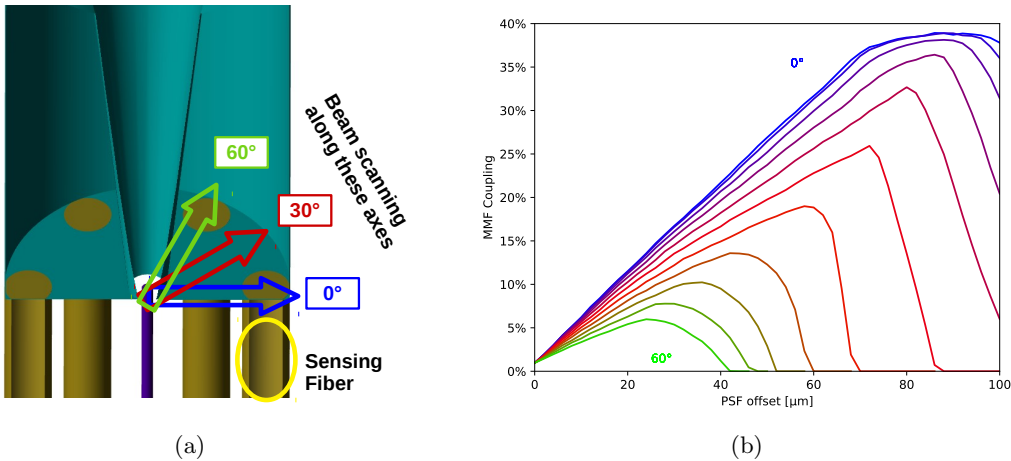


Figure 4.7: Off-axis performance of the MLA tip-tilt sensor. Modeled coupling for one sensing MMF for an incoming beam moving from an aligned position outwards. This is illustrated in the image (a): The rightmost fiber is sensed while the beam is decentered from the center in different directions indicated by the colored arrows. The different lines in image (b) correspond to these different directions of this tip-tilt motion, ranging from 0° (blue) to 60° (green) in steps of 6° and in reference to the sensing MMF. (Reprinted from *Hottinger et al., 2018*)

This very wide dynamical range enables the usage for not only real-time tip-tilt sensing, but also for initial fiber and target alignment where a large dynamical range is favorable.

A similar analysis was performed to evaluate the sensing response of all MMFs for a misaligned beam. This is shown in Fig. 4.8b with a schematic in Fig. 4.8a illustrating the procedure. As the beam moves towards the rightmost fiber (blue), coupling is measured for all six sensing fibers (two are not shown in the illustration) numbered by the angular position in respect to the rightmost fiber. All signals show an initial linear response with different slopes allowing reconstruction of the actual beam position. As there is an initial response in all sensing fibers, some errors signals from other aberrations or detector noise can be filtered.

Central aperture

The MLA was designed such that $\sim 70\%$ of the total intensity is coupled into the central SMF if the beam is aligned. This is less than the theoretical maximum of $\sim 80\%$ (Shaklan and Roddier, 1988) and is due to the fact that the central void part of the lens, i.e. the unobscured area in front of the SMF, is smaller than necessary for maximum coupling efficiency. This way, a sensing signal in the MMF can be provided even if the beam is aligned, thus providing stability as sensing can be performed even for a very small

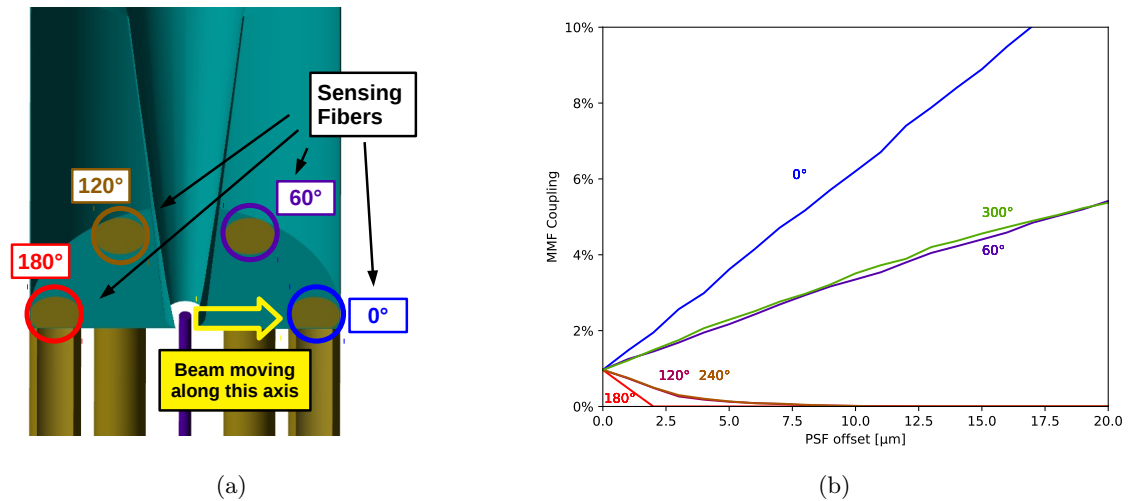


Figure 4.8: Sensing signal for each MMF as the incoming beam moves from an aligned position outwards as illustrated in image (a) (two fibers are not shown). Image (b) shows the signal as function of the misalignment. The signal of the three fibers in direction of the beam increases linearly while the signal on the opposite fibers decreases linearly.
(Reprinted from Hottinger et al., 2018)

beam offset. Fig. 4.9 shows a range of possible choices for the diameter of the central aperture between 100 μm (blue) to 130 μm (green). If the systems requirements demand a higher sensing signal or on the contrary a higher SMF coupling, the design may be adjusted accordingly. For a reasonable trade-off, we have decided on a central aperture of $\sim 120 \mu\text{m}$ that yields both good coupling ($\sim 70\%$) and a good sensing signal even for an aligned beam ($\sim 1\%$).

4.3.2 Tip-tilt correction

The MLA tip-tilt sensor described in this section provides a signal indicating that the incoming beam is misaligned. This sensor signal will then be transformed into a correction signal which feeds a tip-tilt mirror within the iLocator front-end prototype. The sensor and the mirror will then be able to correct in real-time and closed-loop. To read out the sensing fibers, a fast, low-noise photo-detector can be used such that the correction frequency is governed by the photon count of the science target.

As mentioned in Sec. 4.3.1, there is a response in all six sensing fibers if the beam is decentered. This enables the development of an interaction matrix which takes into account possible error signals that occur due to other aberrations than tip-tilt as well as background noise.

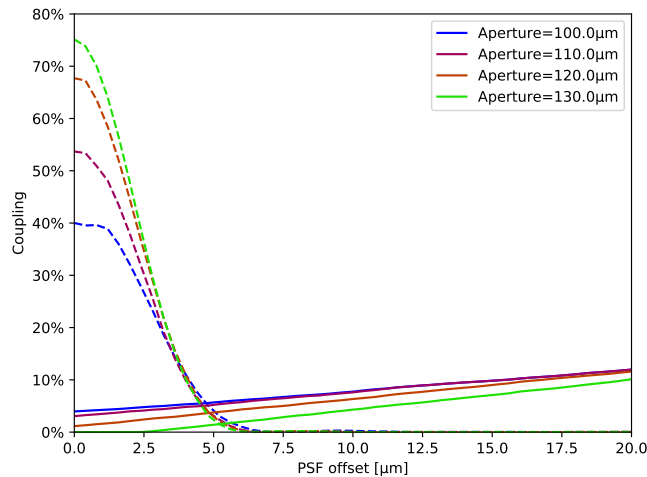


Figure 4.9: Tip-tilt sensor performance for different central apertures ranging from $100\ \mu\text{m}$ (blue) to $130\ \mu\text{m}$ (green) in diameter. Dashed lines correspond to central SMF coupling and solid lines to sensing MMF coupling. For larger central apertures, the maximum coupling efficiency into the SMF increases but the sensing signal decreases. This trade-off between maximum coupling and sensing sensitivity needs to be evaluated and chosen to fit the requirements of the system.

(Reprinted from *Hottinger et al., 2018*)

4.3.3 Manufacturing

Current approaches for fabricating individually lensed fibers rely on grinding (Szu-Ming Yeh et al., 2005), etching (Eisenstein and Vitello, 1982) or melting techniques (Presby et al., 1990). These require complex fabrication processes that are not well suited for multi-core fibers (MCFs) or compact fiber bundles. In order to fabricate these, MLAs can be glued onto the fibers. These lenses, however, must be aligned with the fibers in three or six degrees of freedom, thereby considerably complicating the assembly, particularly for SM fibers, where alignment tolerances are very stringent.

Recently it has been demonstrated, that in-situ fabricated beam-shapers allow ultra low-loss coupling for a variety of application (Dietrich et al., 2018) including astrophotonics (Dietrich et al., 2017). This technology makes use of 3D-lithography by two-photon polymerization of a commercial IP-resist by Nanoscribe. This solves several problems: Due to the flexibility of 3D-lithography lens designs can be adapted rapidly to any requirements of the optimal system, ensuring best possible coupling. This is particularly useful if the cores of the MCF or fiber bundle are not regularly spaced. Additionally, the in-situ fabrication of lenses circumvents tedious alignment steps. Additionally, free-form lenses can be formed in shapes that are difficult to manufacture using conventional methods. They do not require any adhesives that may decrease both short-term and long-term stability.

4.4 KOOL: AO system testbed

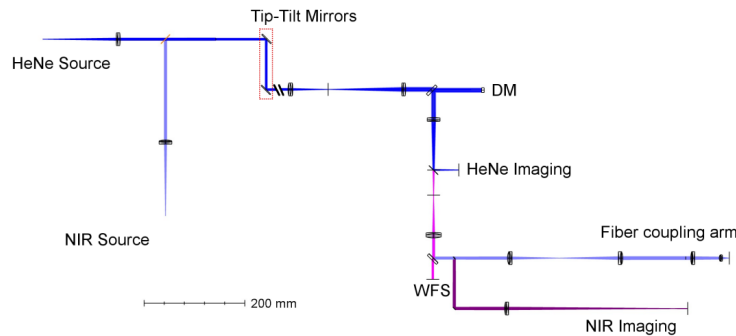


Figure 4.10: Design layout of the Königstuhl Observatory Opto-Mechatronics Laboratory (KOOL). This adaptive optics (AO) testbed allows simulation and correction of LBT vibrations with two tip-tilt mirrors and higher order aberrations with an ALPAO deformable mirror (DM). A HeNe Source (632 nm) is used in the main setup including the wavefront sensor (WFS) (purple) and an imaging arm (dark blue). A near-infrared (NIR) (1.31 μm) source feeds both a fiber coupling arm (light blue) and a separate imaging arm (violet). Both sources are SMF-fed.

(Reprinted from *Hottinger et al., 2018*)

We have developed an optical testbed for performing realistic tests for vibration correction and single-mode fiber coupling in large telescopes, which we call Königstuhl Observatory Opto-Mechatronics Laboratory (KOOL). This is a collaboration between the MPIA in Heidelberg, Germany, ISYS in Stuttgart, Germany and the Landessternwarte Heidelberg (LSW, part of Zentrum für Astronomie der Universität Heidelberg) in Heidelberg, Germany.

Fig. 4.10 shows the schematics of the setup. This testbed is separated into two sections. Beam manipulation optics make use of several opto-mechanical components to generate and manipulate a test beam that will simulate an incoming telescope beam. A first tip-tilt mirror can introduce vibrations up to 50 Hz into the optical system, which can be similar to the PSD of the LBT. Furthermore, the mirror is equipped with several accelerometers to test the disturbance feed-forward control in real time (Glück et al., 2017). Based on the accelerometers the low order aberrations as piston, tip and tilt can be estimated on-line by a linear filter. A second tip-tilt mirror as well as the DM can be used for the compensation of the vibrations. The frequency range of the tip-tilt correction is up to 1 kHz. A phase screen (not shown) is also available and can introduce atmospheric aberrations with variable speed. The DM is able to either correct for those aberrations in closed-loop or it can itself introduce desired aberrations to simulate a certain environment or a known telescope PSF. For both closed-loop operation, as well as for wavefront quality control, this setup includes a WFS and a camera for imaging the

PSF. All beam manipulation and closed loop operation is performed with a SMF-fed HeNe source (632nm).

A second, near-infrared (NIR) source (1.31 μm) is also fed into the system with a dichroic mirror. It passes through the AO system and it is then again reflected by a dichroic mirror, entering the fiber coupling section. This section consists of a fiber coupling arm to test and characterize SMF coupling and the final MLA tip-tilt sensor. By using a beam splitter, the NIR source is also imaged onto a camera to compare fiber coupling results to the PSF.

4.5 Discussion

Other options to sense tip-tilt aberrations include a pinhole mirror near the focal plane to reflect any misaligned light, a beam splitter or dichroic mirror to image the PSF on a charged-coupled device (CCD) or quad-cell detector (Esposito et al., 1997), the AO system of the telescope, or an accelerometer based feed-forward control (Glück et al., 2017), where the accelerometers are mounted at the telescope mirrors and the reconstructed low order aberrations are used for compensation in a disturbance feed-forward combined with the AO system. Yet, the MLA tip-tilt sensor design introduced in this work yields many advantages but also some challenges. To compensate for difficulties it is also possible to combine different approaches. Such a system could combine a feed-forward system for rough tip-tilt compensation and the MLA tip-tilt sensor for closed-loop high precision correction.

Throughput The MLA tip-tilt mirror will couple almost all light into the SMF if the beam is aligned. This can be increased in trade-off for sensitivity (see Sec. 4.3.1). When imaging the PSF using a beam splitter, some light needs to be diverted and is therefore not available for coupling. This is not the case when using a dichroic mirror as sensing is done in a different wavelength range. There will also be no losses when using either the telescope AO system as no additional light is diverted or when using an accelerometer based feed-forward system as no light is detected all together. When using a pinhole mirror, the alignment precision of the pinhole to the SMF will govern its throughput and can lead to large losses.

Vignetting Light may be vignetted by a pinhole in front of the focal plane causing reduced coupling. This is especially worth considering as the pinhole mirror needs to reflect the beam at an angle leading to an elliptical aperture. The MLA tip-tilt sensor also suffers from vignetting as the central unobscured area in front of the SMF acts as an aperture. However, this can be modeled reliably as in-situ printing of the MLA assures good alignment and its circular shape assures symmetry. All PSF imaging, AO correction and feed-forward control will not lead to any vignetting.

Range The dynamical range is rather large on all afore mentioned options. An exception is the AO system of the telescope as a large tip-tilt error in the wavefront

may already be outside the dynamical range of the WFS. The MLA brings the additional advantage that the sensor provides a linear signal for a very large range. Due to these properties the sensor can also be used for initial alignment on the target.

Sensitivity The MLA tip-tilt sensor ensures excellent sensitivity, though some of it is penalized by a lower maximum fiber coupling efficiency. Additionally, as the sensing MMFs can be read out individually, the possibility to use low-noise read out electronics can further increase sensitivity. As a pinhole in front of the SMF practically needs to be larger than the fiber to assure high throughput, sensing of slight misalignment will not be challenging. Also, when imaging either the pinhole mirror or the PSF directly on a CCD, readout noise will limit the sensitivity. Using a feed-forward system that makes use of an accelerometer will in general be quite sensitive to small amplitude vibrations. The disturbance feed-forward system mainly considers the vibrations in the telescope path. However, vibrations are also introduced in the instrument path. To achieve optimal coupling an additional sensor as the MLA is needed in a closed-loop system for high precision coupling.

Speed Again, as readout electronics can be chosen more freely, fast photo-diodes can be used for the MLA tip-tilt sensor in combination with a simple tip-tilt correction algorithm allowing correction frequencies that are only limited by photon count. All sensors that rely on sensing with a CCD or a quad-cell detector are limited by its readout and signal processing sampling. On the other side, a feed-forward system can also work quite fast as the tip-tilt detection is independent of the photon collection. Therefore the speed limitations only depend on the mechanical dynamics of the sensor and the electronics.

Chromaticity Even though tip-tilt aberrations are known to be achromatic, it is worth while mentioning that imaging the PSF with a dichroic mirror will lead to tip-tilt sensing in a different wavelength range. An accelerometer based approach is also wavelength independent leading to possible chromatic effects. All other tip-tilt sensor options detect in the working wavelength range.

Non-common path aberrations Tip-tilt vibrations that occur between the sensing mechanism and the focal plane can cause most of the fiber coupling inefficiency. This is mostly true for the AO system WFS and any accelerometer that will potentially be much further upstream. Separate imaging of the PSF can also be affected by non-common path aberration, strongly depending on where it is integrated into the optical system. As sensing is done right before the focal plane for both the pinhole mirror technique and MLA tip-tilt sensor, all vibrations throughout the system are detected and can be corrected for. This also leads to the exciting possibility to not only use the MLA for real-time tip-tilt sensing but also to correct for static higher order aberrations. As sensing is done near the focal plane and in the working wavelength range, overall coupling efficiency can be optimized by correcting with the DM. Furthermore, as there is data from one central SMF and

six surrounding sensing fibers available, the optimization algorithm can make use of more data than e.g. a quad-cell detector.

Size and complexity This is one of the main advantages of the MLA tip-tilt sensor. While all other closed-loop systems depend on major modifications of the optical setup, the MLA can be integrated easily without changing the optical train. For this, the fiber bundle with the MLA is placed at the focal plane and readout electronics can be mounted remotely. This compact design reduces complexity and cost of the implementation into the system. On the other hand, design and manufacturing of the fiber bundle and of the MLA itself are more complex but also open up many possibilities as the free-form lenses allow adjustments to a wide range of optical requirements and performance goals.

4.5.1 Comparison to prototype

An initial design and prototype was introduced in 2017 (Dietrich et al., 2017) (3D model shown in Fig. 4.11a). The design in this work is based upon this prototype but incorporates a number of major changes. First of all, the prototype design also refracts the incoming beam when it is aligned to the optical axis and focuses it onto the SMF. The new design from this work offers two major improvements in that regard. By allowing the aligned beam to pass to the fiber coupling plane without refraction, the design from this work offers two improvements. Firstly, the optical path does not need to be modified for the MLA tip-tilt sensor to be integrated into the system. Secondly, this design guarantees maximum performance if the beam is aligned as the optical system is designed for maximum coupling efficiency. Therefore, possible error sources such as reflection, absorption, limited surface quality and chromaticity of the lens material can be disregarded.

Furthermore, the prototype makes use of SMFs for sensing, leading to a sensing signal that is very similar to that of the central SMF that leads to the instrument. This is plotted in Fig. 4.11b. The design introduced in this work, on the other hand, is able to create a linear response because the usage of MMFs allow more tolerances and enable a more efficient fiber coupling (compare to Fig. 4.6). As using SMFs do not offer any advantage for the sensor readout, the only disadvantage of using MMFs is an increased coupling of spatially separated objects or other aberrations than tip-tilt.

4.6 Conclusion

In this work we have introduced a preliminary design for a tip-tilt sensor with integrated SMF coupling that is optimized to be used with the prototype front-end of the SM spectrograph iLocator. This design can be integrated into the existing fiber coupling optics without any modifications. When sensing tip-tilt motion of the incoming beam, modeled performance yields a linear response, which simplifies signal processing correction algorithms. The device can be modified to fit system requirements and performance goals.

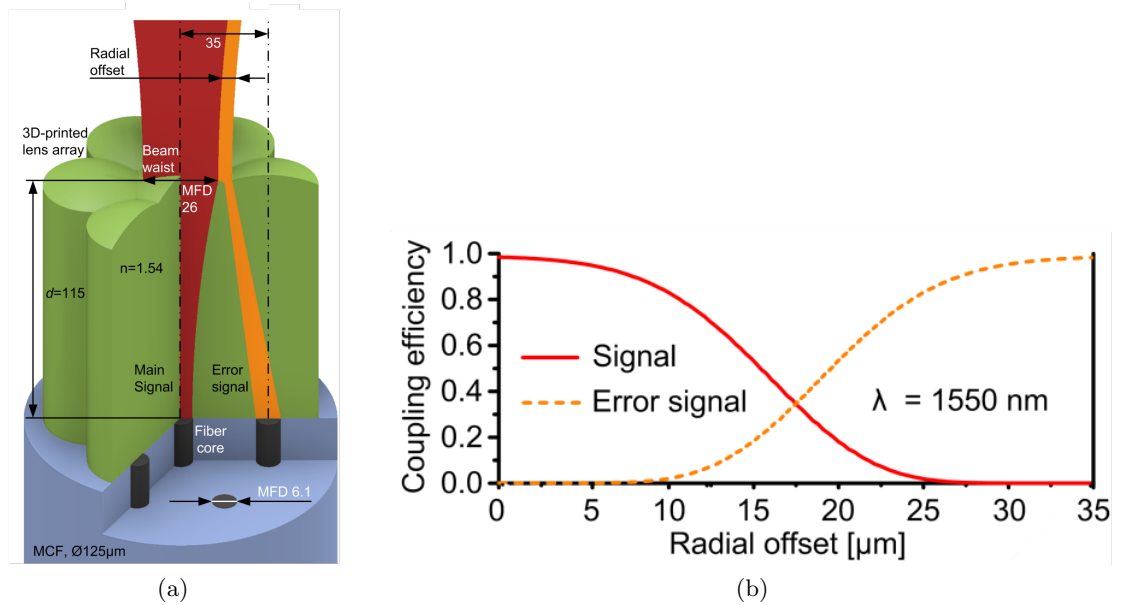


Figure 4.11: Prototype MLA (green) printed on top of a multi-core fiber (MCF) (blue) consisting of seven single-mode fibers (SMFs) (black) as introduced by Dietrich et al. (2017). Image (a) shows a 3D model of the design. Image (b) shows the single-mode fiber (SMF) coupling efficiency normalized to the maximum coupling efficiency for both the the central fiber (red line) and the outer sensing fiber (dashed orange line). Note the different sensing response in comparison to the design introduced in this work as plotted in Fig. 4.6.

(Reprinted from Hottinger et al., 2018, adapted from Dietrich et al., 2017)

We have discussed the advantages of this sensor when compared to conventional tip-tilt sensing options. This includes the compactness of the device, the capability to integrate it into existing optical systems easily, the sensing at the focal plane to avoid NCP vibrations and a higher sensitivity and sampling frequency as detectors can be chosen much more freely. Due to its wide dynamical range, this design can be used for initial fiber and target alignment. Furthermore, it can be used to feed NCP aberration optimization algorithms.

We have also introduced the adaptive optics (AO) testbed KOOL which can be used to introduce and correct LBT vibrations and higher order aberrations. We will use this testbed to test, characterize and optimize this device.

We are currently in the final design stages and will be manufacturing the final device soon. This will be tested at KOOL and then be integrated and tested at the LBT.

Acknowledgments

This work was supported by the Deutsche Forschungsgemeinschaft (DFG) through project 326946494, 'Novel Astronomical Instrumentation through photonic Reformatting'.

This publication makes use of data generated at the Königstuhl Observatory Optomechanics Laboratory (short: KOOL) which is run at the Max-Planck-Institute for Astronomy (MPIA, PI Jörg-Uwe Pott, jpott@mpia.de) in Heidelberg, Germany. KOOL is a joint project of the MPIA, the Landessternwarte Königstuhl (LSW, Univ. Heidelberg, Co-I Philipp Hottinger), and the Institute for System Dynamics (ISYS, Univ. Stuttgart, Co-I Martin Glück). KOOL is partly supported by the German Federal Ministry of Education and Research (BMBF) via individual project grants.

5 Laboratory characterization and integration

The following chapter is a reprint of the publication by Hottinger et al., titled *Focal plane tip-tilt sensing for improved single-mode fiber coupling using 3D-printed microlens-ring*. It is a written proceeding to a presentation given by myself at the conference *Adaptive Optics for Extremely Large Telescopes (AO4ELT6)* held in Québec City, Canada in 2019.

A number of people have been involved in this publication and everybody has made a substantial contribution. I have been responsible for large parts of the manuscript, setting up the system as a whole as well as performing the presented laboratory characterizations.

Summary and context

The proceeding gives an overview of the final design and presents the final MLR hardware, and its response as measured in the lab is presented.

The overall sensor system is described and how it integrates with the iLocator front-end prototype. The sensor integration was tested with the iLocator coupling interface at the University of Notre Dame in Indiana, USA.

Proceeding to AO4ELT6, 2019: Focal plane tip-tilt sensing for improved single-mode fiber coupling using a 3D-printed microlens-ring

(Reprinted with adapted formatting)

P. Hottinger, R. J. Harris, P.-I. I. Dietrich, M. Blaicher, A. Bechter, J. Crass, M. Glück, J.-U. Pott, N. A. Bharmal, A. Basden, T. J. Morris, C. Koos, O. Sawodny, and A. Quirenbach. Focal plane tip-tilt sensing for improved single-mode fiber coupling using a 3d-printed microlens-ring. In *Proceedings of AO4ELT6*, pages 1–7, Dec. 2019

Abstract

Modern extreme adaptive optics (ExAO) systems achieving diffraction-limited performance open up new possibilities for instrumentation. Especially important for the fields of spectroscopy and interferometry is that it opens the possibility to couple light into single-mode fibers (SMFs). However, due to their small size, efficient coupling is very sensitive to the quality of the fiber alignment, beam drifts and higher-frequency tip-tilt aberrations caused by telescope mechanics and vibrations. These residual aberrations are not always sensed and corrected by the AO system, leading to unacceptable losses. This is particularly severe for the Extremely Large Telescopes, where their huge structure will mean vibrations increase and optimal AO solutions are even more difficult to implement.

We have created a focal plane sensor to correct for residual aberrations by surrounding the SMF with six Multi-mode fibers (MMFs). On each of the MMFs sits a printed freeform lens, making up a six-element micro-lens ring (MLR) to refract the light into these surrounding MMFs and thus minimizing light loss in the gap between the fiber cores. This means when the beam is near diffraction limited and centered almost all light couples to the SMF. When the beam is misaligned, it couples to the surrounding cores, which are read out by a detector and processed by the Durham Adaptive Optics Real-Time Control (DARC) software driving a tip-tilt mirror. Currently we are aiming to detect and correct only tip-tilt aberrations. However, choosing to surround the central fiber with six sensing locations potentially allows us to investigate higher order correction modes.

Here we present the design and performance our prototype system. This has been designed for use with the iLocator fiber injection system at the Large Binocular Telescope and can easily be scaled to larger telescopes. We present test results from the KOOL laboratory in Heidelberg and initial integration with the iLocator instrument.

5.1 Introduction

In recent years, the development of advanced AO systems has opened up new possibilities: ever-improved image quality, a wider FoV and greater sky coverage, leading to

new discoveries in fields of astronomy from direct imaging of exoplanets (Rodigas et al., 2014) to examining the motions of the stars around Sgr A* (Gillessen et al., 2009). In particular the development of ExAO has enabled 8-10m class telescopes to achieve diffraction-limited optical performance, where they would otherwise be seeing-limited (Esposito et al., 2011; Macintosh et al., 2014; Beuzit et al., 2008). Whilst the FoV is limited, this enhanced capability has allowed objects to be viewed with far more detail than ever before.

This improvement has also opened new doors in the field of spectroscopy. Conventionally, spectrographs had large entrance apertures, matched to the seeing limit. In the case of fiber fed spectrographs, this meant using MMFs, with core diameters on the order of 100 microns. Due to their large core diameter, the light from the telescope could be efficiently coupled from the telescope, though this formed a large entrance slit to the spectrograph. Due to the instrument scaling laws, the instruments behind had to be appropriately scaled in size (Lee and Allington-Smith, 2000). Using an ExAO system reduces the size of the PSF to the diffraction limit, which in turn allows the size of the fiber core to be reduced. These fibers are called SMFs and by coupling into their smaller entrance aperture and usually smaller NA, the spectrographs that are fed with SMFs can not only be reduced in size, while maintaining the same spectral resolution, but are also free of conventional modal noise (Crepp et al., 2016). This leads to increased stability and reduced cost for the instrument. Whilst in principle this is an ideal solution, it comes at the cost of increased alignment tolerances. In recent years, there have been several attempts to couple light from large telescope into SMFs, but the coupling efficiency highly depends on initial fiber alignment, as well as long term movement (beam drifts) and higher-frequency tip-tilt motions (Bechter et al., 2016). These can originate both from residual atmospheric aberrations or from telescope and instrument flexure and vibrations.

We have developed a fiber based focal plane tip-tilt sensor to compensate for the movements and tip-tilt vibrations. The concept was introduced in 2017 (Dietrich et al., 2017) and a modified preliminary design was presented in 2018, as a tip-tilt sensing MLA (Hottinger et al., 2018).¹ The tip-tilt sensor is based upon a fiber bundle consisting of the “science” SMF and six surrounding sensing MMFs. A MLR sits on top of the fiber bundle tip and refracts increasing amounts of light into the corresponding surrounding sensing fibers as the beam gets misaligned. Analysis of the amount of light coupled into these fibers then allows reconstruction of the actual beam position, i.e. the tip-tilt. This device is designed to be retrofitted to any SMF fed spectrograph, but our prototype is specifically designed for the prototype of the iLocater spectrograph (Crepp et al., 2016) at the LBT.

In this work we outline the working principles of the fiber-based tip-tilt sensor and the corresponding application (Sec. 5.2), as well as its performance in lab conditions

¹Despite the difference in name, the working principles presented in this work are identical to the ones in Hottinger et al. (2018). The actual geometry of the lenses has inspired us to rename the 3D printed lens to micro-lens ring (MLR) instead of micro-lens array (MLA), due to design having a central aperture and the overall shape being point symmetric. The fiber arrangement has changed slightly as printing restrictions required the use of MMFs with larger core sizes.

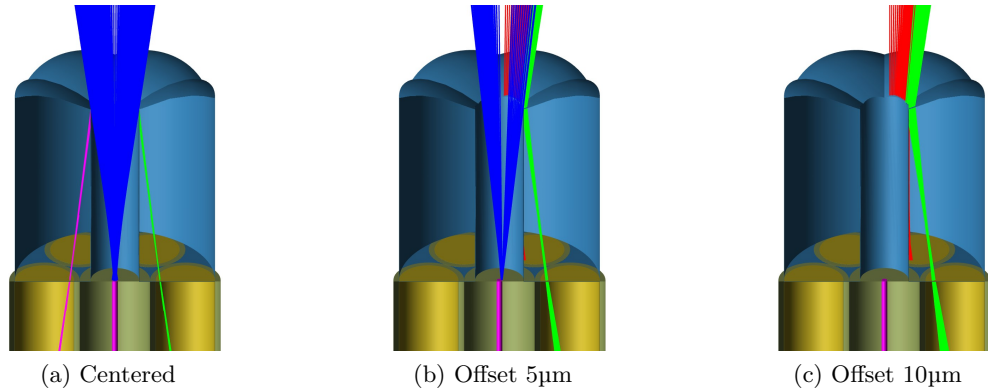


Figure 5.1: Modeled ray propagation through the micro-lens ring (MLR) for an incoming beam that is **(a)** aligned and offset by **(b)** $5\mu\text{m}$ and **(c)** $10\mu\text{m}$, respectively. In the platescale of iLocator frontend (at $1\mu\text{m}$), the diffraction limit $1.22\lambda/D \sim 60\text{mas}$ corresponds to $\sim 3.9\mu\text{m}$ offset. Please note that the number of rays propagating to the tip of the single-mode fiber (SMF) does not correspond to the coupling efficiency.

(Reprinted from Hottinger et al., 2019)

(Sec. 5.3). In Sec. 5.4 we discuss advantages of this sensor before summarizing and highlighting future work in Sec. 5.5.

5.2 Design

5.2.1 Optical principle

At the focal plane of the telescope, the tip-tilt sensor is formed of a fiber bundle, which consists of one central SMF (Fibercore SM980, $1/e^2$ MFD= $5.8\mu\text{m}$) and six surrounding MMFs (Thorlabs, core size $105\mu\text{m}$, NA=0.22). The central science fiber guides the light from the telescope to the spectrograph. This fiber is taken from the same production batch as the fiber for iLocator, which allows us to match the MFD and therefore increase throughput. The surrounding MMF are fed to the sensing system. As these fibers do not feed the spectrograph we can make use of the larger core diameter MMFs, to allow for better coupling through reduced alignment tolerances. A small fraction of the light is coupled into these fibers even when the PSF is on axis to allow for correction feedback. This principle is illustrated in Fig. 5.1 for an aligned beam (a) that achieves maximum coupling efficiency into the science fiber while only a low amount of light is evenly distributed into the surrounding sensing fibers. When the incoming beam is misaligned by $5\mu\text{m}$ (b) and $10\mu\text{m}$ (c), the amount of light that couples to the sensing fibers located in the direction of the displacement increases.

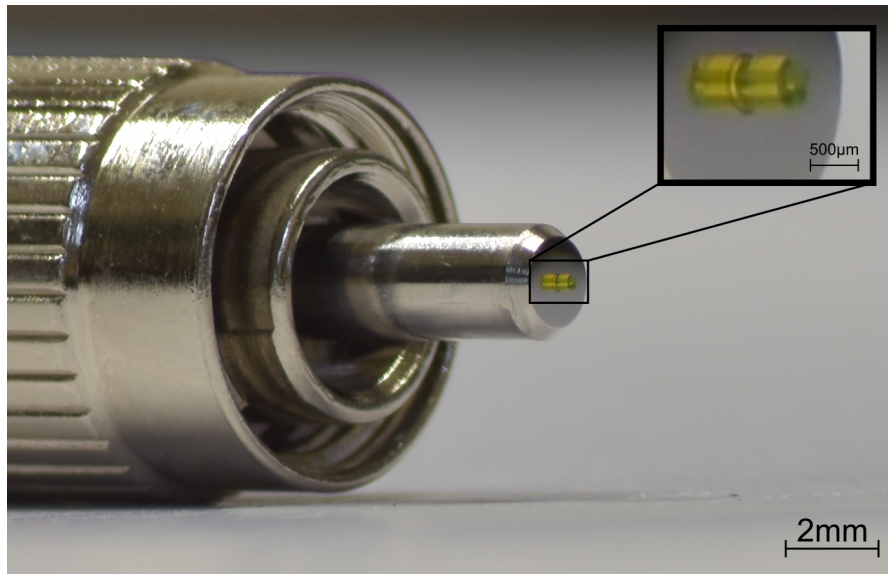


Figure 5.2: DSLR photograph of micro-lens ring (MLR). The lens stands around 380 μm tall and around 400 μm in diameter.
 (Reprinted from Hottinger et al., 2019)

5.2.2 Manufacturing

As the design for our MLR is unusual, this would be excessively expensive to design and produce using conventional methods. To make our sensor economically viable we use an in-situ printing technique developed for the telecommunications industry and recently tested for astronomical applications (Dietrich et al., 2017, 2018). This technique uses 3D-lithography by two-photon polymerization of a commercial IP-resist from *nanoscribe* and allows us to print directly on the tip of the fiber. Printing on the tip of the fiber allows very precise alignment of the lenses to the cores, as the position of the individual cores is measured before printing and the printing position adjusted to compensate for any differences between design and manufactured bundle.

Fig. 5.2 shows the completed MLR on top of a FC/PC connector ferrule. The lens stands approximately 380 μm tall and has a diameter of approximately 400 μm . The central aperture has a diameter of approximately 80 μm leaving the light path to the science fiber unaffected. Using an aperture instead of a lens means reflections and surface quality do not play a role in the SMF coupling and the iLocator system does not have to be modified to accommodate the new lens. There is a limited effect due to the edges of this hole vignetting the beam, which results in a slight chromatic coupling efficiency difference.

5 Laboratory characterization and integration

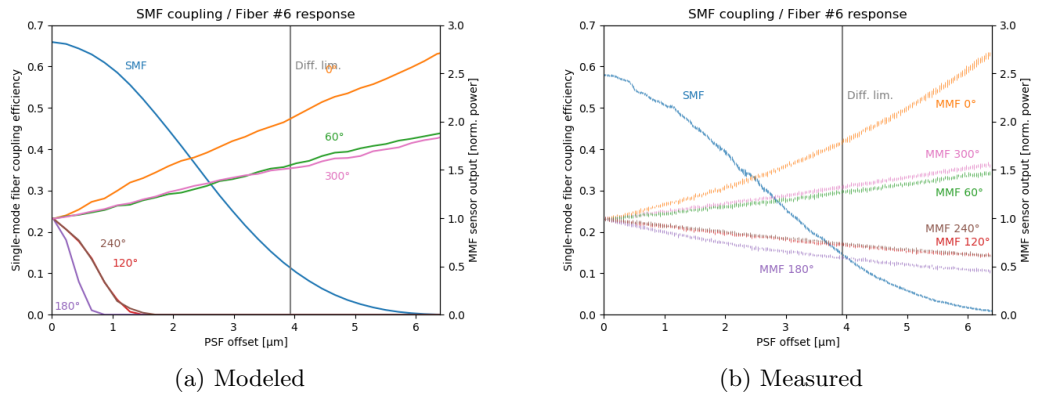


Figure 5.3: Fiber response in respect to centroid position for both modeled throughput in the ray tracing software *Zemax* (a) and for measured throughput at the iLocator fronted prototype in the lab (b). The vertical gray line denotes the diffraction limit at $\lambda \approx 1\mu\text{m}$. SMF coupling (light blue markers, left y-axis) MMFs coupling (right y-axis) for all six sensing fibers, from same direction as the misalignment (orange marker, corresponding to very right fiber with green rays in Fig. 5.1), the two adjacent fibers (green, pink, corresponding to second fiber from right with red rays on Fig. 5.1), to the three fibers on the opposite direction (brown, red, violet, corresponding to two left fibers with pink rays on Fig. 5.1). All MMFs have differing throughputs, which are normalized in this graph for illustration. (Reprinted from Hottinger et al., 2019)

5.2.3 Correction

The six surrounding MMFs are separated from the SMF using a 3D printed fiber breakout and rearranged to form a linear array, which is then re-imaged onto a InGaAs camera (First Light C-Red 2). The fluxes of the individual fibers are read, and processed by Durham Adaptive Optics Real-Time Controller (DARC) (Basden et al., 2010; Basden and Myers, 2012), running on a computer equipped with a consumer grade CPU (i5-8400). DARC then reconstructs the actual centroid position from the six fluxes using a sine-fit approach with some calibration correction. The loop is then closed by an integration correction, feeding a signal to a tip-tilt mirror upstream.

5.3 Results

Setup and optimization of the fiber-based tip-tilt sensor and the corresponding control system were carried out at the KOOL (Hottinger et al., 2018), in Heidelberg, Germany. Initial integration tests were conducted at the iLocator frontend prototype at the Uni-

versity of Notre-Dame in Indiana, USA.

Fig. 5.3 shows the response for the seven individual fibers depending on the centroid position for both modeled throughput in the ray tracing software *Zemax* (a) and for measured throughput at the iLocator fronted prototype in the lab (b). As the incoming beam is de-centered, the SMF coupling (light blue markers, left y -axis) decreases significantly within a few μm . On the right y -axis, the response on the sensing fibers is plotted. The amount of coupled light increases for the MMF corresponding to the direction of the offset (orange marker, corresponding to very right fiber with green rays in Fig. 5.1) as well as the two adjacent fibers (green, pink, corresponding to second fiber from right with red rays on Fig. 5.1). The throughput of the MMFs opposite to the misalignment decreases (brown, red, violet, corresponding to two left fibers with pink rays on Fig. 5.1). All MMFs have differing throughputs which are normalized in this graph for illustration. The actual difference originates in residual aberrations in the PSF of the optical setup, in the reconstruction algorithm this is accounted for by a calibration correction.

The overall flux in the six sensing fibers amounts to 2.3% of the overall incoming flux in the lab measurements compared to 10% expected from modeling, which is still being investigated. The SMF coupling efficiency is designed to amount to 67% of the overall incoming light which is less than the $\sim 80\%$ that is theoretically possible when coupling an Airy pattern into a SMF (Shaklan and Roddier, 1988). The measured maximum coupling efficiency is 58% somewhat lower than the expected performance from modeling. This $\sim 10\%$ percentage points difference corresponds to the 70% coupling efficiency into a regular bare SMF that was achieved on the same setup which is also ~ 10 percentage points below the achievable maximum coupling efficiency. We therefore account that difference to residual aberrations in the beam and likely induced in the optics used in generating a simulated telescope beam in laboratory testing.

While most of the modeled and designed characteristics are achieved, these discrepancies in coupling efficiency remain and still need to be fully understood. Furthermore, as seen in Fig. 5.3b, the response is not as linear as expected. This calls for a more complicated reconstruction algorithm. A simple fitting approach with a sine function was able to recover the measured PSD quite accurately. This is shown in Fig. 5.4 for reconstruction (orange) of an artificially introduced vibration (blue). Further calibration correction is being developed to increase accuracy.

5.4 Discussion

The setup of the correction system and laboratory results show that the fiber based tip-tilt sensor is capable of sensing aberrations. Yet, both coupling efficiency of the SMF at 58% is less than expected (67%) and coupling into the sensing MMFs yields considerably less light than modeled (2.3% compared to 10%). The response also shows a deviation from the predicted linear response, requiring higher order reconstruction algorithms.

When introducing higher order aberrations, the sensor response also shows very characteristic signals. This can already be used to identify signatures of individual modes and will be further improved to yield NCP wavefront data.

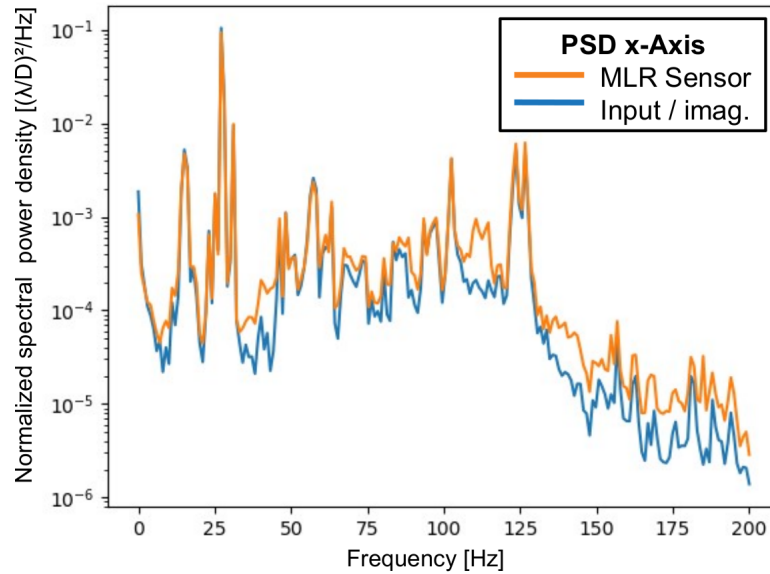


Figure 5.4: Power spectral density (PSD) of the position in x-direction of introduced vibrations as seen on a separate detector that images the PSF (blue) and recovered by the fiber based tip-tilt sensor presented in this work (orange). (Reprinted from *Hottinger et al., 2019*)

Compared to conventional beam stabilization strategies the fiber based tip-tilt sensor presented in this work yields several advantages. While most techniques direct light off to a separate detector such as a quad-cell (Esposito et al., 1997), the fiber based tip-tilt provides an excellent point of measurement shortly before the focal plane feeding the science fiber. This ensures that there are no NCP aberrations between the science fiber and the sensor, allowing the observer to optimally couple light from the telescope. Furthermore it is very compact and can easily be integrated into any (existing) instrument, only requiring the space for the fiber itself while the read out optics and electronics can be placed in a remote location. This can reduce complexity and cost for different applications. Further research will therefore go into implementing this sensor in small, compact systems and telescopes. Other advantages are the very predictable vignetting of the light within the system and a wide dynamical range as light is coupled into the sensing fibers even for rather large offsets making it also suitable for coarse (initial) alignment processes.

5.5 Conclusion

In this work we present a fiber based tip-tilt sensor that has been designed to improve SMF coupling at the iLocator front end and presented initial laboratory results. Our novel sensor shows a very distinctive response to a misaligned incoming beam. Yet,

the coupling efficiencies on both the central science SMF and the surrounding sensing MMFs are lower than expected. Furthermore, an unexpected non-linearity calls for a more complicated reconstruction algorithm.

The sensor is made possible by new exciting technologies such as the two-photon polymerization used for manufacturing the MLR for this device. Only little light is used for sensing if the beam is aligned and only when the beam becomes misaligned more light is refracted into the sensing fibers. Its advantages are its compact design and sensing at the fiber coupling focal plane, which are not possible with traditional systems, and the potential to sense higher order aberrations. We plan to test it with realistic on-sky conditions at the iLocator front-end at Large Binocular Telescope in the near future. Coupled to a suitable AO system, this could be an important tool for coupling SMFs to ELT class telescopes.

Acknowledgments

This work was supported by the Deutsche Forschungsgemeinschaft (DFG) through project 326946494, ‘Novel Astronomical Instrumentation through photonic Reformatting’.

This publication makes use of data generated at the Königstuhl Observatory Optomechanics Laboratory (short: KOOL) which is run at the Max-Planck-Institute for Astronomy (MPIA, PI Jörg-Uwe Pott, jpott@mpia.de) in Heidelberg, Germany. KOOL is a joint project of the MPIA, the Landessternwarte Königstuhl (LSW, Univ. Heidelberg, Co-I Philipp Hottinger), and the Institute for System Dynamics (ISYS, Univ. Stuttgart, Co-I Martin Glück). KOOL is partly supported by the German Federal Ministry of Education and Research (BMBF) via individual project grants.

6 On-sky results

The following chapter is a reprint from the 2021 peer-reviewed publication by Hottinger et al. in JOSA B, titled *On-sky results for the integrated micro-lens ring tip-tilt sensor*. It was published as an article in the feature issue ‘Astrophotonics’ which brought together a number of new publications in applied photonics in the field of astronomy. It is the summary of the on-sky tests that were performed with the MLR-TT sensor in 2019.

Contribution

There are a number of people involved in this project and it is important to acknowledge the important contributions that each of them has provided to its success and correspondingly to the publication of this article. All authors have contributed significantly to the project and have played an appropriate role in publishing the paper both in action and in writing; see *acknowledgments* for an overview of the different contributions.

I, the author of this thesis, have been the leader of the project. I have been responsible for the design of the sensor itself, but also for the system as a whole as has been described throughout this work. This includes all parts of optical designs of the MLR, the read-out optics, and the laboratory modifications, it includes the mechanical design of the setup and the electronic design of the read-out and computational component. I have performed all laboratory tests and performed the integration test at the University of Notre Dame, IN. I have set up the system at Large Binocular Telescope (LBT) and performed on-sky measurements with the MLR-TT sensor and have subsequently done data processing and analysis. I have also been responsible for most of the segments of the text itself.

Summary and context

This publication presents the results of on-sky experiments with the MLR-TT sensor. This marks the first high point of the development of the sensor system and its integration with the iLocator acquisition camera going back to the beginning of concept development in 2016 (Dietrich et al., 2017). The paper not only presents the results of the experiments but also gives a general overview of the system including the optical design, the electrical communication, and the software employed with the control algorithms.

The most important data is the recorded performance of the sensor during nighttime observations on stellar targets together with the corresponding reference measurements by the Andor focal plane camera. Furthermore, laboratory measurements that were performed afterward to characterize the lenses were included. To replicate the sensor’s on-sky behavior, AO simulations were performed with the HCiPY package (Por et al.,

6 *On-sky results*

2018). This includes both synthetic atmospheric modeling as well as simulated wavefront correcting coupling into an approximated MLR-TT sensor.

In this publication, it is shown that the sensor is generally able to reconstruct the centroid, i.e. tip and tilt disturbance, but it also shows that the sensor's measurements significantly deviate from the reference measurements performed by the focal plane camera. This is further supported by the observation that the closed-loop control using the sensor is not able to efficiently correct this disturbance. This discrepancy is shown to be most prominent in the lower frequencies where lower-order Zernike modes dominate the residual aberrations of the incoming wavefront.

That behavior is shown to have a significant trend with respect to the measured SR, showing an improvement in tip-tilt recovery with decreasing residual aberrations. Using the synthetic setup to replicate the on-sky observation, this trend is also visible, supporting this interpretation.

JOSA B, 2021: On-sky results for the novel integrated micro-lens ring tip-tilt sensor

(Reprinted with adapted formatting)

P. Hottinger, R. J. Harris, J. Crass, P.-I. Dietrich, M. Blaicher, A. Bechter, B. Sands, T. Morris, A. G. Basden, N. A. Bharmal, J. Heidt, T. Anagnos, P. L. Neureuther, M. Glück, J. Power, J.-U. Pott, C. Koos, O. Sawodny, and A. Quirrenbach. On-sky results for the integrated microlens ring tip-tilt sensor. *JOSA B*, 38(9):2517–2527, Sept. 2021. ISSN 1520-8540. doi: 10.1364/JOSAB.421459

Abstract

We present the first on-sky results of the micro-lens ring tip-tilt (MLR-TT) sensor. This sensor utilizes a 3D printed micro-lens ring feeding six multi-mode fibers to sense misaligned light, allowing centroid reconstruction. A tip-tilt mirror allows the beam to be corrected, increasing the amount of light coupled into a centrally positioned single-mode (science) fiber. The sensor was tested with the iLocator acquisition camera at the Large Binocular Telescope in November 2019. The limit on the maximum achieved root mean square reconstruction accuracy was found to be $0.19 \lambda/D$ in both tip and tilt, of which approximately 50% of the power originates at frequencies below 10 Hz. We show the reconstruction accuracy is highly dependent on the estimated Strehl ratio and simulations support the assumption that residual adaptive optics aberrations are the main limit to the reconstruction accuracy. We conclude that this sensor is ideally suited to remove post-adaptive optics non-common path tip tilt residuals. We discuss the next steps for the concept development, including optimizations of the lens and fiber, tuning of the correction algorithm and selection of optimal science cases.

6.1 Introduction

In recent decades, improvements in the performance of an increasing number of ExAO systems has led to the ability to image near the diffraction-limit using 8 m-class telescopes (Beuzit et al., 2008; Esposito et al., 2011; Macintosh et al., 2014; Jovanovic et al., 2015). These ExAO systems focus on achieving the best performance over a small FoV and regularly achieve SRs of 80% in the NIR. One of the most prominent goals for these systems is the direct observation and characterization of exoplanets (Angel, 1994), for which high angular resolution and contrast are crucial. The high level of correction provided by these ExAO systems also makes it possible to efficiently couple light from the telescope directly into SMFs (Bechter et al., 2016). SMFs have a core diameter of the order of ten microns, which can only transport the fundamental fiber mode. As this mode is the only spatial mode transported and has a near-Gaussian intensity profile, the corresponding output beam is very stable and easy to model. SMFs also act as a spatial filter and couple very little sky background (Crepp et al., 2016). This makes them highly suitable for direct exoplanet spectroscopy (Haffert et al., 2020) and interferometry

(Coudé du Foresto, 1994; Le Bouquin et al., 2011; Gillessen et al., 2010; Cvetojevic et al., 2018; Martinod et al., 2018). When coupled to a high resolution spectrograph, SMFs also remove conventional modal noise, allowing an increase in the achievable radial velocity (RV) precision (Cvetojevic et al., 2017). A number of SMF-fed spectrographs are currently under development, including iLocater at LBT (Crepp et al., 2016; Crass et al., 2020), SPHERE and CRIRES+ at the Very Large Telescope (VLT) (Vigan et al., 2018), RHEA and IRD at SCExAO/Subaru (Feger et al., 2014; Kotani et al., 2018) and KPIC at Keck (Mawet et al., 2016).

As the size of the fiber is of the order of the diffraction limit (λ/D , where λ is the wavelength and D the diameter of the telescope), the alignment accuracy is highly dependent on the PSF stability (see Fig. 6.1 for an example of relative coupling efficiency as a function of residual tip-tilt position). Any vibrations that occur throughout the telescope system and influence the position of the PSF in the focal plane can have a large impact on performance. These variations can be caused by electrical and mechanical components such as fans and pumps, but can also be induced by wind, atmospheric distortions and dome seeing (Milli et al., 2018). As these variations can have both large amplitude and high frequencies, the AO system may not be able to compensate for them sufficiently and, if they can occur outside the path to the WFS, they will not be sensed. These variations can effect the performance significantly (Lozi et al., 2018b) and turn out to be a limiting factor when coupling into SMFs, with coupling efficiency being degraded by as much as a factor of two (Bechter et al., 2019).

Besides high-order AO correction, efficient SMF-coupling therefore requires a method to accurately sense and correct induced tip-tilt variations. Traditionally, this is accomplished by detecting the PSF at the focal plane either with a fast quad-cell photo detector (Esposito et al., 1997) or camera, computing the centroid position, and feeding back a corresponding error signal to a fast tip-tilt correction mirror. More advanced systems include feed-forward correction of mechanical vibration measurements with accelerometers (Glück et al., 2017) and the deployment of complex metrology systems utilizing concurrent alignment lasers (Lippa et al., 2016). While most of these systems have been adopted at large telescopes, they all have a significant mechanical and optical footprint, throughput loss, tend to become complex in operation, and are vulnerable to NCP effects as the tip-tilt correction is performed at a different optical surface than the SMF face.

Different fiber based photonic sensor concepts are being investigated in the community to complement conventional AO systems (Corrigan et al., 2016; Norris et al., 2020c). The concept presented in this work draws from Dietrich et al. (2017), who developed a sensor with multiple SM cores equipped with an micro-lens array to refract the beam at the focal plane for both science instrument and tip-tilt sensing. Our modified concept features MMFs in conjunction with a MLR (Hottinger et al., 2018) for sensing and is called the micro-lens ring tip-tilt (MLR-TT) sensor (Hottinger et al., 2019). We present first on-sky results of this novel tip-tilt sensor with the iLocater acquisition camera at the LBT (Crass et al., 2020).

In Section 6.2, we describe the sensor concept and the methods used to design, manufacture and employ it at the telescope along with outlining our simulation approach. In Section 6.3 we present our on-sky results and supporting simulations and in Section

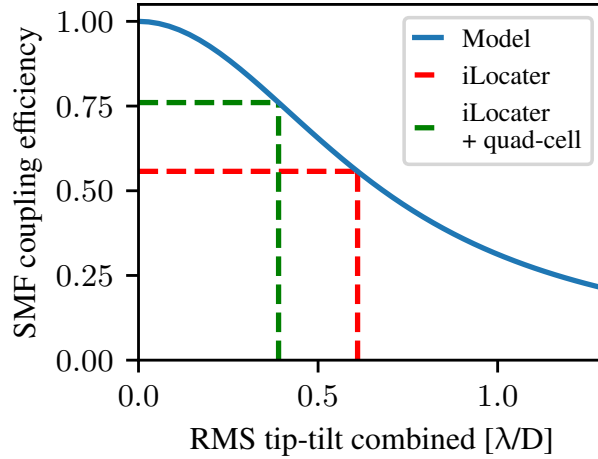


Figure 6.1: Numerically calculated theoretical normalized coupling efficiency assuming an optimally coupled diffraction-limited PSF with additional residual tip-tilt variation, plotted in units of λ/D . The measured RMS residuals at the iLocator focal plane are also indicated, without beam stabilization at $0.61 \lambda/D$ resulting in a theoretical reduction by 44% (red line), and with additional stabilization with a quad-cell detector improving tip-tilt stability to $0.39 \lambda/D$, leading to a tip-tilt induced coupling loss of 24% (green line) (Crass et al., 2020).

(Reprinted from Hottinger et al., 2021)

6.4 we discuss these results and future developments before presenting our conclusions in Section 6.5.

6.2 Design and methods

The MLR-TT sensor concept is depicted in Fig. 6.2 as both a schematic cross-section of the optics (Fig. 6.2, left-hand side) and as images of the manufactured components (Fig. 6.2, right-hand side). The details are re-iterated here, with additional information, for clarity:

1. The sensor consists of a fiber bundle containing six MMFs surrounding a SMF, located at the iLocator focal plane. On the fiber face, a MLR stands $380 \mu\text{m}$ tall and $355 \mu\text{m}$ wide with a central aperture of $86 \mu\text{m}$.
2. The central part of the beam is injected into the SMF, while the outer edge is clipped and refracted by the MLR. Depending on the alignment of the beam, the proportion of light clipped by the MLR changes, which modifies the coupling into the individual MMFs.

6 On-sky results

3. The MMFs are separated from the SMF, re-arranged to form a linear array, re-imaged, and read out by a detector.
4. The illumination pattern of the MMFs is processed to reconstruct the original PSF centroid position, which can be fed back to a fast steering tip-tilt mirror for correction.

6.2.1 Fiber bundle design

The fiber bundle was manufactured commercially (Berlin Fibre GmbH) and holds the array of seven fibers terminated into an FC/PC connector which is then connected to the iLocator fiber feed mount. The fibers are stripped of their furcation tubing and buffer and are placed in the connector with a pitch of 125 μm . After 30 cm, the SMF and the MMFs separate into two individual 5 m-long fiber cables: 1) the science SMF, which is terminated to an FC/PC adapter to feed the science instrument and 2) the sensing MMFs, which are rearranged into a linear array within an SMA connector.

The SMF (Fibercore SM980) features a MFD of 5.8 μm ($1/e^2$ -intensity at 980 nm) and is taken from the same batch of the fiber that will feed the iLocator spectrograph, minimizing any fiber-to-fiber coupling losses further down the fiber link. To simplify design and production, the MMFs are off-the-shelf fibers (Thorlabs FG105LCA). Their optical properties (core diameter 105 μm , NA=0.22) were chosen in order to reduce the core-to-core separation between the SMF and MMFs, reducing the 3D printed lens dimensions.

6.2.2 Lens design

Design and optimization of the MLR were performed using the optical design software *Zemax OpticStudio*. To calculate the coupling efficiency into the SMF, the *Physical Optics Propagation* (POP) tool was employed, and for MMF coupling the *Imaging* tool was used. POP uses Fourier and Fresnel propagation, which is crucial when handling the near-Gaussian mode of the SMF and the complex illumination pattern on the MLR. It is computationally intensive however, so to design the shape of the lenses, the *Imaging* tool was used, which utilizes a ray tracing algorithm to estimate the coupling efficiency into MMFs.

For our technology demonstrator, we aimed to have a strong signal for tip-tilt sensing while also enabling high SMF coupling efficiency. This will both increase the SNR and also provide a signal in all six fibers within a reasonable dynamic range. The diameter of the central aperture was chosen to clip $\sim 13\%$ of the light, reducing the maximum achievable SMF coupling efficiency with an idealized circular pupil from $\sim 80\%$ (Shaklan and Roddier, 1988) to $\sim 65\%$. Using this aperture, the surface shape of the MLR was then optimized to maximize the MMF coupling efficiency, weighted to favor on-axis beams with decreasing priority for misalignment up to 100 μm (corresponding to $\sim 20 \lambda/D$). The surface shape of the individual lenses needs to provide suitable optical power to focus the incoming clipped part of the beam into the MMF. This was achieved by optimizing the

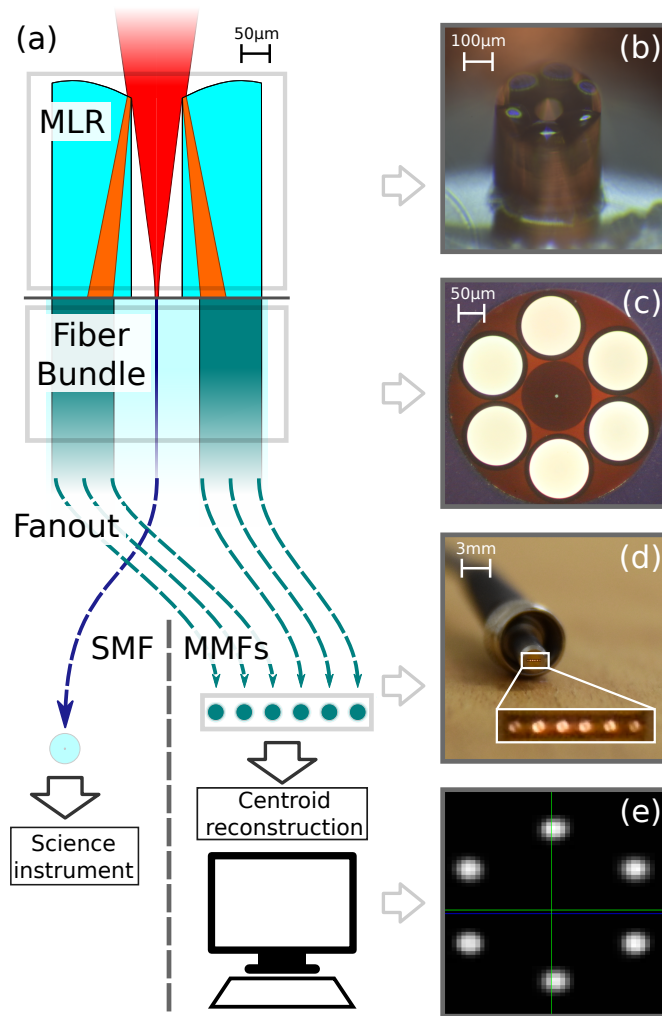


Figure 6.2: Overview of the micro-lens ring tip-tilt sensor (MLR-TT). (a) Schematics of the setup. The starlight (red) is coupled into the SMF (dark blue), while some light at the edges of the beam is clipped and refracted (orange beam) by the MLR (light blue) to be coupled into the sensing MMFs (dark green). The fibers are embedded in a fiber bundle that fans out into a single SMF which then feeds the starlight into a science instrument and the six MMFs that are reformatted into a linear array mounted in an SMA connector. The sensing fibers are then re-imaged and the detected flux is used to reconstruct the centroid position of the telescope beam. (b) Microscope image of the MLR on the fiber bundle face, (c) microscope image of back-illuminated fiber bundle, (d) sensing fiber output at the fiber connector, and (e) re-arranged detector signal for visual examination of the reconstruction algorithm with the green cross indicating the centroid position.

(Reprinted from Hottinger et al., 2021)

spherical shape and then adding corrections with both Zernike focal sag and separate conical constants in both directions. A strong optical power was necessary to refract the beam from the inner edge of the microlens to the MMF. For this, polynomial corrections were successively applied up to fourth order in the axis parallel to the radial axis, no additional correction was applied in the angular direction.

6.2.3 Lens manufacturing

The MLR was manufactured using two-photon polymerization using a proprietary resin on the fiber tip (Dietrich et al., 2018), which allows the manufacturing of free-form lenses on small scales. Due to the use of stages in the printing process, these structures can take arbitrary shapes, limited by the need for an appropriate support structure and macroscopic forces. The printing is aided by back-illuminating the fiber bundle and yields sub-micron alignment precision (Dietrich et al., 2017) compensating for irregularities in the bundle geometry. The process allows a precision of ~ 100 nm and a RMS surface roughness of ~ 10 nm. The physical size was limited to the maximum build height of approximately $400 \mu\text{m}$, due to the manufacturing stages and microscope objective NA.

Once the MLR was printed on the fiber the FC/PC connector was then placed within a bulkhead adapter (Thorlabs HAFC) for mechanical protection.

6.2.4 Laboratory sensor response

As the custom lenses belonging to the iLocator acquisition camera were unavailable for laboratory experiments, the MLR-TT sensor's response was tested using commercial lenses. A SMF illuminated by a 1050 nm SLED source (Thorlabs S5FC1050P), was apertured and a Thorlabs AC127-025-C lens was used to produce an NA of 0.14, simulating the telescope's Airy disc. The experimental system provided a lower throughput than the final on-sky experiment, due to lower image quality. The results in Fig. 6.3 show the sensor's response to an gradually off-centered beam in the laboratory setup, both as modeled and as measured. The modeled SMF coupling efficiency (Fig. 6.3, top) includes Fresnel reflection loss of 3.5% at both fiber input and output face. The maximal achievable coupling efficiency within the MLR-TT sensor's SMF is measured at $59.9 \pm 0.6\%$ which is slightly lower than the expected value of 63.2% at the given wavelength. This coupling efficiency then drops off slightly faster than expected with an off-centered beam but features a slightly increased coupling for misalignment of up to $2.2 \lambda/D$. The causes of this behavior still to be understood but are likely due to fiber bundle and lens imperfections.

The response of the sensing MMFs (Fig. 6.3, center) follows the modeled curves well, though the six sensing MMFs are not evenly illuminated when the beam is centered. During alignment we found that the illumination pattern depends strongly on the fiber alignment angle (pitch and yaw) and could not be completely corrected. This can result from asymmetries in the beam or uneven MMF properties such as irregular spacing or different fiber losses. In practice this is corrected by the calibration routine (Sec. 6.2.6).

Laboratory results show the MLR couples 4.1% of the overall light into the MMFs

when the beam is centered, which is 30% lower than the modeled value of 5.8% (this includes 11% reflections and losses from the fiber and 8% from the lens). Interestingly, this loss remains constant with respect to beam position (Fig. 6.3, bottom) up to a centroid offset of $\sim 3\lambda/D$. We presume that the remaining mismatch is due to a non-optimally shaped lens surface. The ray approximation as described in Sec. 6.2.2 only considers a central top-hat beam but fails to accurately account for the diffractive pattern that illuminates the lenses outside the central beam.

Theoretical throughput calculations and the corresponding photon, sky background and camera noise associated with the described system show that with this reduced sensor signal, a source with 8th magnitude in the J band can provide a SNR of 14 for each MMF output when running at 500 Hz. Simulations with the same pipeline as described in Sec. 6.2.8 show that this results in an reconstruction accuracy of $\sim 0.1\lambda/D$ in tip and tilt combined. In this limiting case, performance is limited by read-out noise of the detector.

6.2.5 Signal processing

The output of the sensing MMFs was re-imaged with two lenses mounted within a hybrid tube and cage mechanical system and directly attached to the lens interface of a First Light C-Red 2 InGaAs detector. This detector was chosen as it provides both a high frame rate (up to 16 kHz) and low read-out noise ($34 e^-$) with a pixel size of $15\ \mu\text{m}$. Each MMF illuminates a circular region on the detector with a diameter of $100\ \mu\text{m}$. For each fiber, the 20 pixels with the highest SNR are selected and used for further processing. In laboratory tests, 20 pixels were measured to provide a steady fraction of 80% of the flux and the best overall SNR. The detector data was then processed by the DARC (Basden et al., 2010; Basden and Myers, 2012), running on a consumer grade desktop computer.

6.2.6 Reconstruction and calibration

The reconstruction algorithm (see Fig. 6.4) calculates the MMF illumination and converts it to a physical centroid position. For this, the six fiber fluxes are ordered with their azimuthal coordinate and a sine function with angular period of 2π is fitted to this signal. Three best fit parameters are obtained by this routine (see Fig. 6.4):

1. Offset, depending on both background signal and target flux.
2. Amplitude, corresponding to the radial position of the beam. Note, this is an arbitrary flux unit and the amplitude does therefore not directly yield the physical centroid position.
3. Phase, corresponding to the azimuthal coordinate of the centroid position.

Laboratory tests showed that this approach yields the most reliable and stable output, less susceptible to noise than a simple center-of-mass (CoM) algorithm.

A calibration routine is used to correct the reconstructed centroid position for accurate loop feedback and run time diagnostics. It accounts for irregularities in the system such as asymmetries or misalignment of the MLR, transmission variations within the fiber

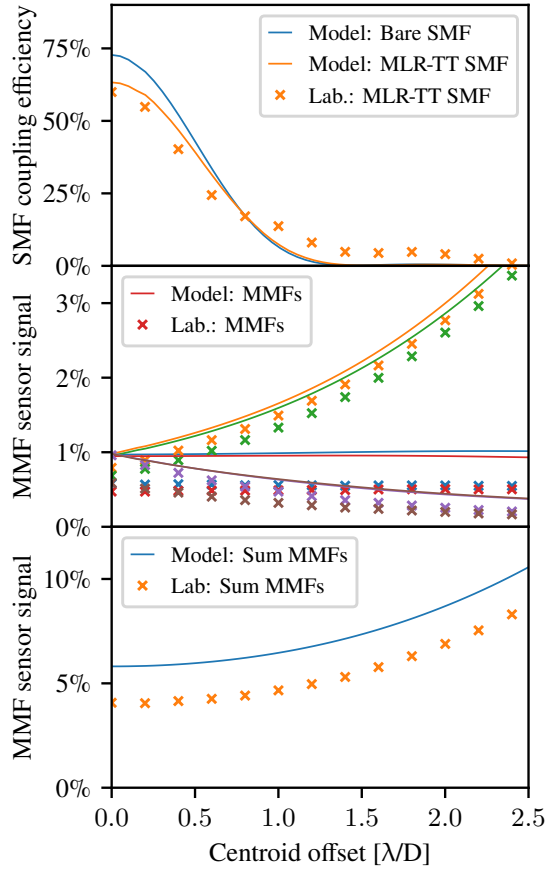


Figure 6.3: Modeled (solid lines) and measured (crosses) sensor response as function of centroid offset. **Top panel:** The coupling efficiency of the science SMF. **Middle panel:** The response of the six sensing MMF as function of beam offset. **Bottom panel:** MLR-TT sensor signal summed over all six MMFs.

bundle and static aberrations in the PSF. For this, a circular motion is introduced with the tip-tilt mirror. The offset between the introduced and reconstructed azimuthal coordinate and the factor between the respective radial coordinates is approximated with individual best fit discrete Fourier transforms (DFTs) of 5th order as a function of the azimuthal coordinate. The obtained correction function is subsequently applied to the measured centroid position. It should be noted that this calibration routine is repeated for each target in order to remove slowly changing quasi-static aberrations (arising from effects such as mechanical flexure) and to include asymmetries of the source itself such as companions or background sources.

The interaction matrix is constructed by applying a linear signal in both tip and tilt with the mirror and simultaneously measuring the centroid position. The resulting

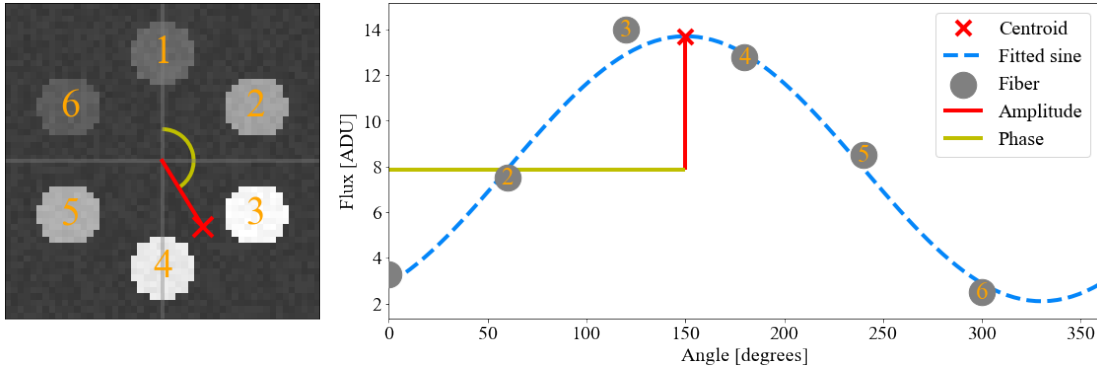


Figure 6.4: Illustration of the reconstruction routine with simulated noise. **Left panel:** Simulated detector image showing the six MMFs (numbered 1-6 in orange) along with the reconstructed centroid of the PSF (red cross). **Right panel:** A graphical illustration of the reconstruction routine. Here the six fiber fluxes (gray, numbered 1-6 in orange) are ordered by their azimuthal coordinate and a sine function with angular period of 2π is fitted, giving the angle, amplitude and offset of the centroid.

(Reprinted from Hottinger et al., 2021)

2x2 matrix is then inverted to obtain a reconstruction matrix, which can be used by the control loop to convert the measured centroid position into an feedback signal to command the tip-tilt mirror.

6.2.7 On-sky integration

The MLR-TT sensor was integrated into the iLocator SX acquisition camera (Crass et al., 2020) that is fed by the Large Binocular Telescope Interferometer (LBTI). The optical path is illustrated in Fig. 6.5. The iLocator acquisition camera receives the pupil from the telescope (a), passes the wavelengths between 920 nm and 950 nm (c) to its imaging channel equipped with an Andor focal plane camera (ANDOR Zyla 4.2 Plus, d), providing a sampling of 6.1 pixels across the full width at half maximum (FWHM) of the diffraction-limited PSF. This focal plane image is used as reference for the centroid position, i.e. the tip-tilt.

iLocator’s native tip-tilt correction features a quad-cell photo detector (Hamamatsu G6849-01 InGaAs, g), which is fed with light picked off by a dichroic at 1.34-1.76 μm , (e) just before the final coupling optics. The quad-cell system can then feed an error signal back to a fast tip-tilt mirror (nPoint RXY3-276, b) to correct for tip-tilt. Alternatively, the mirror can be controlled by the MLR-TT sensor to either introduce the required motions for calibration (see Sec. 6.2.6) or for correcting tip-tilt directly.

The science beam (0.97 – 1.31 μm) is focused by two custom triplet lenses (Crass et al., 2020) to an f/3.7 beam on the SMF to match its MFD of 5.8 μm ($1/e^2$ -intensity at 970 nm). The fiber mount can be moved in 5 axes for alignment and to switch between

6 On-sky results

three independent fibers mounted at the instrument focal plane. These are: the native iLocator SMF, a bare MMF (105 μm core diameter) used for flux calibration, and the guest fiber port equipped with the MLR-TT sensor (f).

Fiber throughput is determined by measuring the output flux from each fiber with the bare MMF serving as an incident flux reference. Output flux is measured with a FemtoWatt receiver (Crass et al., 2020). The fiber bundle holding the six sensing MMFs is routed to a separate opto-electric enclosure, housing the read-out optics and electronics.

6.2.8 Simulations of on-sky results

To further investigate the performance of the sensor with our recorded on-sky conditions, we simulated the sensor response for differing AO correction. To do this, an atmospheric wavefront distortion of 1000 modes in combination with a corresponding AO system correcting 500 modes was modeled using the HCIPy high contrast imaging simulation framework (Por et al., 2018). To allow an accurate comparison, the tip and tilt modes of the resulting wavefront are replaced by the centroid positions that were recorded during the on-sky observations.

These simulations are key as they allow us to understand our results and estimate the impact of residual AO aberrations and their dominance with respect to other noise sources.

6.3 Results

We tested the MLR-TT on-sky in November 2019 at the LBT, using the left (SX) mirror of the telescope (Crass et al., 2020). During the run the Large Binocular Telescope Interferometer adaptive optics (LBTI-AO) system was using the SOUL upgrade, which is designed to produce a SR of up to 78% in I-band (Pinna et al., 2016) under optimal conditions. For all observations the AO system was running at 1 kHz closed on 500 modes. Correction for AO NCPA was performed before observations, but otherwise there was no direct interaction between the MLR-TT sensor and LBTI-AO.

We present the results from three on-sky targets, with a total of 8 datasets. All targets were chosen to be bright ($< 6^{\text{th}}$ magnitude), marginalizing detector noise from the MLR-TT sensor. Tab. 6.1 provides an overview of the targets, the AO loop performance, and the associated datasets.

Each dataset includes three simultaneous measurements taken using iLocator and the MLR-TT sensor:

- Andor focal plane frames (Sec. 6.2.7), taken at a frame rate of 250 Hz. A symmetric 2D Gaussian function is fitted to the data in post processing and its calculated centroid used as a reference for PSF position. The SR in Tab. 6.1 was estimated by fitting a Gaussian to the centroid corrected PSF and taking the ratio between the normalized central intensities of this fit and the expected telescope PSF as described in Bechter et al. (2019). Due to the limited SNR of the individual

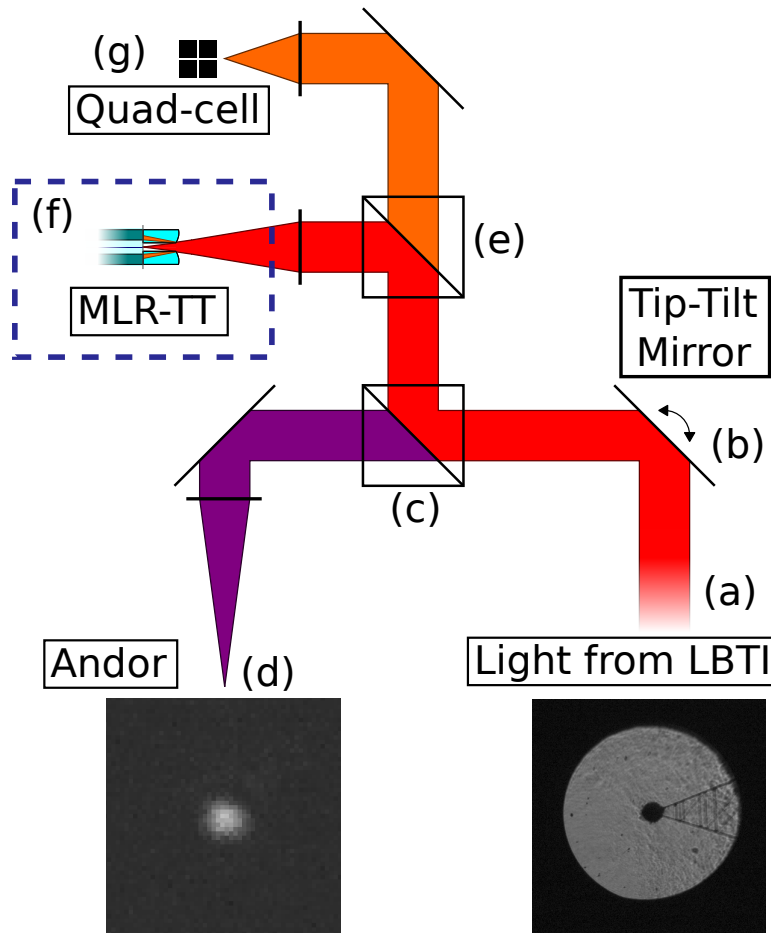


Figure 6.5: Optical path of the experimental setup with the iLocator acquisition camera at LBT (sizes are not to scale). (a) The collimated AO corrected beam from LBTI is steered by a fast tip-tilt mirror (b). A short-pass dichroic (c) transmits wavelengths between 920 and 950 nm to be imaged by the Andor focal plane camera (d). The science light is reflected by the long-pass dichroic mirror (e) and focused into the MLR-TT sensor (f) and SMF. Light between 1.34-1.76 μm is transmitted and imaged on the quad-cell (g) that can be used in closed-loop to correct for tip-tilt vibrations.

(Reprinted from Hottinger et al., 2021)

frames, the SR calculations were smoothed by applying a moving median algorithm covering 20 frames.

- The reconstructed centroid position from the MLR-TT sensor (Sec. 6.2.6). Data were taken at a frame rate of 500 Hz. In post processing the frames were interpolated and cross-correlated to match the time reference of the Andor data.

Table 6.1: Observed targets and datasets as well as observational seeing, estimated SR and the status of the tip-tilt correction loop.

Target/dataset	J-band mag.	Seeing (")	Est. SR	Additional Tip-Tilt control
HIP28634 /4	5.3	1.2-2.0	$50 \pm 6\%$	MLR-TT
	/5 "	"	$52 \pm 7\%$	None
HD12354 /1	5.9	1.0-1.4	$67 \pm 7\%$	None
	/2 "	"	$67 \pm 11\%$	MLR-TT
HIP7981 /2	3.8	1.0-1.4	$66 \pm 4\%$	MLR-TT
	/4 "	"	$65 \pm 4\%$	MLR-TT
	/5 "	"	$65 \pm 4\%$	MLR-TT
	/6 "	"	$65 \pm 4\%$	MLR-TT

- The SMF coupling efficiency was measured with the FemtoWatt receiver (Sec. 6.2.7).

6.3.1 Sensor calibration

As described in Sec. 6.2.6, the calibration pattern was generated by introducing a circular motion on the tip-tilt mirror by issuing open loop position commands. An example of the calibration routine for target HIP7981 is shown in Fig. 6.6 for (a) the Andor reference centroid position, (b) the raw MLR-TT centroid position and (c) the calibrated centroid position.

During the calibration, the AO loop was closed, but no additional tip-tilt correction was applied. Due to residual vibrations at the telescope, the measured centroid positions show a broadened pattern, which is averaged. The averaged centroid positions are used to correct the reconstructed centroid for static asymmetries.

For HIP7981, the reconstruction without calibration shows an RMS error of $0.33 \lambda/D$ in tip and $0.26 \lambda/D$ in tilt ($0.42 \lambda/D$ combined). After correction, this improves to $0.19 \lambda/D$ in tip and $0.21 \lambda/D$ in tilt ($0.28 \lambda/D$ combined) and appears random. The impact of the calibration on the reconstruction accuracy for all targets is listed in Tab. 6.2, including the RMS shift that is applied by the calibration. This shift corresponds to the correction that the calibration routine performs on the centroid position which is seen as an improvement of the reconstructed centroid position. The correction is seen to provide a more significant improvement for the datasets with lower pre-calibration RMS reconstruction error. This arises from a more precise measurement of the calibration pattern (corresponding to a thinner ring in Fig. 6.6) that leads to a more accurate parametrization of the correction function.

For all other datasets listed in Tab. 6.1, the calibration was also applied but did not provide a significant improvement. These datasets all feature a smaller dynamical range and the applied shift varied between 0.06 and $0.09 \lambda/D$ in tip and tilt combined. Compared to the overall noise in these datasets (see Sec. 6.3.4), the impact of the calibration

is negligible.

Table 6.2: Improvement gained through the calibration routine. RMS reconstruction error before and after applying the calibration is listed as well as the RMS shift determined after the application of the calibration routine.

Target	RMS error no calib. [λ/D]	RMS error calibrated [λ/D]	RMS calibration shift [λ/D]
HIP28634 /cal.	0.54	0.50	0.23
HD12354 /cal.	0.42	0.31	0.27
HIP7981 /cal.	0.42	0.28	0.30

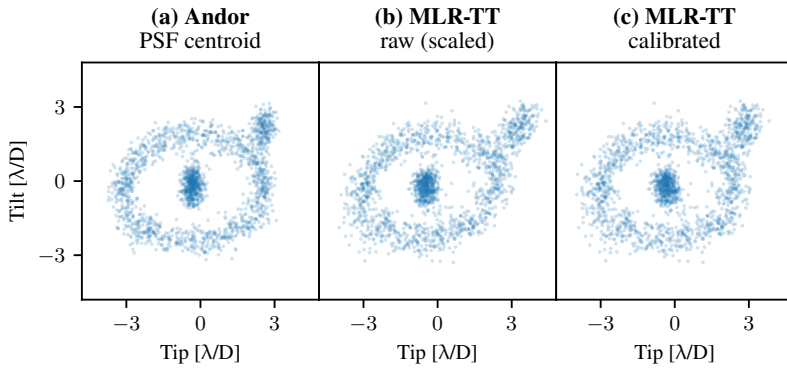


Figure 6.6: Three scatter plots showing the on-sky calibration routine of target HIP7981. Shown are (a) the reference centroid position measured with the Andor focal plane camera, (b) the MLR-TT reconstructed raw centroid position reconstructed from the MLR-TT and (c) the calibrated MLR-TT centroid position (see Tab. 6.2). Initially the PSF is centered, then a circular motion is introduced on the fast tip-tilt mirror. This movement is not calibrated in λ/D and produces an elliptical shape in the focal plane due to the angle of the tip-tilt mirror. The introduced figure also features a central accumulation from before and after the circular motion, as well as an introduced step position seen as a separate patch to the top right of the circle.

(Reprinted from Hottinger et al., 2021)

6.3.2 Closed-loop performance

In the datasets listed in Tab. 6.1, the acquired PSF centroid positions were used to drive the tip-tilt mirror. While the loop was operating stably, no improvement in SMF coupling was observed. The closed loop transfer function as seen by the MLR-TT sensor

(Fig. 6.7, blue/orange) shows a significant rejection of frequencies below 15 Hz, however this is not seen in the Andor reference camera (Fig. 6.7, green/red). Above 15 Hz both Andor and MLR-TT show the same behavior, however the loop fails to correct for the faster disturbances. This suggests that the loop is not running at a high enough frequency for correction or the latency is too high.

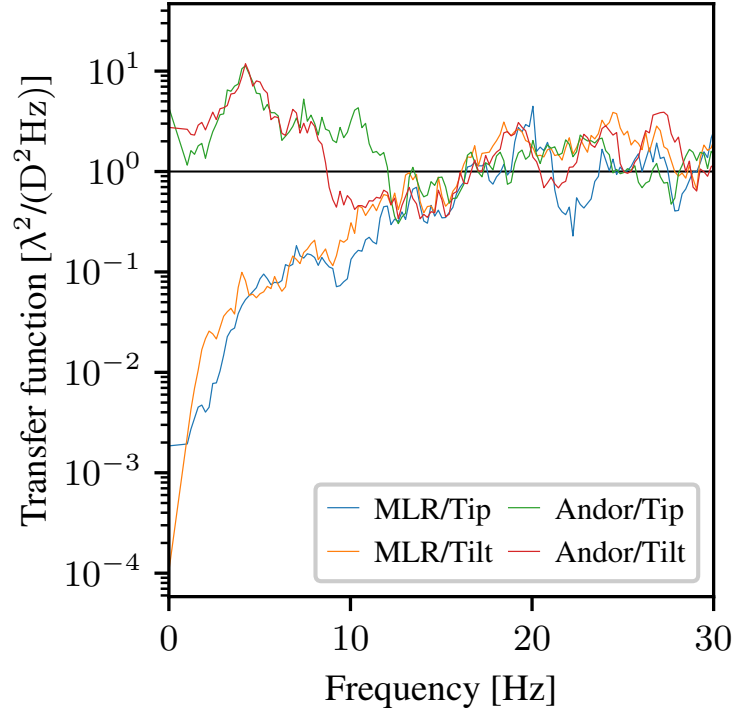


Figure 6.7: Closed loop transfer function when stabilizing the beam with the MLR-TT sensor for datasets HIP28634/4 (closed loop) and HIP28634/5. Below ~ 10 Hz, the MLR-TT sensor (blue, yellow) detects a different frequency rejection than the Andor reference (green, red), whilst above 10 Hz the transfer functions agree well.

(Reprinted from Hottinger et al., 2021)

6.3.3 Reconstruction accuracy

This significant mismatch between MLR-TT sensor and Andor reference in evaluating the loop performance needs to be understood. For this, we analyze the accuracy with which the sensor is able to reconstruct the centroid position. Fig. 6.8 shows the centroid position for the Andor reference and the MLR-TT sensor for HD12354/1, as well as the corresponding reconstruction error. While the scatter of these values does not show any systematic patterns, the time series (cutout, bottom) shows that the sensor is indeed able to track the centroid position. The residual error features a mismatch, amounting

to $0.19 \lambda/D$ RMS in both tip and tilt.

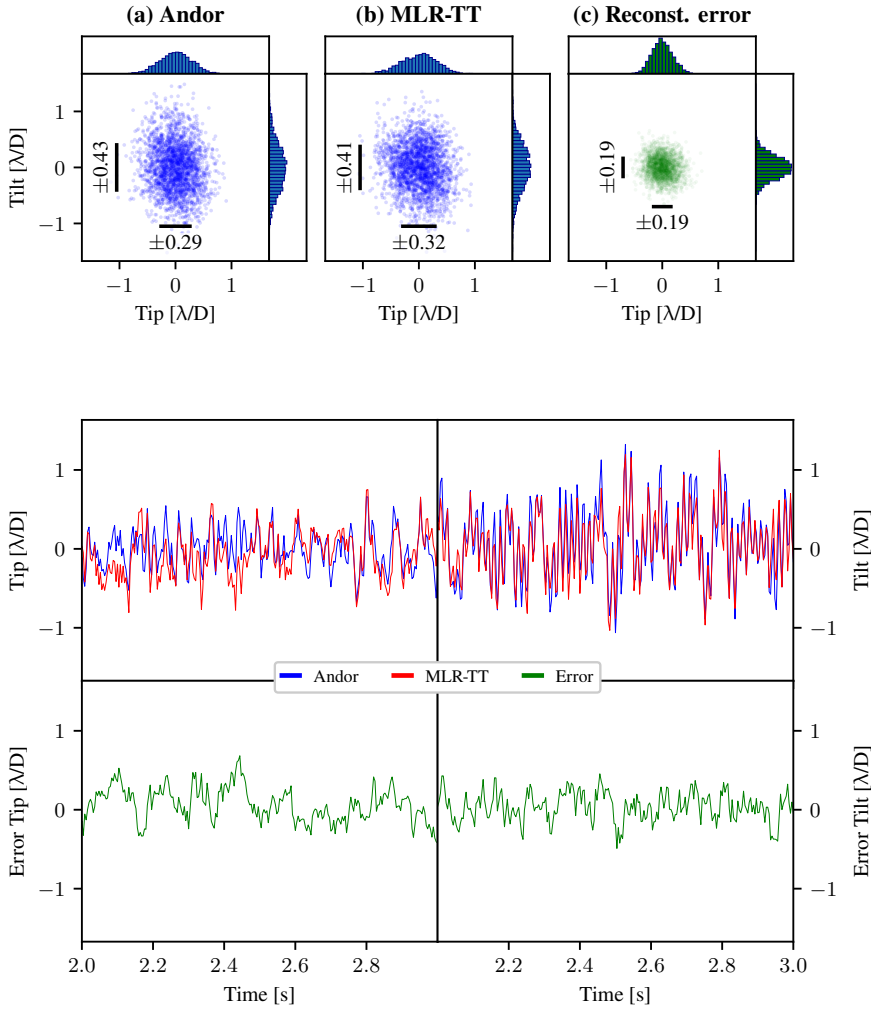


Figure 6.8: Sensor reconstruction accuracy shown graphically. **Top panels:** Time series of (Left) the centroid position measured by the Andor focal plane camera, (Center) the position reconstructed with the MLR-TT and (Right) the error in the reconstruction by taking the difference between the former two datasets. **Bottom panels:** Time series graphs of the same dataset for: (Top) Comparison of the centroid x -position for (tip, left) and y -position (tilt, right) of Andor reference (blue) and MLR-TT (red), and (Bottom) the corresponding reconstruction error (green) from their difference. *(Reprinted from Hottinger et al., 2021)*

The time series of the error suggests a strong low-frequency component. The PSD of the MLR-TT sensor tracks this behavior very well (see Fig. 6.9), with the sensor PSD

6 On-sky results

tracking the features of the reference centroid very accurately above 10 Hz. Residuals below 10 Hz are calculated to account for approximately 50% of the combined tip-tilt error, while residuals between 10 and 20 Hz contribute less than 20%.

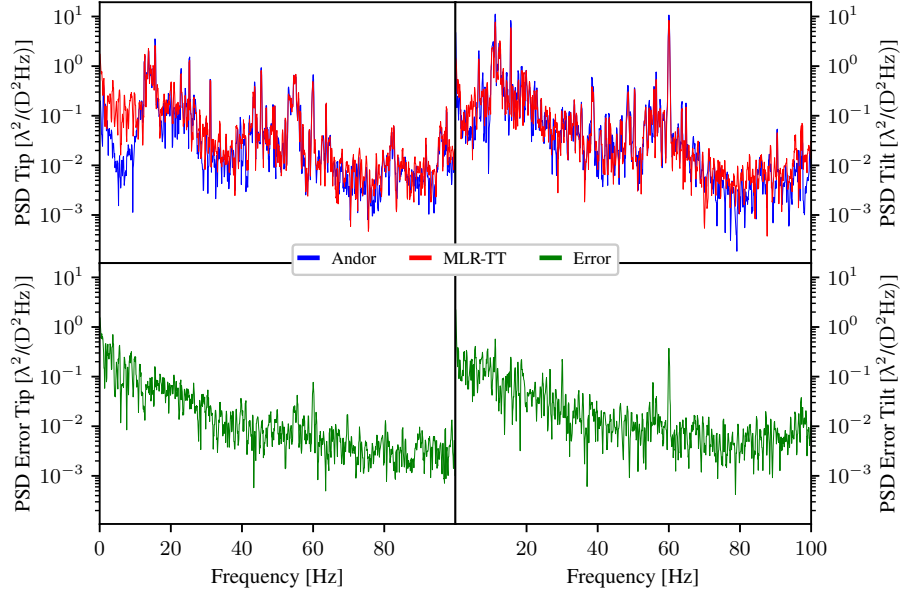


Figure 6.9: Power spectral density (PSD) for HD12354/1 of the signal shown in Fig. 6.8. (Top) PSD of centroid x -position (tip, left) and y -position (tilt, right) of MLR-TT (red) compared to the Andor reference (blue), (Bottom) the PSD of the corresponding reconstruction error (green) for tip and tilt. Most of the vibrational power lies between 10 and 20 Hz, whilst most of the reconstruction error is in the low frequencies (< 10 Hz).

(Reprinted from Hottinger et al., 2021)

6.3.4 Impact of AO performance

Fig. 6.10 shows the combined tip-tilt reconstruction error for all datasets as a function of estimated SR. Note that all datasets feature similar RMS centroid values ($\sim \lambda/D$).

The wavefront correction varies significantly between the datasets and within individual datasets, with subsets featuring SRs as low as 40% and reaching up to 80%. The reconstruction accuracy shows a strong dependency on the SR and improves significantly with increasing SR. The best reconstruction shows a combined tip-tilt RMS of $0.27 \lambda/D$ while the worst reconstruction reaches a RMS error of $0.5 \lambda/D$. A linear fit yields a slope of $-0.95 \pm 0.20 \lambda/D$, an improvement in RMS reconstruction accuracy of $\sim 0.1 \lambda/D$ per 10% increase in SR.

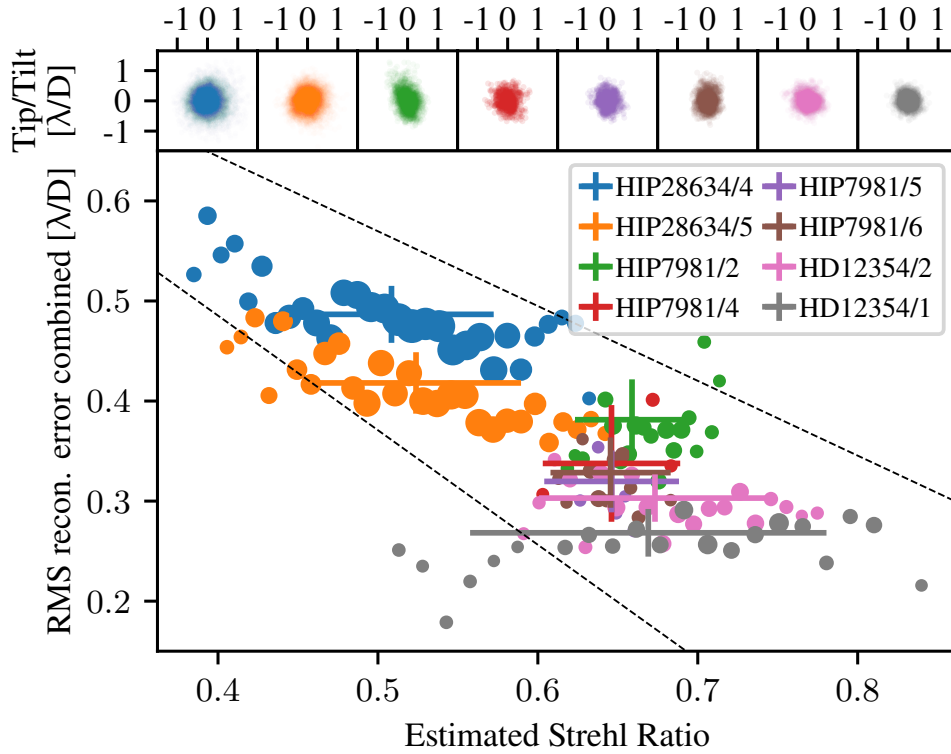


Figure 6.10: On-sky sensor performance. **Main panel:** Reconstruction accuracy as a function of estimated Strehl ratio (SR) for these datasets. Cross marks in the main plot represent the mean and error for each dataset, while the circles in the subplots correspond to subsets with different estimated SRs, with the size of the circle representing the number of frames in each set. The dashed lines show the fitting error. **Top panels:** The centroid reconstruction error scatter plot for each analyzed dataset.

(Reprinted from Hottinger et al., 2021)

6.3.5 On-sky sensor simulations

AO simulations as described in Sec. 6.2.8 were performed to reconstruct the sensor operation. Fig. 6.11 shows the resulting reconstruction error for tip and tilt combined as a function of the retrieved SR and is analogous to Fig. 6.10. For the lowest simulated SRs of $\sim 50\%$, reconstruction accuracy is worse than $0.35 \lambda/D$ and improves to $0.16 \lambda/D$ for a SR of 80% . As with the on-sky results (cf. Fig. 6.10), the data are well fit by a linear trend, with a slope of $-0.72 \pm 0.05 \lambda/D$. For completeness, we have also simulated the reconstruction error for a flat wavefront (Fig. 6.11, yellow marker) which shows a reconstruction error of less than $0.05 \lambda/D$.

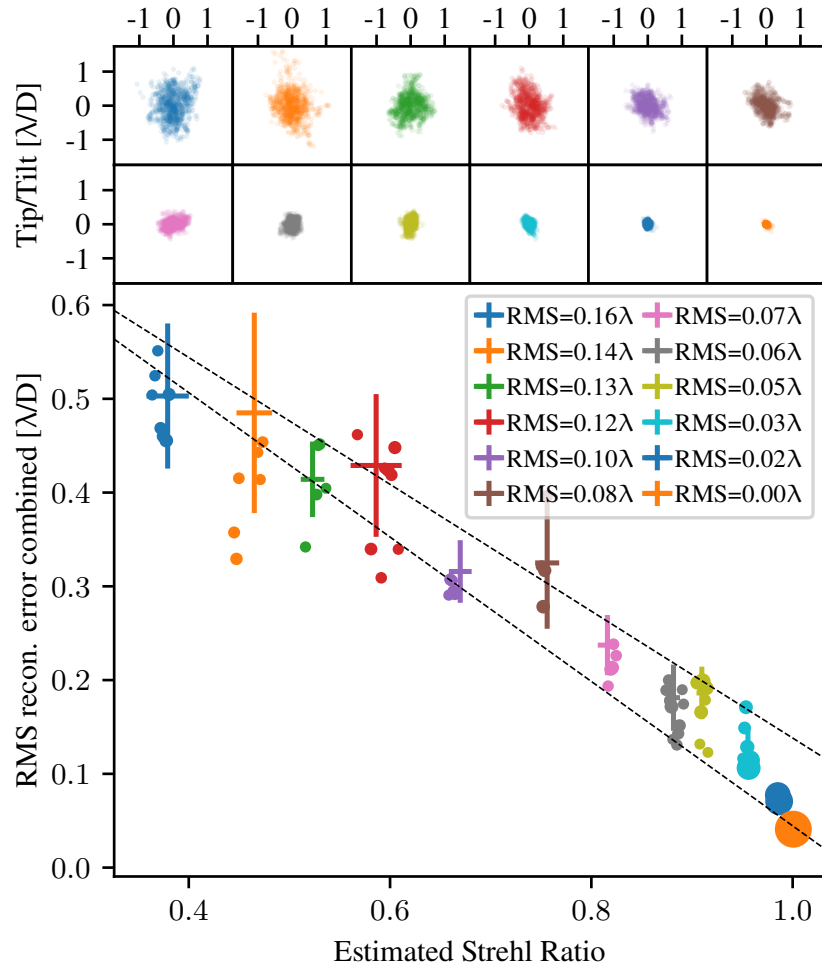


Figure 6.11: Synthetic MLR-TT sensor performance derived from AO simulations, plotted to be comparable to Fig. 6.10. **Main panel:** Reconstruction accuracy as a function of Strehl ratio (SR) for AO simulations with varying residual aberration strength labeled with their RMS wavefront error. Crosses represent overall mean and error for each data set, while the circles correspond to subsets binned by SR, with the size of the circle representing the number of frames in each set. The dashed lines show the fitting error. **Top panels:** Centroid reconstruction error scatter for the individual datasets. *(Reprinted from Hottinger et al., 2021)*

6.4 Discussion

In the preceding section we presented the on-sky performance of the MLR-TT sensor. Whilst able to track incident beam motions, the sensor was unable to improve fiber coupling performance with our current AO loop. The sensor also shows limitations in

the overall performance which can be achieved due to the effects of residual aberrations. The causes and solutions are discussed in this section.

6.4.1 Sensor reconstruction limitations

As shown in Fig. 6.10, the sensor was able to reconstruct the centroid position to an accuracy of $0.27 \lambda/D$ combined tip-tilt RMS. The majority of this error (50%) originates in frequencies below 10 Hz and depends strongly on the estimated SR. To ascertain the cause of this error, we presented optical simulations with differing SR in Sec. 6.3.5. The simulations show the same trend with a slightly flatter linear fit. The discrepancy can be attributed to a number of additional noise sources that occur within the measurements. These alternative sources include detector noise, reconstruction algorithm error, NCP vibrations, flux variations, and noise in the measurements of the reference centroid. While we investigated these factors during analysis, the current system is most strongly impacted by the effects of residual aberrations. For future versions of the sensor we aim to understand the exact contributions that these noise terms have on the reconstruction accuracy.

To further investigate the impact of wavefront aberrations on the MLR-TT sensor, in future laboratory testing and on-sky experiments, we intend to acquire additional metrology data to identify other effects driving performance. This will allow us to optimize the MLR-TT reconstruction algorithm to account for the observed aberrations and possibly even reconstruct Zernike modes beyond tip and tilt.

6.4.2 Loop performance

As illustrated in Fig. 6.10, under the best conditions experienced, the reconstruction accuracy of the sensor provided a combined RMS error of $0.27 \lambda/D$. Assuming an ideal control system, this would provide correction with an RMS error 1.5 times lower than the existing quad-cell system. With our current control system, this is reduced significantly due to latency and meant the loop was only able to reject frequencies up to 15-20 Hz. The control system therefore needs to be optimized in order to allow a better correction of the tip-tilt disturbance which holds the most power in frequencies between 10 and 20 Hz (see Fig. 6.9).

As shown in Fig. 6.9, most of the noise in the reconstruction occurs below 10 Hz. The main goal will be to optimize the MLR-TT sensor software (Sec. 6.4.1) and hardware design (Sec. 6.4.3) to improve its performance in this regime. Even without additional precision, the loop can be tuned to filter this frequency range or another sensor designed to suppress vibrations in the range 1-10 Hz can be added. Alternatively, the MLR-TT sensor may be used to only detect slow beam drift below 1 Hz. Any residual aberrations will average out over long timescales (>1 second) and the sensor can be optimized to measure slow mechanical drift resulting from e.g. gravitational flexures. This would focus the sensor on utilizing one of its main advantage, namely that it is virtually free from NCP effects. When running at lower frame rates, the sensor also needs less light for operation, increasing the limiting sensing magnitude and the light available for the

science instrument.

6.4.3 Sensor optimization

To control the amount of noise that is induced by residual AO aberrations, the lens design can be tuned for future devices. As the shape of the MLR surface is set by the need to efficiently couple light into the MMFs, the height of the lens and the size of the central aperture then become the most important variables. Both parameters control the distance from the focal plane where the telescope beam is sensed and by varying them the impact of aberrations in the system changes.

By sampling the beam closer to the fiber focal plane, the MLR-TT sensor will use an intensity distribution more similar to the PSF for sensing, which depends mostly on the phase of the wavefront at the pupil. As the height of the MLR increases, the beam enters the Fresnel regime and the sensor is therefore also affected by variations in the pupil intensity that arise from scintillation and pupil instability. Fully analyzing this parameter space will be crucial for future sensor optimization.

The size of the lens ring aperture determines how much of the beam's central core is diverted to the sensor. As the edges of the beam are more susceptible to higher order modes and asymmetries, using more of the beam's core will result in more reliable measurements. However, this will also reduce the fraction of light available for science measurements. This trade off is the key design choice that will be determined by future use cases and implementations. In addition to the size of the central aperture, the NA can be used to slightly change the ratio between sensor signal and SMF coupling. Given the right optical system, it would be possible to perform individual adjustments of this trade off for each observed target.

6.4.4 Future applications

The system presented in this work was optimized to be used with the iLocator acquisition camera at the LBT, however there are other diffraction-limited systems where the technology can find application. As discussed in Sec. 6.4.1, the performance is limited by residual AO aberrations, and thus the most beneficial application will be with systems that feature as little residual wavefront aberrations as possible.

Besides current and future ExAO system at large observatories, the MLR-TT sensor can have an advantage for small observatories, free-space optical communication systems and space based applications that employ diffraction-limited telescopes. In these systems, the sensor can be integrated in a very compact fashion without the need for additional optical components in the optical train reducing complexity and mechanical footprint.

6.5 Conclusion

We presented the first on-sky results of our novel 3D-printed, fiber-based tip-tilt sensor (MLR-TT). The sensor was tested with the iLocator acquisition camera at the Large Binocular Telescope in November 2019. The system consists of a 3D-printed micro-lens

ring that uses six multi-mode fibers to reconstruct the centroid position, while providing an almost unobscured aperture where a science single-mode fiber is positioned. This concept features a very small opto-mechanical footprint and degrades the maximum single-mode fiber coupling efficiency by 15%, which is comparable to typical losses due to beam aberrations.

We showed that the fundamental principle works well and the sensor is able to reach a maximum reconstruction accuracy of $0.19 \lambda/D$ in each tip and tilt, however, the system was not able to improve single-mode fiber coupling efficiency. The majority of the vibration was measured in frequencies between 10-20 Hz, but the majority of the reconstruction error was shown to occur in low frequencies between 1-10 Hz. This error in reconstructing the centroid depended strongly on estimated SR and subsequent simulations were able to recreate this trend, suggesting that residual aberrations were the dominating noise source that limited performance.

These findings will help to tune both the optical design and reconstruction algorithm to improve the centroid measurements and to reduce the impact of residual aberrations. Alternatively, the respective frequency range can be filtered or corrected using another sensor to minimize its impact.

We conclude that the MLR-TT sensor is best suited for applications requiring fast correction with low higher-order wavefront distortions while benefiting from its compact nature. This includes extreme adaptive optics systems, compact systems at small diffraction-limited telescopes and space based applications. We also note that the MLR-TT sensor operates very close to the fiber coupling surface, it is free of non-common path aberration and can therefore be used to track drifts and perform guiding in a closed-loop system where calibration between the wavefront sensor and fiber is difficult.

Acknowledgments

P.H., R. J. H., and A.Q. are supported by the Deutsche Forschungsgemeinschaft (DFG) through project 326946494, ‘Novel Astronomical Instrumentation through photonic Re-formatting’. This project has received support from the European Union’s Horizon 2020 research and innovation program under grant agreement No 730890. NAB, AGB and TJM acknowledge funding from UKRI Science and Technology Facilities Council (ST/T000244/1: NAB, TJM ; ST/P000541/1: AGB, NAB, TJM).

This research made use of HCIPy, an open-source object-oriented framework written in Python for performing end-to-end simulations of high-contrast imaging instruments (Por et al., 2018), Astropy, a community-developed core Python package for Astronomy (The Astropy Collaboration et al., 2013, 2018) Numpy (Harris et al., 2020) and Matplotlib (Hunter, 2007).

We thank the reviewers for the time improving this manuscript and Romain Laugier for useful information about SMF use in interferometry.

7 Discussion

7.1 Summary

This thesis summarized the research and development work of this Ph.D. project. It covered a wider range of common development aspects in astronomical instrumentation. The project included optical design, mechanical design, optical laboratory testing, electrical and digital controlling as well as performing on-sky observations with the subsequent data analysis and visualization.

The presented research is based on the work by Dietrich et al. (2017). In this thesis, their concept was modified and further optimized to fit the requirements for testing at the LBT. For lens testing and developing, the KOOL was adapted and set up, as described in Chapter 4. Around the MLR-TT sensor itself, a system was designed consisting of a read-out camera and a control computer using a custom control algorithm. This was then integrated with the iLocator acquisition camera in the lab, see Chapter 5. And after final optimizations, the system was tested on-sky at the LBT, and the data were analyzed and published (Chapter 6; Hottinger et al., 2021).

The sensor was able to reconstruct the centroid position of the PSF but was unable to significantly improve the SMF-coupling. For this, a number of causes were found: Most importantly, the flux in the residual AO aberrations caused a false signal. This noise led to a reconstruction error of $\sim 0.19 \lambda/D$ in both tip and tilt measurements. Additionally, latency in the control loop limited the correction in the desired frequencies.

The following chapter will summarize various aspects of these results in more detail. For this, the whole telescope system is formalized. The reconstruction errors and the corresponding algorithms are discussed. Then, the different aspects of the controller are analyzed. The next steps that should be taken to further develop this concept are outlined, the possible use cases and the context of this work are discussed.

7.2 System overview

The on-sky system operation was first designed theoretically in a block diagram for an overview of its working functionality. Fig. 7.1 shows the functional block diagram of all components that interact in this system. It starts with the wavefront entering the telescope aperture, being measured and modified by the different control systems, and finally coupled into the fiber to be further processed by the science instrument.

This can be sorted into three separate but interacting subsystems: Firstly, the AO system measures the wavefront and sends an appropriate correction signal to a DM. Then, the *iLocator acquisition camera* receives the collimated beam and applies additional tip-

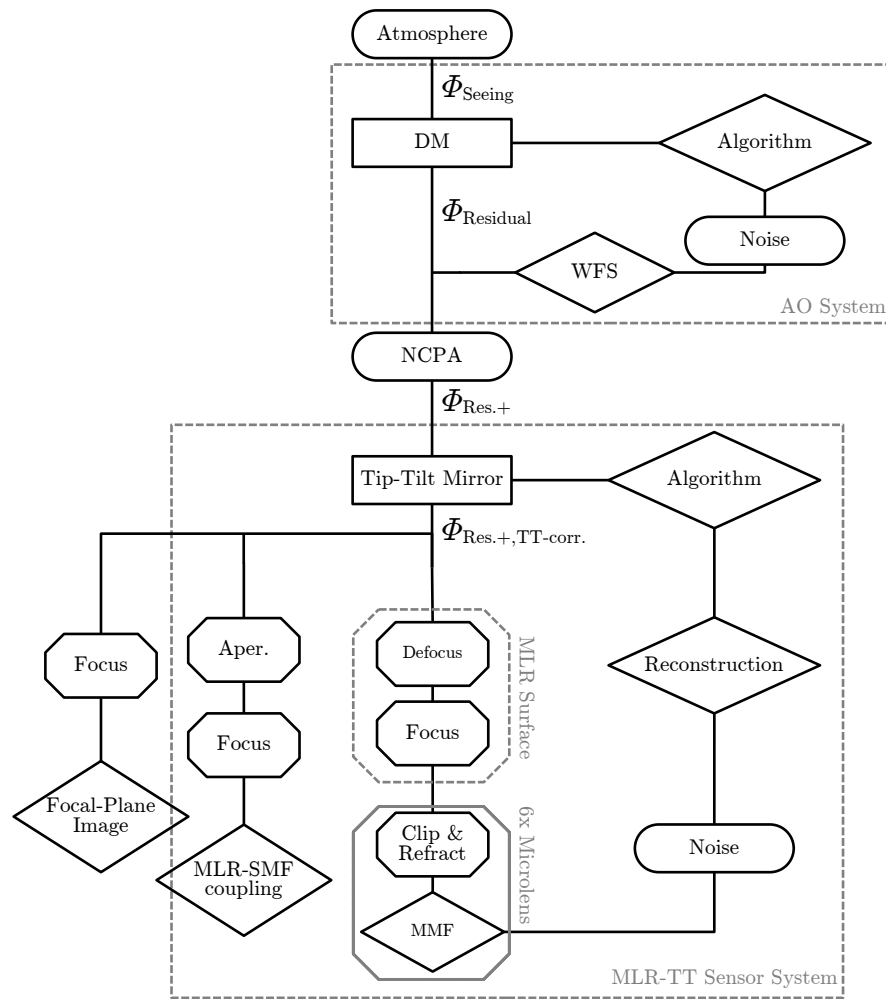


Figure 7.1: Block diagram of the telescope system setup composed of the AO system and the MLR-TT Sensor system. The iLocator’s unmodified SMF coupling and its native quad-cell tip-tilt sensing is not shown.

tilt correction before recording a focal plane image and coupling into the SMF. Finally, the *MLR-TT sensor system* introduced in this work is an add-on that is temporarily installed within the iLocator acquisition camera. It implements an alternative second tip-tilt measurement and control loop, replacing iLocator’s native quad-cell tip-tilt measurement.

7.3 Mathematical framework

To describe the system presented above, the following mathematical framework collects all physical models as introduced in Chapter 2.1.

Initially, the incoming wavefront of the target is assumed to be a flat wavefront given by

$$\psi_{\text{star}}(\vec{r}, t) = Ae^{i(\phi(\vec{r}, t) + 2\pi\nu t + \vec{k} \cdot \vec{r})} \quad . \quad (7.1)$$

Atmospheric turbulence (Seeing) then imposes both an amplitude factor $\chi_A(\vec{r}, t)$ and a phase delay $\Phi_A(\vec{r}, t)$, in addition to the telescope's primary mirror aperture acting as a constant optical pupil $\chi_{\text{Primary}}(\vec{r})$ given by

$$\psi_{\text{Seeing}}(\vec{r}, t) = \chi_{\text{Primary}} \cdot \chi_A(\vec{r}, t) \cdot e^{i\Phi_A(\vec{r}, t)} \cdot \psi_{\text{star}}(\vec{r}, t) \quad . \quad (7.2)$$

Then the DM, which corrects for the atmospheric perturbations adds another phase delay Φ_{DM} as instructed by the control system given by

$$\psi_{\text{Residual}}(\vec{r}, t) = e^{i\Phi_{\text{DM}}(\vec{r}, t)} \psi_{\text{Seeing}}(\vec{r}, t) \quad . \quad (7.3)$$

For this AO control loop, the WFS measures the wavefront slope and transforms it into a wavefront error $\vec{e}(\vec{r}, t)$ with respect to the desired wavefront. A noise term w represents the corresponding noise in the measurement. The control algorithm, an integrator, calculates the correction signal $\Phi_{\text{DM}}(\vec{r}, t)$ that is sent to the DM. For this, a reconstruction matrix K transforms the wavefront error to the corresponding correction signal. The measurement is temporally offset by a delay in time δT and multiplied by a gain factor γ . The previous control value is dampened by the integrator decay value α given by

$$\Phi_{\text{DM}}(\vec{r}, t) = \alpha\Phi_{\text{DM}}(\vec{r}, t - T) + \gamma K(\vec{e}(\vec{r}, t - \delta T) + w) \quad . \quad (7.4)$$

The additional NCPAs that occur after the WFS, add an additional phase delay. This consists of vibrations $\Phi_{\text{NCP, vib.}}(\vec{r}, t)$ and of higher-order modes $\Phi_{\text{NCPA}}(\vec{r}, t)$ given by

$$\psi_{\text{NCP res.}}(\vec{r}, t) = e^{i\Phi_{\text{NCP, vib.}}(\vec{r}, t)} e^{i\Phi_{\text{NCPA}}(\vec{r}, t)} \psi_{\text{Residual}}(\vec{r}, t) \quad . \quad (7.5)$$

Within the iLocator acquisition camera, a fast-steering tip-tilt mirror corrects for residual tip-tilt with an additional phase correction $\Phi_{\text{tip-tilt}}(\vec{r}, t)$ given by

$$\psi_{\text{iLocator}}(\vec{r}, t) = e^{i\Phi_{\text{tip-tilt}}(\vec{r}, t)} \psi_{\text{NCP res.}}(\vec{r}, t) \quad . \quad (7.6)$$

Afterward, iLocator's focal plane camera (ANDOR Zyla 4.2 Plus sCMOS) records an image of the target. This can be approximated by the Fraunhofer diffraction equation, which corresponds to a Fourier transformation of the EM field in the pupil. This EM field in the focal plane $\psi_{\text{Andor}}(\vec{r}, t)$, is then used to calculate the light intensity distribution

7 Discussion

$I_{\text{Andor FP}}(\vec{r}, t)$ as

$$I_{\text{Andor FP}}(\vec{r}) = \psi_{\text{Andor FP}}(\vec{r}, t)^* \cdot \psi_{\text{Andor FP}}(\vec{r}, t) = \|\psi_{\text{Andor FP}}(\vec{r}, t)\|^2 \quad (7.7)$$

$$= \left\| \int_{\text{Pupil}} \psi_{\text{iLocater}}(\vec{r}', t) \cdot e^{-\frac{i2\pi}{\lambda}(\vec{r}' - \vec{r})} d\vec{r}' \right\|^2 \quad (7.8)$$

SMF coupling takes place at the fiber position. The coupling efficiency ρ_{SMF} is calculated with the overlap integral between the EM field of the incoming beam $\psi_{\text{FP}}(\vec{r}, t)$ and the EM field of the fundamental mode $\psi_{\text{SMF}}(\vec{r}, t)$ that the fiber accepts as

$$\rho_{\text{SMF}}(t) = \left(\frac{\left\| \int \psi_{\text{FP}}(\vec{r}, t) \cdot \psi_{\text{SMF}}^*(\vec{r}, t) d\vec{r} \right\|}{\|\psi_{\text{FP}}(\vec{r}, t)\| \cdot \|\psi_{\text{SMF}}(\vec{r}, t)\|} \right)^2 \quad (7.9)$$

While the coupling itself takes place at the fiber, the calculation is independent of the position at which the overlap integral is performed.

In the case of SMF-coupling as part of the MLR-TT sensor, the clipping of the incoming beam by the MLR needs to be accounted for. For this, the EM field is calculated by adding a phase modification $\Phi_{\text{MLR defocus}}(\vec{r}, t)$ to the field prior to the Fourier transformation. This is equivalent to Fresnel diffraction close to the optical axis by adding a defocus mode to the wavefront leading to the evaluation of the field at the MLR surface. This transformation is done to obtain the field of both the telescope wavefront $\psi_{\text{MLR surf.}}(\vec{r}, t)$ and the fundamental mode of the SMF $\psi_{\text{SMF-MLR surf.}}(\vec{r}, t)$ given by

$$\psi_{\text{MLR surf.}}(\vec{r}, t) = \int_{\text{Pupil}} e^{i\Phi_{\text{MLR defocus}}(\vec{r}, t)} \psi_{\text{iLocater}}(\vec{r}', t) \cdot e^{-\frac{i2\pi}{\lambda}(\vec{r}' - \vec{r})} d\vec{r}' \quad (7.10)$$

$$\psi_{\text{SMF-MLR surf.}}(\vec{r}, t) = \int_{\text{Pupil}} e^{i\Phi_{\text{MLR defocus}}(\vec{r}, t)} \psi_{\text{SMF pupil}}(\vec{r}', t) \cdot e^{-\frac{i2\pi}{\lambda}(\vec{r}' - \vec{r})} d\vec{r}' \quad (7.11)$$

The fiber's coupling efficiency is calculated equivalently to Eq. 7.9. The overlap integral is performed only over the central aperture of the MLR, where the light is not refracted by the lenses. The whole field is considered for normalization as

$$\rho_{\text{MLR-SMF}}(t) = \left(\frac{\left\| \int_{\text{MLR aper.}} \psi_{\text{MLR surf.}}(\vec{r}, t) \cdot \psi_{\text{SMF-MLR surf.}}^*(\vec{r}, t) d\vec{r} \right\|}{\left\| \int_{\text{MLR aper.}} \psi_{\text{MLR surf.}}(\vec{r}, t) d\vec{r} \right\| \cdot \left\| \int_{\text{MLR aper.}} \psi_{\text{SMF-MLR surf.}}^*(\vec{r}, t) d\vec{r} \right\|} \right)^2 \quad (7.12)$$

The MLR-TT sensors MMF-coupling is calculated by integrating the intensity of the EM field at the MLR surface ($\psi_{\text{MLR surf.}}(\vec{r}, t)$, Eq. 7.10) over the respective lenslet's surface, producing the six sensor fluxes F_X ($X = 1 \dots 6$) of the sensor, including the corresponding measurement noise $\omega_{\text{MMF}, X}$. This assumes that all the light that reaches

the MLR surface will couple into the corresponding MMF and does not account for reflection, absorption, and mismatching of the fiber's NA as

$$F_X = \int_{\text{lenslet}_X} I_{\text{MLR surf.}} d\vec{r} + \omega_{\text{MMF},X} \quad (7.13)$$

$$= \int_{\text{lenslet}_X} \|\psi_{\text{MLR surf.}}(\vec{r}, t)\|^2 d\vec{r} + \omega_{\text{MMF},X} \quad . \quad (7.14)$$

Using a reconstruction algorithm $R_{\text{TT-recon.}}$, the six sensor fluxes F_X are then transformed to a centroid position r_{centroid} corresponding to the tip and tilt as

$$r_{\text{centroid}} = R_{\text{TT-recon.}}(F_{1\dots6}) \quad . \quad (7.15)$$

In the on-sky setup, the reconstruction is achieved by performing a least-squares fit of the normalized sensor fluxes $\hat{F}_X = (F_X - N_{\text{offset},X})/N_{\text{scale},X}$ in the parametrization of their azimuthal position θ_X to a sinusoidal function with a frequency of 1 Hz where the best-fit amplitude r yields the radial centroid position and the best-fit phase θ yields the azimuthal position given by

$$(r, \theta)_{\text{centroid, raw}} = \arg \min_{r, \theta} \sum_{X=1}^6 \left(\hat{F}_X - r \cdot \sin(\theta_X + \theta) \right)^2 \quad . \quad (7.16)$$

This calculation was performed in the control system as employed on-sky and features a rather complicated procedure. The calculation, however, can be performed in a computationally much less expensive manner as the results just represent the amplitude and phase of the corresponding unit frequency of 2π . Then the parameters can be determined by a simple DFT of first order with

$$a_1 = \sum_{X=1}^6 \left(\hat{F}_X \cdot \sin \theta_X \right) \quad \text{and} \quad (7.17)$$

$$b_1 = \sum_{X=1}^6 \left(\hat{F}_X \cdot \cos \theta_X \right), \quad \text{yielding} \quad (7.18)$$

$$r_{\text{centroid, cal.}} = \sqrt{a_1^2 + b_1^2} \quad \text{and} \quad (7.19)$$

$$\theta_{\text{centroid, cal.}} = \arctan b_1/a_1 \quad . \quad (7.20)$$

The polar coordinates are then corrected with calibration parameters $C_{r/\theta,i}$ and $\phi_{r/\theta,i}$

7 Discussion

($i = 1 \dots 5$), a DFT of 5th order, modifying the parameters with

$$r_{\text{centroid, cal.}} = r_{\text{centroid, raw}} \cdot \sum_{i=1}^5 C_{r,i} \cdot \sin(\omega_i \cdot \theta + \phi_{r,i}) \quad \text{and} \quad (7.21)$$

$$\theta_{\text{centroid, cal.}} = \theta_{\text{centroid, raw}} + \sum_{i=1}^5 C_{\theta,i} \cdot \sin(\omega_i \cdot \theta + \phi_{\theta,i}) \quad . \quad (7.22)$$

The correction factors are determined by a calibration routine that introduces a circular tip-tilt motion in order to measure any unwanted asymmetry of the sensor response (see Sec. 6.2.6).

The resulting calibrated coordinates $(r, \theta)_{\text{centroid}}$ are then transformed to Cartesian coordinates $\vec{r}_{\text{centroid}} = (x, y)_{\text{centroid}}$ as

$$x_{\text{centroid, cal.}} = r_{\text{centroid, cal.}} \cdot \cos(\theta_{\text{centroid, cal.}}) \quad (7.23)$$

$$y_{\text{centroid, cal.}} = r_{\text{centroid, cal.}} \cdot \sin(\theta_{\text{centroid, cal.}}) \quad . \quad (7.24)$$

The MLR-TT control loop again uses an integrator algorithm to feed the iLocater's tip-tilt mirror for closed-loop correction. This is done in the same fashion as the main AO-loop given by

$$\Phi_{\text{tip-tilt}}(\vec{r}, t) = \alpha_{\text{MLR-TT}} \Phi_{\text{MLR-TT}}(\vec{r}, t - T) \quad (7.25)$$

$$+ \gamma_{\text{MLR-TT}} \mathbf{K}_{\text{MLR-TT}} (\vec{e}_{\text{MLR-TT}}(\vec{r}, t - \delta T)) \quad . \quad (7.26)$$

7.4 Reconstruction error and noise

The sine-fit algorithm does not have a particular theoretical foundation other than its representation of a periodic pattern. The calibration routine then corrects for any deviation from the sine pattern itself. The main motivation for using this particular algorithm was its superior laboratory performance compared to a simple CoM algorithm, particularly with respect to its sensitivity to noise. A more sophisticated algorithm would need to take into account the actual optical propagation within the system and the MLR-TT sensor.

But any algorithm will face the challenge to not only sense the centroid position of the incoming beam but also cope with changing residual AO aberration. In the previous chapter, it was suggested that these residual aberrations can severely impact sensor performance. The low-order modes have the most power in low radial and azimuthal orders and thus also have the most prominent asymmetries in the focal plane and at the optical plane of the MLR surface. As the low-order modes have larger-scale perturbations, the associated timescale of these aberrations is also larger, and they will thus have a smaller frequency component associated with them than the other modes. From the on-sky analysis (see Sec. 6) is shown that the highest impact occurred at frequencies below 15 Hz. Additionally, asymmetries that arise from scintillation in the pupil can

introduce an error in the reconstruction.

At first sight, the error in reconstruction that arises from the residual aberrations can be considered noise, as they are uncorrelated at the time of the measurement. As the MLR-TT sensor does have six output values, while the centroid position has only two degrees of freedom, it opens up the possibility to implement more advanced reconstruction algorithms that filter or ignore these misleading signals.

Fig. 7.2 shows initial work with Barnaby Norris using the on-sky measurements to train a machine learning (ML) algorithm. Early results from across multiple datasets suggest that the deployment of a neural network could slightly decrease the reconstruction error by $\sim 10\%$, but it is unable to fundamentally avoid the error imposed by residual aberrations.

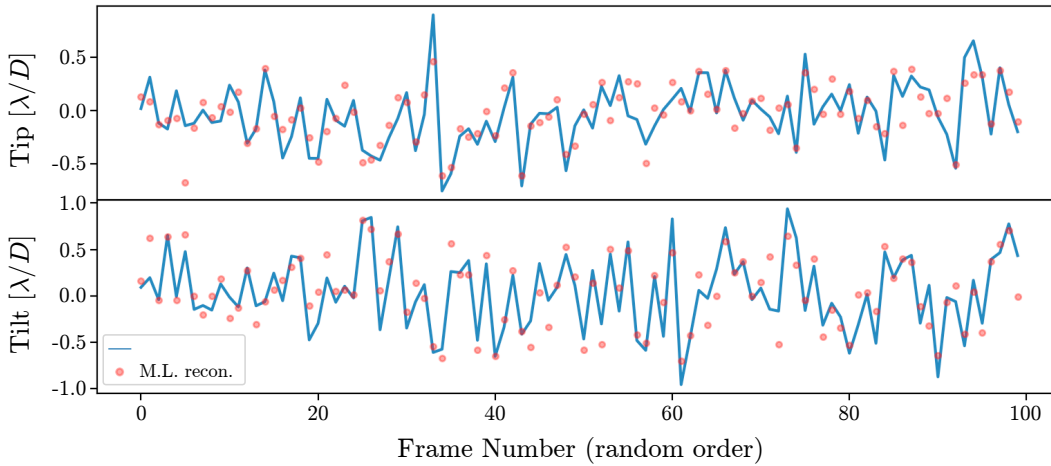


Figure 7.2: Reconstruction of tip/tilt with machine learning (ML) using neural networks (red dots). Performed on on-sky measurements (HD12354/1) including noise and residual AO aberrations. After training, the algorithm is able to achieve an accuracy of $0.175 \lambda/D$ (RMS error) in comparison with centroid position as measured with a Gaussian fit on the Andor focal plane camera (blue lines). This is a $\sim 8\%$ improvement compared to $0.195 \lambda/D$ on the same dataset by the reconstruction algorithm presented in this work.

(Courtesy of Barnaby Norris, private communication)

In the long term, this also opens up the possibility to reconstruct not only tip-tilt modes but other modes as well. Fig. 7.3 again shows initial work performed with Barnaby Norris succeeding to reconstruct multiple modes with the use of neural networks. These early results are limited to simulated sensor responses that do not introduce any other modes, residual aberrations, or noise. The impact of these is the focus in the ongoing investigations.

Additionally, the fact that the most influential aberrations change on a longer timescale could allow making use of the fact that there is indeed a temporal correlation which could

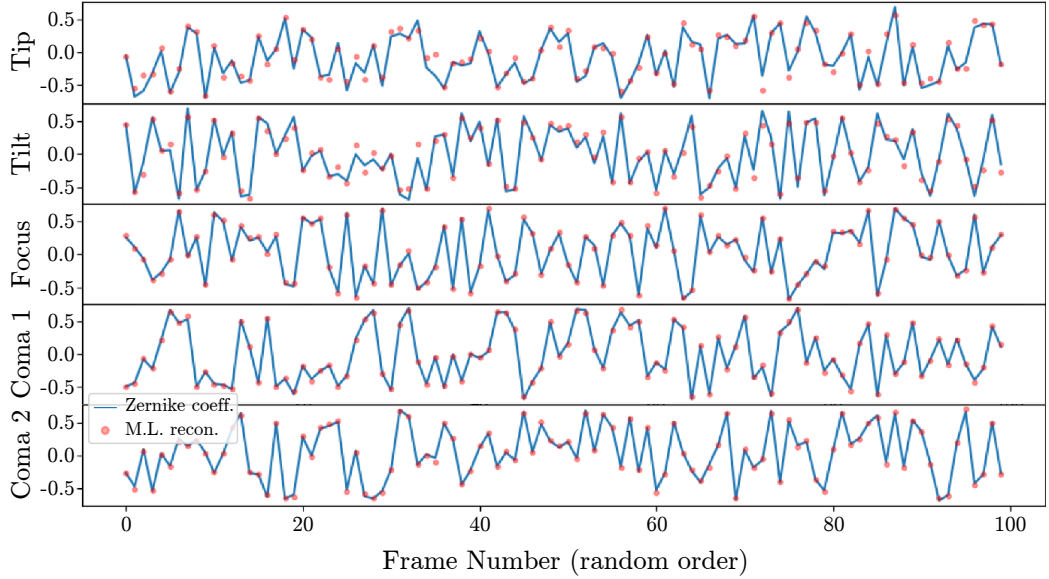


Figure 7.3: Reconstruction of 5 Zernike modes with machine learning (ML) using neural networks (red dots). Performed on simulated MLR-TT responses with 5 uniformly random coefficients between -0.7 and 0.7 without additional aberrations or noise. The ML algorithm is able to reconstruct the introduced coefficients (blue lines) with an RMS error of 0.0582 .

(Courtesy of Barnaby Norris, private communication)

be exploited or additional lower frequency sensor measurements could be incorporated. Future analysis will focus on quantifying the impact of these different factors. For this, extensive simulations need to be performed that account for the impact of the atmosphere under different observing conditions and the expected vibrations of the telescope. This will result in a quantified sensitivity of the sensor and the corresponding applied reconstruction algorithm with respect to the different distortions of the wavefront, namely the different modes as expressed in the Zernike basis and possible scintillation. The impact of different modes can then be correlated to the corresponding frequencies.

7.5 Noise

Fundamentally, there is also well-known uncorrelated noise that will cause erroneous sensor measurements. First, detector noise occurs per used pixel and depends on the environment. It consists mainly of read-out noise (RON) that occurs when resetting and reading pixels and dark current (DC) noise from random quantum fluctuations within the detector. Secondly, photon noise arises from the quantum statistics of detecting the photons themselves. This depends on the number of photons that are detected.

Therefore, the total noise σ is thus the quadrature sum of the RON σ_{RON} , which is

the result of the underlying electronics with unspecified statistics, the statistical error of the Poisson statistics that describe the behavior of DC noise $\sigma_{\text{DC}} = \sqrt{\text{DC}}$ and the photon noise $\sigma_{\text{photon}} = \sqrt{N_{\text{photon}}}$, depending on the number of detected photons N :

$$\sigma = \sqrt{\sigma_{\text{RoN}}^2 + \text{DC} + N_{\text{photon}}} \quad (7.27)$$

Because this noise is truly uncorrelated, it does not have a specific frequency component and can therefore be regarded as white noise. While on-sky analysis has shown that this noise is negligible compared to the errors caused by the algorithms and the noise originating from residual aberrations, their impact on the measurements needs to be quantified. Synthetic noise simulation where uncorrelated noise was added to the on-sky measurement reveals a SNR of ~ 4 will lead to a combined centroid reconstruction noise of $1 \lambda/D$.

7.5.1 Reference error

It should also be mentioned that the measurement reference itself is associated with uncertainty. The reference centroid position was determined by a Gaussian fit to the Andor focal plane image. This introduces systematic error as the Gaussian fit is only an approximation of the centroid position and is susceptible to asymmetries of the PSF. In principle, this asymmetry correlates with the asymmetry that the MLR-TT sensor observes, albeit in a different optical manner. Furthermore, as shown in Sec. 2.2.2, the coupling efficiency is mathematically described by an overlap integral of the PSF with the near-Gaussian fundamental mode of the SMF. This justifies the use of a Gaussian fit as a proxy of the desired metric, although the desired impact should be analyzed in more detail in the future.

The impact of reference error due to NCP effects was also considered, but daytime observations did not suffer from the same inaccuracies. As vibrational impact within the iLocator acquisition camera should be in the same order, the impact by NCPA was determined to be negligible.

Additionally, the focal plane images also suffer from camera and photon noise that can heavily impact the reference measurements. Synthetic noise modeling on the observed images revealed that the reference camera noise does contribute to, but does not dominate the accuracy of the measurement.

7.6 Latency

All control systems are affected by latency that occurs when working with discrete time steps. The measured sensor data need to be read out and processed before the corresponding correction signal can be sent to the appropriate device. This means that the control always lags behind the measurement, limiting the frequencies that the system can correct.

To test the latency of the on-sky system at the LBT, an instant disturbance was introduced to the tip-tilt mirrors and the number of frames was measured until the

7 Discussion

sensor was able to sense this disturbance. This was repeated for multiple framerates to find the best suitable framerate to work with. This turned out to be 500fps where the delay was two frames overall, corresponding to 4ms (see Fig. 7.4).

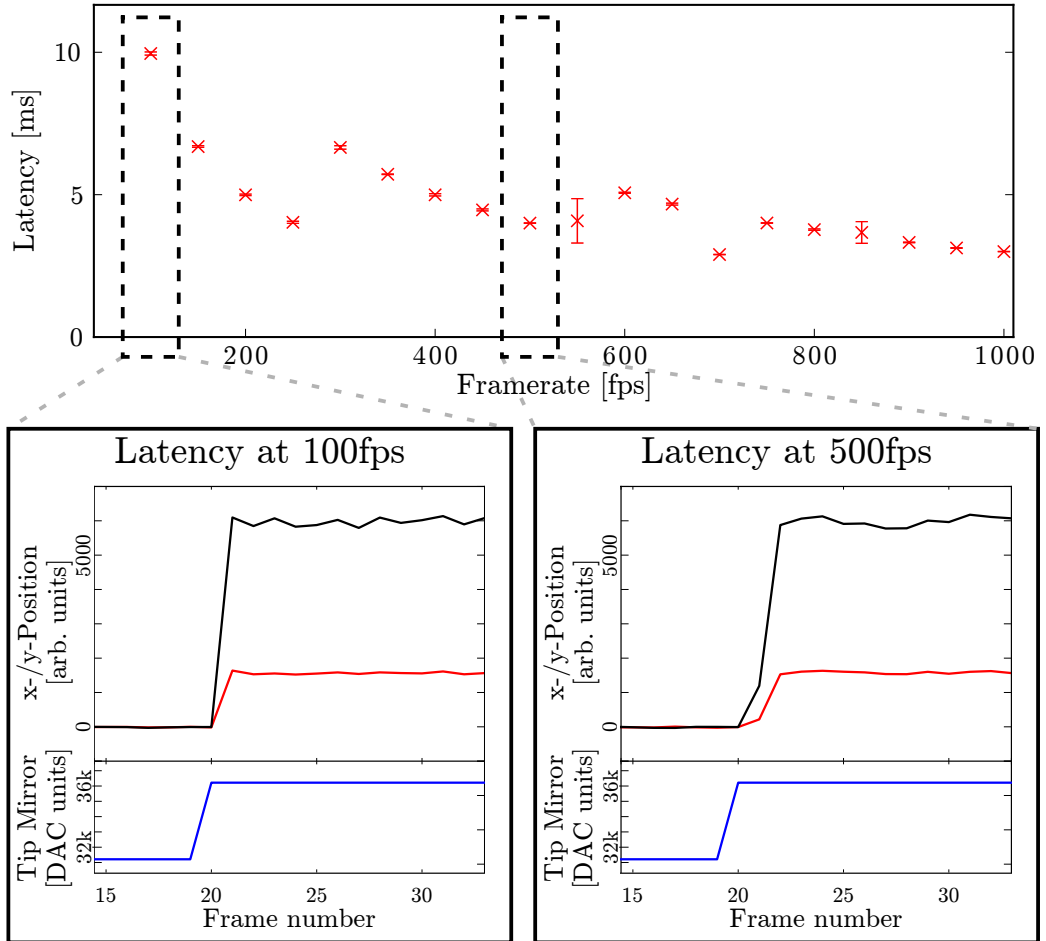


Figure 7.4: **Top panel:** Latency of MLR-TT sensor system on-sky in ms as a function of framerate (1/s). **Bottom panels:** Step response as measured by the sensor. The centroid x - and y -position (black/red) as measured after introducing an offset in one of the axes of the tip-tilt mirror.

There are a number of components that contribute to this delay, such as:

- Read out procedure by the detector
- Data transfer from detector to computing unit
- Image processing and normalization
- Centroid reconstruction

- Calculation of the correction signal by the control algorithm
- Data transfer to the correction component
- Physical reaction of the correction component, in this case, mechanical movement of the tip-tilt mirror

In order to improve the latency of the whole system, each of these components can be optimized. The overall computational delay time was estimated at ~ 2 ms. The image was recorded with a window size of 128×128 pixels and subsequently corrected and integrated with the highly optimized DARC software. The reconstruction algorithm, on the other hand, is quite resource-demanding, as it performs an optimization algorithm, which could be optimized significantly or even replaced by a fundamentally different approach. Furthermore, the mechanical movement of the tip-tilt mirror plays a significant role with ~ 2 ms as a whole half-inch mirror needs to rotate. The PID controller that steers this component is already optimized but other measures like reducing mirror weight or even aiming for an integrated photonic solution should be kept in mind.

7.7 Controlling

The control algorithm uses the sensor readings as input and calculates the appropriate correction signal that is sent to the tip-tilt mirror. Although measuring with a sensor is a vital part of achieving a good result, it is important to understand and optimize the procedure that follows this measurement.

In the first step, the characteristics of the disturbance that is to be corrected need to be analyzed. The residual tip-tilt error at the iLocator acquisition camera has a number of different origins. First, vibrations within the telescope and atmospheric distortions that have amplitudes or frequencies that cannot be sensed or corrected by the AO system. Secondly, NCP vibrations that occur after the WFS of the AO system. Usually, the tip-tilt distortions by the atmosphere have rather low frequencies that can be both sensed and corrected by the AO system.

However, the vibrations throughout the telescope can have very large amplitudes as the components only need to move marginally for the optical beam to be distorted well over the diffraction limit. Additionally, the vibration downstream of the WFS will not be detected at all and will need to be sensed in the first place. Most vibrations will occur at frequencies that are related to the resonances of the mechanical structure. These resonance frequencies are then very prominent in the spectral analysis of the disturbance.

Fig. 7.5 shows the PSD of both tip and tilt at the LBT as measured from the centroid reconstruction from the Andor camera images at the focal plane of the iLocator acquisition camera. It features two very prominent peaks between 10 Hz and 20 Hz, at around 30 Hz and additional disturbance at 50-60 Hz and 80 Hz. The corresponding cumulative representation (Fig. 7.5, right panel) reveals that 60-70% of the power of is present in the regime of 10-20 Hz.

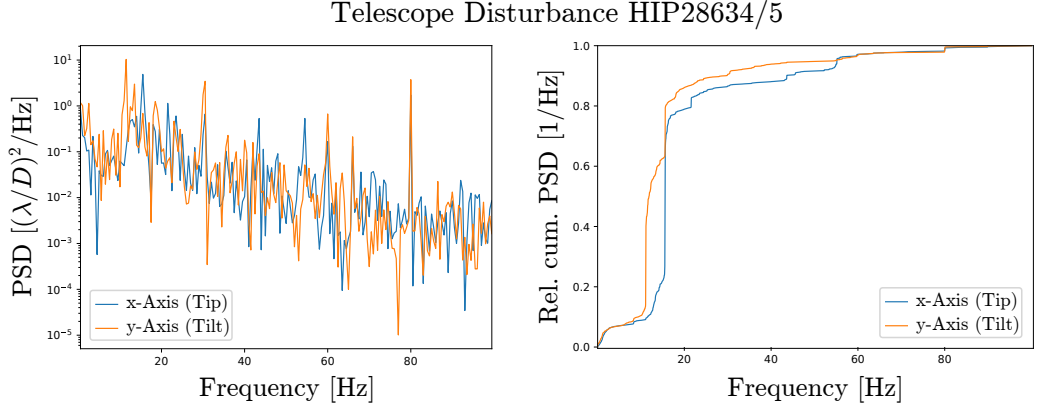


Figure 7.5: Power spectral density (PSD) of tip and tilt disturbance as measured by the Andor focal plane camera on-sky, without additional correction. Target HIP28634/5. **Left panel:** logarithmic scale PSD; **right panel:** relative cumulative PSD.

Among many AO systems and in this work as well, an integrator control algorithm is used. This uses the most recent sensor measurement, reconstructs the centroid, transforms it to the corresponding correction with the reconstruction matrix M_{RMX} and then scales it with the gain factor α to end with a correction signal that is added to the temporally preceding correction value. This preceding correction value is also multiplied by an integration factor γ , also known as leakage, to reduce the susceptibility of the control loop to become unstable as it corrects for noise-induced signals.

Besides the integrator setting of gain and leakage, the frequency that the correction loop operates and the latency (see above) of the system play a vital role when optimizations are to be performed. The PSD of the different components of a synthetic control system is shown in Fig. 7.6 with a one-dimensional uniform disturbance with arbitrary amplitude with white noise characteristics. The top panel of the figure shows the PSD of the disturbance itself, the central panel shows that of the corrected signal, and the bottom panel shows the corresponding rejection transfer function. The latter transfer function indicates the frequency ranges that the control algorithm can suppress (rejection <1) and where it overshoots and amplifies the disturbance (rejection >1). When considering a reasonable delay of 2 frames and a control loop frequency of 500 Hz with a gain of $\alpha = 0.4$ as shown in Fig. 7.6, the integrator is able to correct disturbances up to 30 Hz and then amplifying higher frequency disturbances.

Fig. 7.7 summarizes the performance of the control loop on-sky. The upper row shows the PSD of the tip (left) and tilt (right) uncorrected in open-loop operation. The middle row shows the same signal when the control loop is closed, correcting the disturbance. Then, looking at the measurement of the MLR-TT sensor (orange) with which the control loop runs, the PSD at lower frequencies is significantly reduced in closed-loop. The corresponding rejection transfer function (bottom row) again shows the frequencies

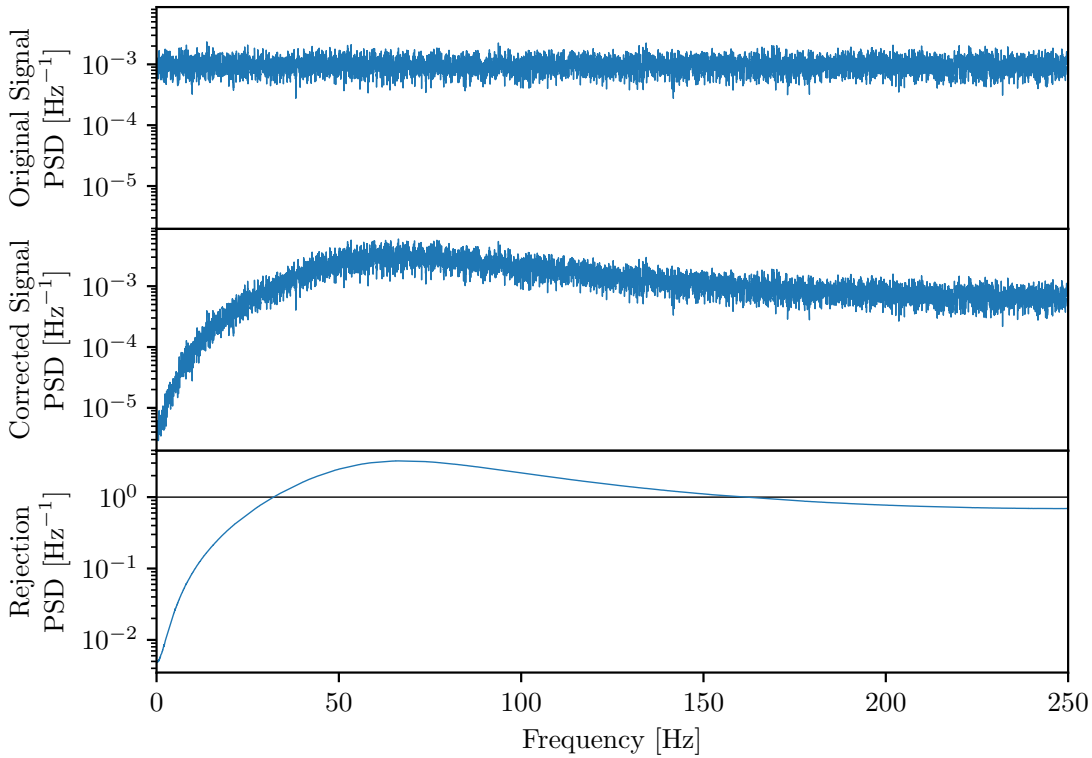


Figure 7.6: Modeled theoretical rejection of an integrator. Without measurement noise and running at a correction frequency of 500 Hz and with a latency of 2 frames. **Top:** PSD of random noise signal; **center:** PSD of corrected signal; **bottom:** rejection transfer function.

for which the control algorithm is able to correct. This is clearly successful for frequencies up to 10 Hz with mixed results in the intermediate frequency range before overshooting for frequencies beyond 30 Hz.

This shows that the control algorithm is not properly suited to correct the desired frequencies due to the discussed reasons, namely reconstruction error, loop frequency, and loop latency. One should also mention that, when considering the tip-tilt measured by the Andor focal plane camera (Fig. 7.7, blue line), there is a fundamental mismatch in the frequencies below 10 Hz. This is a strong indicator for the interpretation that the reconstruction algorithm of the MLR-TT sensor is particularly sensitive to wavefront distortions with low Zernike modes that evolve over slower timescales.

In order to improve the frequency response of the system, the obvious parameters of the control need to be improved. This is therefore the noise, the reconstruction error, and the latency, as mentioned in the previous sections. Additionally, the control loop needs to run at higher frequencies.

A promising prospect is the employment of a high-performance algorithm, such as linear-quadratic-Gaussian (LQG) control algorithms, that can incorporate the charac-

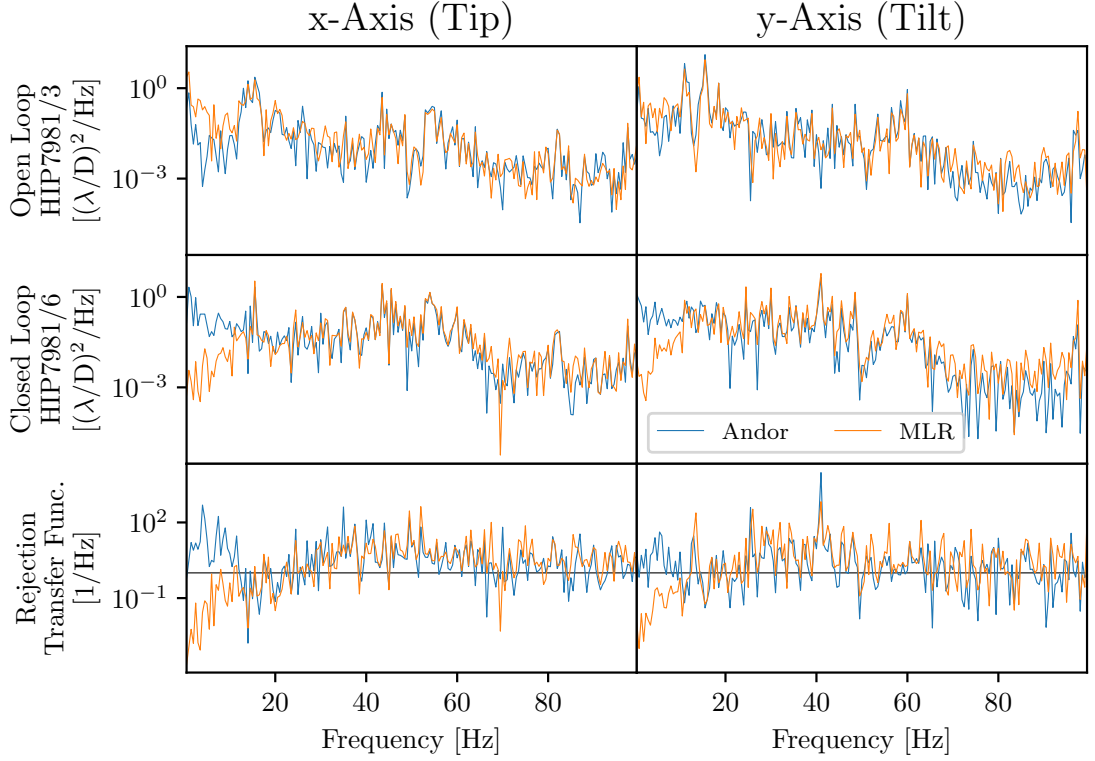


Figure 7.7: PSD of residual tip (x-Axis, left column) and tilt (y-Axis, right column) both as measured by the Andor focal plane camera (blue) and the MLR-TT sensor (orange). Compared between open-loop measurements (top) without any corrections, closed-loop (gain $\alpha = 0.4$) with the MLR-TT sensor system (center), and the corresponding rejection transfer function (bottom). Target HIP2981.

teristic of the disturbance and the system itself. LQG control has been shown to substantially improve AO systems both in laboratory environment (Petit et al., 2008; Guesalaga et al., 2013) and on-sky (Sivo et al., 2014; Petit et al., 2014; Poyneer et al., 2016).

Furthermore, it should be considered to support the control algorithm with additional data. The following sensor measurements are closely correlated. First, the WFS of the AO system itself, as it can provide insights into residual aberrations to overcome the error in reconstruction. Second, the Andor focal plane image can provide additional information about the PSF of the incoming beam to aid in centroid reconstruction, although at a lower temporal frequency, as it is less sensitive. Third, the existing vibration monitor infrastructure, such as the feed-forward accelerometer measurement could be used to aid the control algorithm.

7.8 Optical design

With regard to the optical design that was demonstrated on-sky, a lot of consideration was put in. In hindsight, this design needs to be revisited. In the following, the different parameters are discussed and the optical and mechanical constraints that might restrict them.

Two main parameters govern the working principle of the MLR-TT sensor. Firstly, this is the position at which the sensor picks off the beam, which corresponds to the height of the lens where its surface refracts the light to be redirected into the sensing fibers. Second, the size of the central aperture of the MLR. This governs how much light it will be able to couple into the science SMF and how much light from the outer edge of the beam will be used for sensing.

These two parameters are crucial as they govern which part of the telescope beam exactly is used for sensing and which part of the beam is used for the actual science processing. The residual aberrations that are propagated to the sensor and introduce reconstruction errors are heavily dependent on this.

Additional design choices and parameters can be changed in the system, including the following.

- The size of the MMFs and subsequently their spacing on the fiber face has a large impact on their ability to efficiently couple sensor light while coupling the least amount of background light and thus being responsible for the least amount of detector noise. This will also greatly govern the restrictions that are placed on MLR itself, as it needs to optically conform to the MMFs.
- The number of MMFs can also be significantly varied. The choice of six fibers was due to the highest fill factor of the hexagonal pattern. It should also be considered to introduce additional rings of fibers in order to gather more information about the wavefront.
- The shape of the MLR is obviously a major parameter that needs to be considered. This has a large number of free parameters as the surface of the lenses needs to be designed to refract the beam so that coupling is optimized while potentially rejecting residual aberration and background that can harm the performance of the sensor. In addition, the overall diameter of the lens must be set.

Although some design parameters are quite flexible, such as the shape of the MLR surface or the size of the MMFs, others are rather limited. The most prominent example is the separation of the fiber cores, as the current manufacturing technique does not modify their cladding, effectively limiting their separation. This was a simplified design choice because it avoided the need to source or produce specialty fibers or even use etching technology to modify their cladding. These design requirements can be overcome in the future. Similarly, the height of the MLR was limited due to manufacturing restrictions, but more modern two-photon lithography systems can overcome this issue.

The design was purely driven by geometric approximation of the system and did not consider residual aberrations. This approximation is only feasible to a certain extent, as

it may sufficiently model the refracting itself, but does not consider the exact intensity profile and wavefront phase at the sensor’s surface, and subsequently fails to accurately account for all optics. For this, a more accurate simulation pipeline needs to be considered to make further optimization feasible. Fig. 7.8 shows the geometric modeling (left panel) as performed for designing and wave-optical modeling (right panel) that proved to be more accurate for predicting the sensor response.

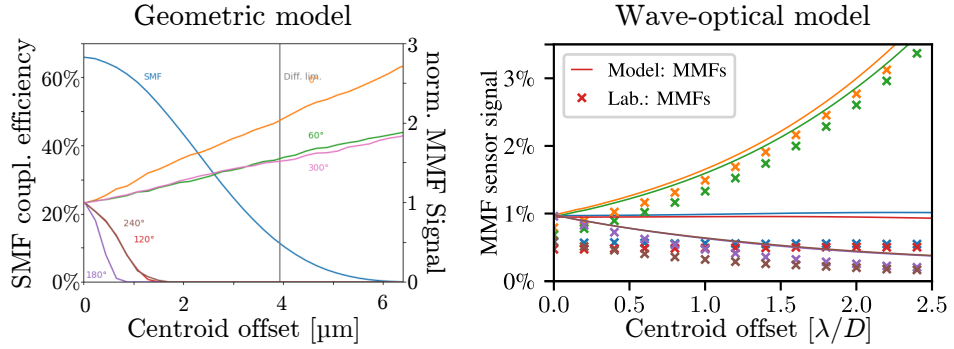


Figure 7.8: Comparison of different modeling approaches of the MLR-TT sensor response (solid lines) with the corresponding laboratory measurements (crosses). **Left panel:** geometric modeling (*adapted from Hottinger et al., 2019*); **right panel:** more accurate wave-optical simulation (*adapted from Hottinger et al., 2021*).

7.9 Co-design of the whole system

The previous sections outlined all the different components and aspects of the system that need to be refined further. Each of them has its own function that needs to be considered and optimized. But the overall merit of the system is not governed by the performance of the individual components but is measured by the end result of the whole operation. In the case of the MLR-TT sensor, the overall performance is measured by the amount of light that is coupled to the SMF.

Accurate measurement and correction of tip-tilt is a necessary step in doing so. But it is only one subsystem. Rather, all components must be taken into account to measure the eventual overall performance.

In this chapter, all information was gathered to create a pipeline that simulates the entire system, including its temporal behavior. Although the physical concepts of the system are well known, the full treatment of each component might be computationally too expensive. Therefore, a few approximations need to be made that need to be separately validated to be reasonable within the required accuracy.

The input of the model will have a wide variety of input parameters. First, this is the exterior environment, such as the characteristics of the disturbance and the optics of the telescope. This can be regarded as static, though their impact needs to be analyzed over

a certain range, as the environment may change due to changing observing conditions, telescope orientation, etc. Second, the design parameters of the MLR-TT sensor as outlined need to be optimized within their constraints.

Eventually, the system needs to be optimized with a reasonable algorithm like particle swarms that can both cope with the computational cost of simulating the whole system and find a feasible global maximum within the large parameter space.

7.10 Project continuity

The work presented in this thesis has shown that the sensor as demonstrated was not able to sufficiently sense and correct for tip and tilt vibrations. However, the concept of the MLR-TT sensor, as first described by Dietrich et al. (2017) and then developed throughout this work, surely poses a unique instrument that has the potential to satisfy expectations either in this application or in a more specific environment.

This work summarizes all the physical and practical concepts necessary for future researchers to continue the development. To further assist prospective development, it is also important to make the underlying designs and software available to the research community. Therefore, a GIT repository is maintained to hold both the archived design documents and the control software from the on-sky setup, the most prominent on-sky data, and the analysis and simulation scripts for subsequent publications and future development. It is publicly available at <https://gitlab.lsw.uni-heidelberg.de/phottinger/mlr-tt-sensor>.

8 Conclusion and future prospects

It is now important to consider the next steps to be taken from the presented insights. These are approaches to further develop the concept and the appropriate use cases where the sensor will have the most beneficial impact.

Results

The Königstuhl Observatory Opto-Mechatronics Laboratory (KOOL) setup was successfully set up with modifications and it was well suited to test and characterize the MLR-TT sensor and develop the system, providing a realistic telescope environment regarding vibrational capabilities.

The MLR-TT's lens design yielded a usable design, but the geometric approximation used to model its behavior did not suffice. While it was most likely good enough to model the rays and thus optimize the lenses' shape, it did not properly predict the sensor response. For a more thorough analysis, wave propagation also needs to be taken into account. Using Fresnel propagation to model the intensity distribution at the MLR surface was able to predict the sensor response much better.

In the on-sky setup, the system was unable to improve SMF coupling significantly. The coupling efficiency, in particular, fluctuates strongly, as it is sensitively dependent on many environmental factors.

Therefore, the reconstruction accuracy in reference to the simultaneously recorded focal plane images and the centroid position as reconstructed from it was used to determine the performance of the sensor. While there are errors associated with this reference as well, it is still a good approximation of the target. This reconstruction accuracy captures both the reconstruction error introduced by the sensor and the reconstruction algorithm, as well as the noise introduced by the various components of the system. In the best case, the sensor was able to achieve a reconstruction accuracy of $0.19 \lambda/D$ in both directions.

Subsequent analysis shows that this accuracy is mostly dominated by residual AO wavefront aberrations. This conclusion is based on two observations. First, the behavior of this error with respect to the approximated AO performance was simulated showing a strong correlation between the achieved SR and the resulting accuracy of the MLR-TT sensor. Second, the error is observed to dominate at temporal frequencies that are associated with the Zernike modes excited by the atmospheric turbulence.

While the above effects play the dominating role, a number of factors also have a significant impact and are found to limit performance, such as the latency of the system including the control loop calculations and correction mirror movement.

Sensor optimization

At first, the sensor needed to be optimized in order to fully capture its potential. The various aspects as listed in Sec. 7.9 such as the geometry of lenses and fibers and their optical properties played a significant role in the response of the sensor and therefore in its sensitivity. The parameter space of the design was large, making this optimization rather complex. In addition to the parameters mentioned in the current design of six sensing MMFs and a single MLR, the manufacturing constraints were rather small. This allows for many possible modifications to be imposed on the sensor that should be explored in order to find the best working setup.

The optimization process was particularly cumbersome, as the entire system needs to be taken into account in order to accomplish the necessary accuracy. This work has shown rigorously how different aspects of the whole optical system affect sensor performance, including observing conditions.

Use cases

The dependence of the performance on the environment implies that a very wide range of use cases should be considered in more detail. The cross-dependence between these parameters will make a generalized global optimization both analytically and computationally expensive. But a number of system environments stand out as particularly suited setups to be combined with the MLR-TT sensor.

The primary use case, as presented in this work, is the LBT as a very large telescope with state-of-the-art ExAO working near the diffraction limit. The large NCP aberrations and vibrations encountered at such observatories make tip-tilt stabilization necessary. Here, the MLR-TT sensor can make use of close positioning to the coupling at the fiber tip. However, as the complexity of these large telescopes is already at a very high level, the reduction in optical complexity by using the MLR-TT sensor is not that beneficial as the conventional options such as quad-cell detectors do not add substantial complexity.

Furthermore, the LBT AO system does not have special speckle and NCPA suppression as found in other ExAO systems such as SPHERE at VLT (Beuzit et al., 2008) or SCExAO at Subaru telescope (Jovanovic et al., 2015). These instruments were designed for high contrast, high angular resolution imaging and deploy even more specialized AO concepts, therefore potentially providing a more suitable input to the MLR-TT sensor with less residual aberration.

Apart from the large telescopes discussed above, near-diffraction-limited telescopes with diameters $D \lesssim r_0$ and hence without AO systems might also play an important application role. These are used in automated systems or as part of telescope arrays, potentially feeding an interferometric instrument. The particular benefit of such a system is the reduced complexity of the MLR-TT sensor both in integration and in operation and its very small opto-mechanical footprint.

Space-born telescopes also fall into this category. In the absence of atmospheric disturbances, these naturally work in the diffraction-limited regime and would benefit from

the small footprint. As they are not as prone to vibrations, the use of an MLR-TT sensor concept would primarily focus on guiding, reducing the requirements on sensitivity and speed.

Potentially, another range of applications arises if the concept design is fundamentally modified. Especially using a MMF as a central science fiber would make this a possible component for most telescope setups that use optical fibers.

All of the above applications can, in some way, also be related to optical communication, particularly free-space optical communication. This is an ever-growing field where low-cost, low-complexity solutions are very desirable.

System optimization

In this work, a practically limiting factor proved to be the feedback control system with its particular parameters.

Foremost, the reconstruction algorithm leaves room for improvement. This includes a better characterization of the current algorithm with regard to, for instance, the impact of different residual aberrations. Statistically based models should be explored in-depth, particularly including further investigation of ML approaches. Additionally, including the time domain to make use of temporal correlations should be considered. An optional output of the sensor could also be the reconstruction of more wavefront information than just the tip and tilt, such as more low-order Zernike modes.

The different components of the control system need to be optimized to reduce noise and latency of the system. As with most systems, the detector is a crucial element. It sets the baseline for the amount of camera noise and the maximum correction frequency that can be achieved. Furthermore, the computer system and the tip-tilt correcting mirror account for most of the control latency.

Finally, the interplay of these components, governed by the control algorithm, could be executed in a more advanced procedure. The integrator controller currently used only implements a simple control system. A more suitable, but albeit complex, algorithm could be the LQG controller that considers the system's properties, such as different noise sources.

Another potential consideration is to feed more sensors to the control algorithm. As the MLR-TT sensor itself features only limited information about the incoming light beam, the different sensor data might be able to break some of the occurring degeneracies. Examples include existing AO WFSs, focal plane images, SMF coupling intensities, mechanical information of telescope orientation, etc. However, having a grid of sensors that each work with a separate set of parameters, including frequency and noise characteristics, introduces another set of complexity that needs to be dealt with.

Research context

This demonstration of the MLR-TT sensor is, hopefully, only the beginning of more research for integrated microlens fiber sensors. Proven conventional solutions for the use case presented in this work exist such as quad-cell detectors or focal plane imaging.

8 Conclusion and future prospects

Additionally, the research field of integrated astrophotonic devices has only a limited amount of resources. But both application cases, inside and outside of astronomical observatories, and the vast possibilities for optimization, enhancement, and customization are benefits justifying further development.

Both the sensor itself and the integration of a WFS with a vital part of an instrument can be considered novel approaches to astronomical instrumentation. This proof-of-concept work has therefore shown a good possible path of where future integrated instrument design might be headed to. Yet, it has also shown the complexities that even a small system will encounter when integrated with the context of on-sky performance at astronomical telescopes.

Publications

First author to peer-reviewed publications

Hottinger et al. (2021) *JOSA B, astrophotonics feature edition*

P. Hottinger, R. J. Harris, J. Crass, P.-I. Dietrich, M. Blaicher, A. Bechter, B. Sands, T. Morris, A. G. Basden, N. A. Bharmal, J. Heidt, T. Anagnos, P. L. Neureuther, M. Glück, J. Power, J.-U. Pott, C. Koos, O. Sawodny, and A. Quirrenbach. On-sky results for the integrated microlens ring tip-tilt sensor. *JOSA B*, 38(9):2517–2527, Sept. 2021. ISSN 1520-8540. doi: 10.1364/JOSAB.421459

First author to conference proceedings

Hottinger et al. (2018) *SPIE 2018, Austin, TX, USA*

P. Hottinger, R. J. Harris, P.-I. Dietrich, M. Blaicher, M. Glück, A. Bechter, J.-U. Pott, O. Sawodny, A. Quirrenbach, J. Crass, and C. Koos. Micro-lens arrays as tip-tilt sensor for single mode fiber coupling. In R. Geyl and R. Navarro, editors, *Advances in Optical and Mechanical Technologies for Telescopes and Instrumentation III*, volume 1070629, page 77. SPIE, July 2018. ISBN 978-1-5106-1965-4. doi: 10.1117/12.2312015

Hottinger et al. (2019) *AO4ELT6, Quebec City, Canada*

P. Hottinger, R. J. Harris, P.-I. I. Dietrich, M. Blaicher, A. Bechter, J. Crass, M. Glück, J.-U. Pott, N. A. Bharmal, A. Basden, T. J. Morris, C. Koos, O. Sawodny, and A. Quirrenbach. Focal plane tip-tilt sensing for improved single-mode fiber coupling using a 3d-printed microlens-ring. In *Proceedings of AO4ELT6*, pages 1–7, Dec. 2019

Contributions to peer-reviewed publications

Anagnos et al. (2021)

Contributions: Research advice and results discussion.

T. Anagnos, M. Trappen, B. C. K. Tiong, T. Feger, S. Yerolatsitis, R. J. Harris, J. Lozi, N. Jovanovic, T. A. Birks, S. Vievard, O. Guyon, I. Gris-Sánchez, S. G. Leon-Saval, B. Norris, S. Y. Haffert, P. Hottinger, M. Blaicher, Y. Xu, C. H. Betters, C. Koos, D. W. Coutts, C. Schwab, and A. Quirrenbach. 3D-M3: High-spatial-resolution spectroscopy with extreme AO and 3D-printed micro-lenslets. *Applied Optics*, 60(19): D108, 2021. ISSN 1559-128X. doi: 10.1364/ao.420855

Haffert et al. (2020)

Contributions: Setting up and supporting laboratory measurements.

S. Y. Haffert, R. J. Harris, A. Zanutta, F. A. Pike, A. Bianco, E. Redaelli, A. Benoît, D. G. MacLachlan, C. A. Ross, I. Gris-Sánchez, M. D. Trappen, Y. Xu, M. Blaicher, P. Maier, G. Riva, B. Siquin, C. Kulcsár, N. A. Bharmal, E. Gendron, L. Staykov, T. J. Morris, S. Barboza, N. Muench, L. Bardou, L. Prengère, H.-F. Raynaud, P. Hottinger, T. Anagnos, J. Osborn, C. Koos, R. R. Thomson, T. A. Birks, I. A. G. Snellen, and C. U. Keller. Diffraction-limited integral-field spectroscopy for extreme adaptive optics systems with the multicore fiber-fed integral-field unit. *Journal of Astronomical Telescopes, Instruments, and Systems*, 6(04):1–55, Dec. 2020. ISSN 2329-4124. doi: 10.1117/1.JATIS.6.4.045007

Jovanovic et al. (2023, under review)

Lead author of Sec. 2 by Philipp Hottinger, Olivier Guyon, and Rebecca Jenson-Clem: Symbiosis Between Adaptive Optics and Photonic Components: the Path to Fully Integrated Instruments

N. Jovanovic, P. Gatkine, N. Anugu, R. Amezcua-Correa, R. B. Thakur, C. Beichman, C. Bender, J.-P. Berger, A. Bigioli, J. Bland-Hawthorn, G. Bourdarot, C. M. Bradford, R. Broeke, J. Bryant, K. Bundy, R. Cheriton, N. Cvetojevic, M. Diab, S. A. Diddams, A. N. Dinkelaker, J. Duis, S. Eikenberry, S. Ellis, A. Endo, D. F. Figer, M. Fitzgerald, I. Gris-Sanchez, S. Gross, L. Grossard, O. Guyon, S. Y. Haffert, S. Halverson, R. J. Harris, J. He, T. Herr, P. Hottinger, E. Huby, M. Ireland, R. Jenson-Clem, J. Jewell, L. Jocou, S. Kraus, L. Labadie, S. Lacour, R. Laugier, K. Lawniczuk, J. Lin, S. Leifer, S. Leon-Saval, G. Martin, F. Martinache, M.-A. Martinod, B. A. Mazin, S. Minardi, J. D. Monnier, R. Moreira, D. Mourard, A. S. Nayak, B. Norris, E. Obrzud, K. Perrot, F. Reynaud, S. Sallum, D. Schiminovich, C. Schwab, E. Serbayn, S. Soliman, A. Stoll, L. Tang, P. Tuthill, K. Vahala, G. Vasisht, S. Veilleux, A. B. Walter, E. J. Wollack, Y. Xn, Z. Yang, S. Yerolatsitis, Y. Zhang, and C.-L. Zou. 2023 Astrophotonics Roadmap: Pathways to realizing multi-functional integrated astrophotonic instruments. *J. Phys. Photonics*, 2023, under review

Acknowledgments

Personal appreciation

First of all, I want to thank my wife Karo and my son Gabriel for their support over the years. Thank you for being there for me and giving me a good place to come home to. I want to thank my parents, but also my entire family and my family-in-law for supporting all my duties and helping me spend countless hours on the road, in the lab, traveling, and at various desks.

Thank you, Rob, for your scientific guidance and unlimited help over the past years, and all the fruitful and fun discussions about optics, photonics, and life. Without your hard work, help, and dedication, this project would not have been possible, thanks for sticking around until the end! I also want to thank you for bringing in Caroline. And thank you, Caroline, for giving my writing a final push and being the tutor I needed at that moment. I would like to thank Andreas Quirrenbach for his long-lasting support, patience, and continued financial backing.

I want to thank Theo for being a great Ph.D. brother and for all the help over the years. I will always cherish the glorious times in the Astrophotonics group under our great leader. I want to thank all the students at LSW, a community bound to help and support each other. I want to thank all the alumni Ph.D. students that have formed such a close group. But I want to thank the current Ph.D. students, in particular, coming closer together to support each other. Thank you Sepideh and Vera for the joint struggle and thank you S.M.A.R.T. meeting team, Emily and Dane, for the fight for productive work. I also want to thank my fellow Ph.D. fighters outside astronomy, namely Manu and Lukas. I want to thank my coaching group for guidance and help to figure out how to work properly.

I want to thank everybody that has helped with this thesis through valuable feedback. First of all Rob and Caroline for guiding me, but also Theo and Felix in particular for the large amount of proof reading. Additionally, I want to thank Andreas Quirrenbach for the structural discussions and Paul, Walter and Jochen for further feedback on various aspects of this work.

Project collaboration

I want to thank everyone who has been involved in the MLR-TT sensor project, as this has been a joint effort of an international collaboration.

Rob has been my supervisor helping and initiating project management. He was a great help in all practical design and application choices, providing valuable feedback with fundamental theoretical and practical knowledge. Furthermore, he has provided

support to many practical aspects including laboratory measurements, system integration, on-sky setup, and on-sky testing. Theo has helped with various discussions both on the design of the system and with the analysis of the data. The whole project was carried out in the Exoplanet research group at Landessternwarte (LSW), under the leadership of A. Quirrenbach, which focuses on radial-velocity detection of exosolar planets, provided the infrastructure and scientific context.

I want to thank the iLocator team for all their support, their hospitality at Notre Dame for integration and laboratory measurements, and for welcoming us at their instrument at LBT. Jonathan Crass is the lead developer of the iLocator spectrograph and has overseen the integration with the instrument, as well as communication and integration with the overall telescope, and contributing significantly to on-sky data analysis and writing. He has led the on-sky observations, responsible for communication with the telescope, controlled the iLocator instrument, and took the according measurements. Andrew Bechter and Brian Sands have both been heavily involved in various technical aspects of integration with iLocator. Andrew has overseen optical compatibility, vibration, and SMF-coupling characterization of the instrument itself, while Brian Sands has been responsible for electrical interfaces and control integration. I also want to thank Barnaby Norris for his work and insights on using machine learning (ML) for tip-tilt reconstruction.

Rob Harris and Philipp-Immanuel Dietrich have developed the initial MLA sensor concept (Dietrich et al., 2017). Philipp-Immanuel Dietrich has led the manufacturing and supported the optical design process. Together with Matthias Blaicher and under the lead of Christian Koos, they developed the necessary manufacturing procedure that was used to print the lenses themselves.

Tim Morris has been leading in advising both the setup and the analysis of the control system, and Ali Basden and Nazim Bharmal have developed and helped with setting up and integrating the Durham Adaptive Optics Real-Time Controller (DARC) software.

Thanks to Jochen Heidt for assisting and coordinating various parts of the observations and Jennifer Power for leading the AO control at Large Binocular Telescope Interferometer (LBTI) both for daytime setup and testing, as well as nighttime observations.

The laboratory measurements in Heidelberg have been supported both with advice and help in setting up and verifying the optical system by Philip Neureuther and Martin Glück at the Königstuhl Observatory Opto-Mechatronics Laboratory (KOOL) under the leadership of Jörg-Uwe Pott (Max Planck Institute for Astronomy, Heidelberg), Oliver Sawodny (Institute for System Dynamics Stuttgart) and Andreas Quirrenbach (Landessternwarte, Heidelberg). Last but not least, I would like to thank Lutz for his help with mechanical manufacturing.

Third-party support

This work has been supported by the Deutsche Forschungsgemeinschaft (DFG) through project 326946494, 'Novel Astronomical Instrumentation through photonic Reformatting'. This Ph.D. project was carried out within and supported by International Max Planck Research School for Astronomy and Cosmic Physics at the University of Heidel-

berg (IMPRS-HD) and Heidelberg Graduate School for Physics (HGSFP).

This thesis made use of many open-source scientific software, including, but not limited to, HCIPy, an open-source object-oriented framework written in Python for performing end-to-end simulations of high-contrast imaging instruments (Por et al., 2018), Astropy, a community-developed core Python package for Astronomy (The Astropy Collaboration et al., 2013, 2018), Numpy (Harris et al., 2020), and Matplotlib (Hunter, 2007).

Acronyms

List of used acronyms (selection).

AO adaptive optics

CoM center-of-mass

DARC Durham Adaptive Optics Real-Time Controller

DC dark current

DFT discrete Fourier transform

DM deformable mirror

EM electro-magnetic

ELT extremely large telescope

ExAO extreme adaptive optics

FoV field-of-view

FRD focal ratio degradation

IFU integral-field unit

IR infrared

ISYS Institute for System Dynamics Stuttgart

KIT Karlsruhe Institute for Technology

KOOL Königstuhl Observatory Opto-Mechatronics Laboratory

LBT Large Binocular Telescope

LGS laser guide star

LQG linear-quadratic-Gaussian

LSF line spread function

LSW Landessternwarte

MCF multi-core fiber

MFD mode-field diameter
ML machine learning
MLA micro-lens array
MLR micro-lens ring
MLR-TT sensor micro-lens ring tip-tilt sensor
MMF multi-mode fiber
MO multi object
MPIA Max Planck Institute for Astronomy
NA numerical aperture
NCPA non-common path aberration
NIR near-infrared
NGS natural guide star
PIAA phase-induced amplitude apodization
PL photonic lantern
PSD power spectral density
PSF point spread function
RON read-out noise
RV radial velocity
SMF single-mode fiber
SNR signal-to-noise ratio
SR Strehl ratio
WFS wavefront sensor

List of Figures

1.1	Sensitivity of SMF-coupling depending on tip or tilt. <i>(Reprinted from Hottinger et al., 2021)</i>	13
1.2	Overview of the micro-lens ring tip-tilt sensor (MLR-TT). <i>(Reprinted from Hottinger et al., 2021)</i>	14
2.1	Diffraction from a circular aperture resulting in an Airy pattern in focus. Left panel: normalized intensity of Airy pattern; center panel: logarithmic scale thereof; right panel: cross-section of normalized intensity.	19
2.2	Cross section of the diffraction pattern with different sizes of the secondary mirror, labeled by obscuration ratio $\alpha = D_{\text{obsc.}}/D$ between the diameter of the obscuring (secondary) mirror $D_{\text{obsc.}}$ and the primary mirror D	20
2.3	Zernike polynomials in Noll indexing order. Left panels: Phase of the wavefront in the pupil plane; right panels: Respective diffraction pattern as seen in the intensity of the light in the focal plane. Both phase and intensity are normalized to the corresponding maximum value, $Z = 1$ for each aberration.	23
2.4	Light rays coupling to a fiber according to the geometrical ray model. Light rays (red) are internally reflected at the boundary between the core (cyan) and cladding (blue) as the larger refractive index of the core n_1 is larger than the cladding's refractive index n_2 . If the incident angle of a light ray is larger than the acceptance angle θ , the light is not confined to the core but refracted into the cladding (dashed red line). The image represents a typical multi-mode fiber (MMF) with a core diameter of $d = 50 \mu\text{m}$, a cladding diameter of $125 \mu\text{m}$ and a protective buffer with a diameter of $250 \mu\text{m}$	24
2.5	Gaussian beam waist shape and the respective parameters. <i>Source:</i> GaussianBeamWaist (https://commons.wikimedia.org/wiki/File:GaussianBeamWaist.svg) by Rodolfo Hermans, DrBob used under CC BY-SA 3.0 (https://creativecommons.org/licenses/by-sa/3.0/deed.en) / modified parameters.	26
2.6	Cross section of the Airy disk (blue) and the best Gaussian fit (orange)	28
2.7	SMF coupling as a function of RMS wavefront distortion denoted by the coefficient a_i of a single Zernike mode. Shown for simulations of different modes (markers) and the corresponding analytical solution (dotted line). <i>(Reprinted from Ruilier and Cassaing, 2001)</i>	29

List of Figures

3.1	Schematic representation of the LBT in its prime focus usage (left) and in its Gregorian configuration (right). The light enters the telescope from the top and is then reflected by the large primary mirror either directly onto a camera or with an additional secondary mirror extending its focal length. <i>(Reprinted from Rodriguez et al., 2020)</i>	32
3.2	Left: PSD of LBT as measured by iLocater, with AO correction considering 300 modes; right: normalized cumulative representation. <i>(Reprinted from Bechter et al., 2019)</i>	36
3.3	<i>Schematic representation</i> of telescope and spectrograph. An angular extended source (physically extended or by atmospheric Seeing, green/blue dashed lines) is coupled into a slit or fiber and from there projected onto a grating. The spectrally dispersed slit image (purple/yellow solid lines) or fiber output is then imaged on the detector.	39
3.4	Fiber far-field output as measured in the laboratory. Left panel: MMF output (slightly out of focus); right panel: SMF output (magnified). . . .	40
3.5	Overview of conventional AO systems, potential photonic counterparts and additions, as well as integrated instrumental concepts. Individual components: Thermo-coupled phase shifter (Harris et al., 2014), sparse aperture masking (SAM) interferometry fringe tracker WFS (Deo et al., 2022), photonic lantern WFS (Norris et al., 2020a), photonic lantern with reformatter (Pike et al., 2020), GLINT nulling interferometer (Norris et al., 2020b), Gravity beam combiner (GRAVITY Collaboration et al., 2017), microlens-ring tip-tilt (MLR-TT) sensor (Hottinger et al., 2021), integrated photonic instrument illustration by Phil Saunders (Norris and Bland-hawthorn, 2019). <i>(Reprinted from Jovanovic et al., 2023, under review)</i>	42
4.1	Simulated single-mode fiber (SMF) coupling for a mode-field diameter (MFD) of $5.8\ \mu\text{m}$ ($1/e^2$ intensity). Image (a) shows the cross section of the intensity profile for both the fundamental mode of a single-mode fiber (blue) and a diffraction limited point spread function optimized for maximum coupling efficiency into that SMF (red). The green dashed line indicates the $1/e^2$ -intensity (13% of the maximum). Image (b) shows the coupling efficiency if the incoming beam is gradually misaligned with respect to the fiber by shifting the centroid of the point spread function (PSF), resulting in a rapid decrease in coupling efficiency with position. <i>(Reprinted from Hottinger et al., 2018)</i>	49
4.2	Scatter plot of the location of the PSF centroid for each exposure and the corresponding distributions. The wavelength range of 700 nm to 970 nm was imaged by the iLocater front-end prototype as described in Bechter et al. (2016). The diameter of the diffraction limited PSF is ~ 60 mas. <i>(Reprinted from Hottinger et al., 2018)</i>	50

4.3 Averaged Point Spread Function from the LBT, with **(a)** no tip-tilt compensation and **(b)** with tip-tilt compensation calculated by holding the center of a fitted Gaussian constant. Both images have logarithmic intensity scaling and are normalized to the highest pixel value. The red circle denotes the Airy disk diameter at 850 nm, indicating that with vibrational compensation the coupling will be higher. It can also be seen from b) that aberrations in the system need to be compensated for.
(Reprinted from Hottinger et al., 2018) 51

4.4 Design model of a micro-lens array (MLA) tip-tilt sensor for the front-end prototype of the iLocator spectrograph. The MLA is printed on top of a fiber bundle made of a central single-mode fiber (SMF) (not visible) and six surrounding multi-mode fibers (MMFs) (only fiber cores shown). While the central optical path to the SMF is unobscured, off-centered light will be refracted by the MLA to be coupled into the surrounding sensing MMFs. The pitch between the fiber cores is 125 μm . Diameter and height of the MLA are 300 μm and 400 μm , respectively.
(Reprinted from Hottinger et al., 2018) 52

4.5 Cross section of the micro-lens array (MLA) tip-tilt sensor with incoming beam illustrating the working principle of the device. The color of the rays indicate which fiber the light is coupled into: the central single-mode fiber (SMF) feeding the spectrograph (purple, number of rays does not correspond to coupling efficiency) and the outer sensing multi-mode fibers (MMFs) (red, violet, orange, blue). Rays that are refracted by the MLA and are not coupled into any fiber are not illustrated. If the beam is perfectly aligned **(a)**, most of the light is coupled into the central SMF with some of the rest coupled into the outer sensing MMFs. As the beam is decentered by 2 μm **(b)**, coupling efficiency into the SMF decreases but is still significant while the sensing signal in the outer MMFs increases. For large misalignments of 10 μm **(c)** and 50 μm **(d)** no light is coupled into the central SMF but successively more light is coupled into the sensing MMFs illustrating the wide dynamical range the tip-tilt sensor covers.
(Reprinted from Hottinger et al., 2018) 53

4.6 Modeled coupling into the SMF (red line) and into the sensing MMF (blue line) for an incoming beam moving from a perfectly aligned position along an axis to this sensing fiber.
(Reprinted from Hottinger et al., 2018) 54

4.7 Off-axis performance of the MLA tip-tilt sensor. Modeled coupling for one sensing MMF for an incoming beam moving from an aligned position outwards. This is illustrated in the image **(a)**: The rightmost fiber is sensed while the beam is decentered from the center in different directions indicated by the colored arrows. The different lines in image **(b)** correspond to these different directions of this tip-tilt motion, ranging from 0° (blue) to 60° (green) in steps of 6° and in reference to the sensing MMF.
(Reprinted from Hottinger et al., 2018) 55

List of Figures

4.8 Sensing signal for each MMF as the incoming beam moves from an aligned position outwards as illustrated in image **(a)** (two fibers are not shown). Image **(b)** shows the signal as function of the misalignment. The signal of the three fibers in direction of the beam increases linearly while the signal on the opposite fibers decreases linearly.
(Reprinted from Hottinger et al., 2018) 56

4.9 Tip-tilt sensor performance for different central apertures ranging from 100 μm (blue) to 130 μm (green) in diameter. Dashed lines correspond to central SMF coupling and solid lines to sensing MMF coupling. For larger central apertures, the maximum coupling efficiency into the SMF increases but the sensing signal decreases. This trade-off between maximum coupling and sensing sensitivity needs to be evaluated and chosen to fit the requirements of the system.
(Reprinted from Hottinger et al., 2018) 57

4.10 Design layout of the Königstuhl Observatory Opto-Mechatronics Laboratory (KOOL). This adaptive optics (AO) testbed allows simulation and correction of LBT vibrations with two tip-tilt mirrors and higher order aberrations with an ALPAO deformable mirror (DM). A HeNe Source (632 nm) is used in the main setup including the wavefront sensor (WFS) (purple) and an imaging arm (dark blue). A near-infrared (NIR) (1.31 μm) source feeds both a fiber coupling arm (light blue) and a separate imaging arm (violet). Both sources are SMF-fed.
(Reprinted from Hottinger et al., 2018) 58

4.11 Prototype MLA (green) printed on top of a multi-core fiber (MCF) (blue) consisting of seven single-mode fibers (SMFs) (black) as introduced by Dietrich et al. (2017). Image **(a)** shows a 3D model of the design. Image **(b)** shows the single-mode fiber (SMF) coupling efficiency normalized to the maximum coupling efficiency for both the the central fiber (red line) and the outer sensing fiber (dashed orange line). Note the different sensing response in comparison to the design introduced in this work as plotted in Fig. 4.6.
(Reprinted from Hottinger et al., 2018, adapted from Dietrich et al., 2017) 62

5.1 Modeled ray propagation through the micro-lens ring (MLR) for an incoming beam that is **(a)** aligned and offset by **(b)** 5 μm and **(b)** 10 μm , respectively. In the platescale of iLocater frontend (at 1 μm), the diffraction limit $1.22\lambda/D \sim 60\text{mas}$ corresponds to $\sim 3.9\mu\text{m}$ offset. Please note that the number of rays propagating to the tip of the single-mode fiber (SMF) does not correspond to the coupling efficiency.
(Reprinted from Hottinger et al., 2019) 68

5.2 DSLR photograph of micro-lens ring (MLR). The lens stands around 380 μm tall and around 400 μm in diameter.
(Reprinted from Hottinger et al., 2019) 69

5.3 Fiber response in respect to centroid position for both modeled throughput in the ray tracing software *Zemax* (a) and for measured throughput at the iLocater fronted prototype in the lab (b). The vertical gray line denotes the diffraction limit at $\lambda \approx 1\mu\text{m}$. SMF coupling (light blue markers, left y-axis) MMFs coupling (right y-axis) for all six sensing fibers, from same direction as the misalignment (orange marker, corresponding to very right fiber with green rays in Fig. 5.1), the two adjacent fibers (green, pink, corresponding to second fiber from right with red rays on Fig. 5.1), to the three fibers on the opposite direction (brown, red, violet, corresponding to two left fibers with pink rays on Fig. 5.1). All MMFs have differing throughputs, which are normalized in this graph for illustration.
(Reprinted from Hottinger et al., 2019) 70

5.4 Power spectral density (PSD) of the position in x-direction of introduced vibrations as seen on a separate detector that images the PSF (blue) and recovered by the fiber based tip-tilt sensor presented in this work (orange).
(Reprinted from Hottinger et al., 2019) 72

6.1 Numerically calculated theoretical normalized coupling efficiency assuming an optimally coupled diffraction-limited PSF with additional residual tip-tilt variation, plotted in units of λ/D . The measured RMS residuals at the iLocater focal plane are also indicated, without beam stabilization at $0.61 \lambda/D$ resulting in a theoretical reduction by 44% (red line), and with additional stabilization with a quad-cell detector improving tip-tilt stability to $0.39 \lambda/D$, leading to a tip-tilt induced coupling loss of 24% (green line) (Crass et al., 2020).
(Reprinted from Hottinger et al., 2021) 79

6.2 Overview of the micro-lens ring tip-tilt sensor (MLR-TT). (a) Schematics of the setup. The starlight (red) is coupled into the SMF (dark blue), while some light at the edges of the beam is clipped and refracted (orange beam) by the MLR (light blue) to be coupled into the sensing MMFs (dark green). The fibers are embedded in a fiber bundle that fans out into a single SMF which then feeds the starlight into a science instrument and the six MMFs that are reformatted into a linear array mounted in an SMA connector. The sensing fibers are then re-imaged and the detected flux is used to reconstruct the centroid position of the telescope beam. (b) Microscope image of the MLR on the fiber bundle face, (c) microscope image of back-illuminated fiber bundle, (d) sensing fiber output at the fiber connector, and (e) re-arranged detector signal for visual examination of the reconstruction algorithm with the green cross indicating the centroid position.
(Reprinted from Hottinger et al., 2021) 81

List of Figures

6.3 Modeled (solid lines) and measured (crosses) sensor response as function of centroid offset. **Top panel:** The coupling efficiency of the science SMF. **Middle panel:** The response of the six sensing MMF as function of beam offset. **Bottom panel:** MLR-TT sensor signal summed over all six MMFs. 84

6.4 Illustration of the reconstruction routine with simulated noise. **Left panel:** Simulated detector image showing the six MMFs (numbered 1-6 in orange) along with the reconstructed centroid of the PSF (red cross). **Right panel:** A graphical illustration of the reconstruction routine. Here the six fiber fluxes (gray, numbered 1-6 in orange) are ordered by their azimuthal coordinate and a sine function with angular period of 2π is fitted, giving the angle, amplitude and offset of the centroid. *(Reprinted from Hottinger et al., 2021)* 85

6.5 Optical path of the experimental setup with the iLocator acquisition camera at LBT (sizes are not to scale). (a) The collimated AO corrected beam from LBTI is steered by a fast tip-tilt mirror (b). A short-pass dichroic (c) transmits wavelengths between 920 and 950 nm to be imaged by the Andor focal plane camera (d). The science light is reflected by the long-pass dichroic mirror (e) and focused into the MLR-TT sensor (f) and SMF. Light between 1.34-1.76 μm is transmitted and imaged on the quad-cell (g) that can be used in closed-loop to correct for tip-tilt vibrations. *(Reprinted from Hottinger et al., 2021)* 87

6.6 Three scatter plots showing the on-sky calibration routine of target HIP7981. Shown are (a) the reference centroid position measured with the Andor focal plane camera, (b) the MLR-TT reconstructed raw centroid position reconstructed from the MLR-TT and (c) the calibrated MLR-TT centroid position (see Tab. 6.2). Initially the PSF is centered, then a circular motion is introduced on the fast tip-tilt mirror. This movement is not calibrated in λ/D and produces an elliptical shape in the focal plane due to the angle of the tip-tilt mirror. The introduced figure also features a central accumulation from before and after the circular motion, as well as an introduced step position seen as a separate patch to the top right of the circle. *(Reprinted from Hottinger et al., 2021)* 89

6.7 Closed loop transfer function when stabilizing the beam with the MLR-TT sensor for datasets HIP28634/4 (closed loop) and HIP28634/5. Below ~ 10 Hz, the MLR-TT sensor (blue, yellow) detects a different frequency rejection than the Andor reference (green, red), whilst above 10 Hz the transfer functions agree well. *(Reprinted from Hottinger et al., 2021)* 90

6.8 Sensor reconstruction accuracy shown graphically. **Top panels:** Time series of (Left) the centroid position measured by the Andor focal plane camera, (Center) the position reconstructed with the MLR-TT and (Right) the error in the reconstruction by taking the difference between the former two datasets. **Bottom panels:** Time series graphs of the same dataset for: (Top) Comparison of the centroid x -position for (tip, left) and y -position (tilt, right) of Andor reference (blue) and MLR-TT (red), and (Bottom) the corresponding reconstruction error (green) from their difference. *(Reprinted from Hottinger et al., 2021)* 91

6.9 Power spectral density (PSD) for HD12354/1 of the signal shown in Fig. 6.8. (Top) PSD of centroid x -position (tip, left) and y -position (tilt, right) of MLR-TT (red) compared to the Andor reference (blue), (Bottom) the PSD of the corresponding reconstruction error (green) for tip and tilt. Most of the vibrational power lies between 10 and 20 Hz, whilst most of the reconstruction error is in the low frequencies (< 10 Hz). *(Reprinted from Hottinger et al., 2021)* 92

6.10 On-sky sensor performance. **Main panel:** Reconstruction accuracy as a function of estimated Strehl ratio (SR) for these datasets. Cross marks in the main plot represent the mean and error for each dataset, while the circles in the subplots correspond to subsets with different estimated SRs, with the size of the circle representing the number of frames in each set. The dashed lines show the fitting error. **Top panels:** The centroid reconstruction error scatter plot for each analyzed dataset. *(Reprinted from Hottinger et al., 2021)* 93

6.11 Synthetic MLR-TT sensor performance derived from AO simulations, plotted to be comparable to Fig. 6.10. **Main panel:** Reconstruction accuracy as a function of Strehl ratio (SR) for AO simulations with varying residual aberration strength labeled with their RMS wavefront error. Crosses represent overall mean and error for each data set, while the circles correspond to subsets binned by SR, with the size of the circle representing the number of frames in each set. The dashed lines show the fitting error. **Top panels:** Centroid reconstruction error scatter for the individual datasets. *(Reprinted from Hottinger et al., 2021)* 94

7.1 Block diagram of the telescope system setup composed of the AO system and the MLR-TT Sensor system. The iLocater’s unmodified SMF coupling and its native quad-cell tip-tilt sensing is not shown. 100

7.2	Reconstruction of tip/tilt with machine learning (ML) using neural networks (red dots). Performed on on-sky measurements (HD12354/1) including noise and residual AO aberrations. After training, the algorithm is able to achieve an accuracy of $0.175 \lambda/D$ (RMS error) in comparison with centroid position as measured with a Gaussian fit on the Andor focal plane camera (blue lines). This is a $\sim 8\%$ improvement compared to $0.195 \lambda/D$ on the same dataset by the reconstruction algorithm presented in this work. <i>(Courtesy of Barnaby Norris, private communication)</i>	105
7.3	Reconstruction of 5 Zernike modes with machine learning (ML) using neural networks (red dots). Performed on simulated MLR-TT responses with 5 uniformly random coefficients between -0.7 and 0.7 without additional aberrations or noise. The ML algorithm is able to reconstruct the introduced coefficients (blue lines) with an RMS error of 0.0582 . <i>(Courtesy of Barnaby Norris, private communication)</i>	106
7.4	Top panel: Latency of MLR-TT sensor system on-sky in ms as a function of framerate (1/s). Bottom panels: Step response as measured by the sensor. The centroid x - and y -position (black/red) as measured after introducing an offset in one of the axes of the tip-tilt mirror.	108
7.5	Power spectral density (PSD) of tip and tilt disturbance as measured by the Andor focal plane camera on-sky, without additional correction. Target HIP28634/5. Left panel: logarithmic scale PSD; right panel: relative cumulative PSD.	110
7.6	Modeled theoretical rejection of an integrator. Without measurement noise and running at a correction frequency of 500 Hz and with a latency of 2 frames. Top: PSD of random noise signal; center: PSD of corrected signal; bottom: rejection transfer function.	111
7.7	PSD of residual tip (x -Axis, left column) and tilt (y -Axis, right column) both as measured by the Andor focal plane camera (blue) and the MLR-TT sensor (orange). Compared between open-loop measurements (top) without any corrections, closed-loop (gain $\alpha = 0.4$) with the MLR-TT sensor system (center), and the corresponding rejection transfer function (bottom). Target HIP2981.	112
7.8	Comparison of different modeling approaches of the MLR-TT sensor response (solid lines) with the corresponding laboratory measurements (crosses). Left panel: geometric modeling (<i>adapted from Hottinger et al., 2019</i>); right panel: more accurate wave-optical simulation (<i>adapted from Hottinger et al., 2021</i>).	114

Bibliography

- J. Allington-Smith. Spectroscopy. In R. Foy and F. C. Foy, editors, *Optics in Astrophysics*, pages 155–180. Springer, Dordrecht, 2006. ISBN 978-1-4020-3435-0. doi: 10.1007/1-4020-3437-7_12.
- T. Anagnos, M. Trappen, B. C. K. Tiong, T. Feger, S. Yerolatsitis, R. J. Harris, J. Lozi, N. Jovanovic, T. A. Birks, S. Vievard, O. Guyon, I. Gris-Sánchez, S. G. Leon-Saval, B. Norris, S. Y. Haffert, P. Hottinger, M. Blaicher, Y. Xu, C. H. Betters, C. Koos, D. W. Coutts, C. Schwab, and A. Quirrenbach. 3D-M3: High-spatial-resolution spectroscopy with extreme AO and 3D-printed micro-lenslets. *Applied Optics*, 60(19): D108, 2021. ISSN 1559-128X. doi: 10.1364/ao.420855.
- J. R. P. Angel. Ground-based imaging of extrasolar planets using adaptive optics. *Nature*, 368(6468):203–207, Mar. 1994. ISSN 0028-0836. doi: 10.1038/368203a0.
- A. Basden, D. Geng, R. Myers, and E. Younger. Durham adaptive optics real-time controller. *Applied Optics*, 49(32):6354, Nov. 2010. ISSN 0003-6935. doi: 10.1364/AO.49.006354.
- A. G. Basden and R. M. Myers. The Durham adaptive optics real-time controller: Capability and Extremely Large Telescope suitability. *Monthly Notices of the Royal Astronomical Society*, 424(2):1483–1494, Aug. 2012. ISSN 00358711. doi: 10.1111/j.1365-2966.2012.21342.x.
- A. Bechter, J. Crass, R. Ketterer, J. R. Crepp, D. King, B. Zhao, R. Reynolds, P. Hinz, J. Brooks, and E. Bechter. Design of the iLocator acquisition camera demonstration system. In S. Shaklan, editor, *Proc. of SPIE 9605*, volume 9605, page 96051U, Sept. 2015. ISBN 978-1-62841-771-5. doi: 10.1117/12.2188426.
- A. Bechter, J. Crass, R. Ketterer, J. R. Crepp, R. O. Reynolds, E. Bechter, P. Hinz, F. Pedichini, M. Foley, E. Runburg, E. E. Onuma, S. Gaudi, G. Micela, I. Pagano, and C. E. Woodward. On-sky single-mode fiber coupling measurements at the Large Binocular Telescope. In E. Marchetti, L. M. Close, and J.-P. Véran, editors, *Adaptive Optics Systems V*, volume 9909, page 99092X, July 2016. ISBN 978-1-5106-0197-0. doi: 10.1117/12.2233153.
- A. J. Bechter, J. Crass, J. Tesch, J. R. Crepp, and E. B. Bechter. Characterization of Single-mode Fiber Coupling at the Large Binocular Telescope. *Publications of the Astronomical Society of the Pacific*, 132(1007):015001, Jan. 2019. ISSN 0004-6280. doi: 10.1088/1538-3873/ab42cb.

Bibliography

- J.-L. Beuzit, M. Feldt, K. Dohlen, D. Mouillet, P. Puget, F. Wildi, L. Abe, J. Antichi, A. Baruffolo, P. Baudoz, A. Boccaletti, M. Carbillet, J. Charton, R. Claudi, M. Downing, C. Fabron, P. Feautrier, E. Fedrigo, T. Fusco, J.-L. Gach, R. Gratton, T. Henning, N. Hubin, F. Joos, M. Kasper, M. Langlois, R. Lenzen, C. Moutou, A. Pavlov, C. Petit, J. Pragt, P. Rabou, F. Rigal, R. Roelfsema, G. Rousset, M. Saisse, H.-M. Schmid, E. Stadler, C. Thalmann, M. Turatto, S. Udry, F. Vakili, and R. Waters. SPHERE: A 'Planet Finder' instrument for the VLT. In I. S. McLean and M. M. Casali, editors, *Ground-Based and Airborne Instrumentation for Astronomy II*, volume 701418, page 701418, July 2008. ISBN 978-0-8194-7224-3. doi: 10.1117/12.790120.
- J. Bland-Hawthorn and P. Kern. Astrophotonics: A new era for astronomical instruments. *Optics Express*, 17(3):1880, Feb. 2009. ISSN 1094-4087. doi: 10.1364/oe.17.001880.
- J. Bland-Hawthorn, J. Bryant, G. Robertson, P. Gillingham, J. O'Byrne, G. Cecil, R. Haynes, S. Croom, S. Ellis, M. Maack, P. Skovgaard, D. Noordegraaf, J. O'Byrne, G. Cecil, R. Haynes, S. Croom, S. Ellis, M. Maack, P. Skovgaard, and D. Noordegraf. Hexabundles: Imaging fiber arrays for low-light astronomical applications. *Optics Express*, 19(3):2649, Jan. 2011. ISSN 1094-4087. doi: 10.1364/OE.19.002649.
- M. Brix, V. Naranjo, U. Beckmann, R. Bertram, T. Bertram, J. Brynnel, S. Egner, W. Gaessler, T. M. Herbst, M. Kuerster, R. R. Rohloff, S. Rost, and J. Schmidt. Vibration measurements at the Large Binocular Telescope (LBT). *Ground-based and Airborne Telescopes II*, 7012(July 2008):70122J, Aug. 2008. ISSN 0277786X. doi: 10.1117/12.787533.
- M. Corrigan, R. J. Harris, R. R. Thomson, D. G. MacLachlan, J. Allington-Smith, R. Myers, and T. Morris. Wavefront sensing using a photonic lantern. page 990969, Aug. 2016. doi: 10.1117/12.2230568.
- V. Coudé du Foresto. Integrated Optics in Astronomical Interferometry. *Symposium - International Astronomical Union*, 158(Gloge):261–271, 1994. ISSN 0074-1809. doi: 10.1017/s0074180900107715.
- J. Crass, A. Bechter, B. Sands, D. King, R. Ketterer, M. Engstrom, R. Hamper, D. Kopon, J. Smous, J. R. Crepp, M. Montoya, O. Durney, D. Cavalieri, R. Reynolds, M. Vansickle, E. Onuma, J. Thomes, S. Mullin, K. Wallace, E. Bechter, A. Vaz, J. Power, G. Rahmer, S. Ertel, C. Shelton, K. Wallace, E. Bechter, A. Vaz, J. Power, G. Rahmer, and S. Ertel. Final Design and On-Sky Testing of the iLocator SX Acquisition Camera: Broadband Single-Mode Fiber Coupling. *Monthly Notices of the Royal Astronomical Society*, 18(October):1–18, 2020. ISSN 0035-8711. doi: 10.1093/mnras/staa3355.
- J. R. Crepp, J. Crass, D. King, A. Bechter, E. Bechter, R. Ketterer, R. Reynolds, P. Hinz, D. Kopon, D. Cavalieri, L. Fantano, C. Koca, E. Onuma, K. Stapelfeldt, J. Thomes, S. Wall, S. Macenka, J. McGuire, R. Korniski, L. Zugby, J. Eisner, B. S.

- Gaudi, F. Hearty, K. Kratter, M. Kuchner, G. Micela, M. Nelson, I. Pagano, A. Quirrenbach, C. Schwab, M. Skrutskie, A. Sozzetti, C. Woodward, and B. Zhao. iLocator: A diffraction-limited Doppler spectrometer for the Large Binocular Telescope. page 990819, Aug. 2016. ISBN 978-1-5106-0195-6. doi: 10.1117/12.2233135.
- N. Cvetojevic, N. Jovanovic, S. Gross, B. Norris, I. Spaleniak, C. Schwab, M. J. Withford, M. Ireland, P. Tuthill, O. Guyon, F. Martinache, and J. S. Lawrence. Modal noise in an integrated photonic lantern fed diffraction-limited spectrograph. *Optics Express*, 25(21):25546, Oct. 2017. ISSN 1094-4087. doi: 10.1364/OE.25.025546.
- N. Cvetojevic, E. Huby, G. Martin, S. Lacour, F. Marchis, J. Lozi, N. Jovanovic, S. Vievard, O. Guyon, L. Gauchet, G. Perrin, G. Duchêne, and T. Kotani. FIRST, the pupil-remapping fiber interferometer at Subaru telescope: Towards photonic beam-combination with phase control and on-sky commissioning results (Conference Presentation). In A. Mérand, M. J. Creech-Eakman, and P. G. Tuthill, editors, *Optical and Infrared Interferometry and Imaging VI*, page 9, Austin, United States, July 2018. SPIE. ISBN 978-1-5106-1955-5 978-1-5106-1956-2. doi: 10.1117/12.2313262.
- J.-R. Delorme, N. Jovanovic, D. Echeverri, D. Mawet, J. Kent Wallace, R. D. Bartos, S. Cetre, P. Wizinowich, S. Ragland, S. Lilley, E. Wetherell, G. Doppmann, J. J. Wang, E. C. Morris, J.-B. Ruffio, E. C. Martin, M. P. Fitzgerald, G. Ruane, T. Schofield, N. Suominen, B. Calvin, E. Wang, K. Magnone, C. Johnson, J. M. Sohn, R. A. López, C. Z. Bond, J. Pezzato, J. L. Sayson, M. Chun, and A. J. Skemer. Keck Planet Imager and Characterizer: A dedicated single-mode fiber injection unit for high-resolution exoplanet spectroscopy. *Journal of Astronomical Telescopes, Instruments, and Systems*, 7(03):035006, Aug. 2021. ISSN 23294221. doi: 10.1117/1.jatis.7.3.035006.
- V. Deo, S. Vievard, N. Cvetojevic, K. Ahn, E. Huby, O. Guyon, S. Lacour, J. Lozi, F. Martinache, B. Norris, N. Skaf, and P. G. Tuthill. Controlling petals using fringes: Discontinuous wavefront sensing through sparse aperture interferometry at Subaru/SCEXAO. In D. Schmidt, L. Schreiber, and E. Vernet, editors, *Adaptive Optics Systems VIII*, page 34. SPIE, Aug. 2022. ISBN 978-1-5106-5351-1. doi: 10.1117/12.2629865.
- P.-I. Dietrich, R. J. Harris, M. Blaicher, M. K. Corrigan, T. J. Morris, W. Freude, A. Quirrenbach, and C. Koos. Printed freeform lens arrays on multi-core fibers for highly efficient coupling in astrophotonic systems. *Optics Express*, 25(15):18288, July 2017. ISSN 1094-4087. doi: 10.1364/OE.25.018288.
- P.-I. Dietrich, M. Blaicher, I. Reuter, M. Billah, T. Hoose, A. Hofmann, C. Caer, R. Dangel, B. Offrein, U. Troppenz, M. Moehrle, W. Freude, and C. Koos. In situ 3D nanoprining of free-form coupling elements for hybrid photonic integration. *Nature Photonics*, 12(4):241–247, Apr. 2018. ISSN 1749-4885. doi: 10.1038/s41566-018-0133-4.

Bibliography

- G. Eisenstein and D. Vitello. Chemically etched conical microlenses for coupling single-mode lasers into single-mode fibers. *Applied Optics*, 21(19):3470, Oct. 1982. ISSN 0003-6935, 1539-4522. doi: 10.1364/AO.21.003470.
- S. Esposito, E. Marchetti, R. Ragazzoni, A. Baruffolo, J. Farinato, L. Fini, A. Ghedina, P. Ranfagni, and A. Riccardi. Laboratory characterization of an APD-based tip-tilt corrector. In R. K. Tyson and R. Q. Fugate, editors, *Proceedings of SPIE - The International Society for Optical Engineering*, volume 3126, page 378, Oct. 1997. doi: 10.1117/12.290159.
- S. Esposito, A. Riccardi, E. Pinna, A. Puglisi, F. Quirós-Pacheco, C. Arcidiacono, M. Xompero, R. Briguglio, G. Agapito, L. Busoni, L. Fini, J. Argomedo, A. Gherardi, G. Brusa, D. Miller, J. C. Guerra, P. Stefanini, and P. Salinari. Large Binocular Telescope Adaptive Optics System: New achievements and perspectives in adaptive optics. In R. K. Tyson and M. Hart, editors, *Astronomical Adaptive Optics Systems and Applications IV*, volume 814902, page 814902, Sept. 2011. ISBN 978-0-8194-8759-9. doi: 10.1117/12.898641.
- T. Feger, C. Bacigalupo, T. R. Bedding, J. Bento, D. W. Coutts, M. J. Ireland, Q. A. Parker, A. Rizzuto, and I. Spaleniak. RHEA: The ultra-compact replicable high-resolution exoplanet and Asteroseismology spectrograph. In S. K. Ramsay, I. S. McLean, and H. Takami, editors, *Ground-Based and Airborne Instrumentation for Astronomy V*, volume 9147, page 91477I, July 2014. doi: 10.1117/12.2055600.
- E. Gendron, F. Vidal, M. Brangier, T. Morris, Z. Hubert, A. Basden, G. Rousset, R. Myers, F. Chemla, A. Longmore, T. Butterley, N. Dipper, C. Dunlop, D. Geng, D. Gratadour, D. Henry, P. Laporte, N. Looker, D. Perret, A. Sevin, G. Talbot, and E. Younger. MOAO first on-sky demonstration with CANARY. *Astronomy & Astrophysics*, 529:L2, May 2011. ISSN 0004-6361. doi: 10.1051/0004-6361/201116658.
- S. Gillessen, F. Eisenhauer, S. Trippe, T. Alexander, R. Genzel, F. Martins, and T. Ott. MONITORING STELLAR ORBITS AROUND THE MASSIVE BLACK HOLE IN THE GALACTIC CENTER. *The Astrophysical Journal*, 692(2):1075, Feb. 2009. ISSN 0004-637X. doi: 10.1088/0004-637X/692/2/1075.
- S. Gillessen, F. Eisenhauer, G. Perrin, W. Brandner, C. Straubmeier, K. Perraut, A. Amorim, M. Schöller, C. Araujo-Hauck, H. Bartko, H. Baumeister, J.-P. J.-P. Berger, P. Carvas, F. Cassaing, F. Chapron, E. Choquet, Y. Clenet, C. Collin, A. Eckart, P. Fedou, S. Fischer, E. Gendron, R. Genzel, P. B. Gitton, F. Gonte, A. Gräter, P. Hagenauer, M. Haug, X. Haubois, T. Henning, S. Hippler, R. Hofmann, L. Jocou, S. Kellner, P. Kervella, R. Klein, N. Kudryavtseva, S. Lacour, V. Lapeyrere, W. Laun, P. Lena, R. Lenzen, J. Lima, D. Moratschke, D. Moch, T. Moulin, V. Naranjo, U. Neumann, A. Nolot, T. Paumard, O. Pfuhl, S. Rabien, J. R. Ramos, J. M. Rees, R.-R. Rohloff, D. Rouan, G. Rousset, A. Sevin, M. Thiel, K. Wagner, M. Wiest, S. Yazici, and D. Ziegler. GRAVITY: A four-telescope beam

- combiner instrument for the VLTI. *Proc. SPIE*, 7734(Optical and Infrared Interferometry II):77340Y–77340Y–20, July 2010. ISSN 0277786X. doi: 10.1117/12.856689.
- M. Glück, J.-U. Pott, and O. Sawodny. Investigations of an Accelerometer-based Disturbance Feedforward Control for Vibration Suppression in Adaptive Optics of Large Telescopes. *Publications of the Astronomical Society of the Pacific*, 129(976):65001, June 2017. ISSN 00046280. doi: 10.1088/1538-3873/aa632b.
- J. W. Goodman and E. G. Rawson. Statistics of modal noise in fibers: A case of constrained speckle. *Optics Letters*, 6(7):324–326, July 1981. ISSN 1539-4794. doi: 10.1364/OL.6.000324.
- M. Goodwin, S. Richards, J. Zheng, J. Lawrence, S. Leon-Saval, A. Argyros, B. Alcalde, S. Richards, J. Zheng, J. Lawrence, S. Leon-Saval, and A. Argyros. Miniaturized Shack-Hartmann wavefront sensors for starbugs. page 91514T, July 2014. doi: 10.1117/12.2055014.
- GRAVITY Collaboration, R. Abuter, M. Accardo, A. Amorim, N. Anugu, G. Ávila, N. Azouaoui, M. Benisty, J. P. Berger, N. Blind, H. Bonnet, P. Bourget, W. Brandner, R. Brast, A. Buron, L. Burtscher, F. Cassaing, F. Chapron, É. Choquet, Y. Clénet, C. Collin, V. Coudé du Foresto, W. de Wit, P. T. de Zeeuw, C. Deen, F. Delplancke-Ströbele, R. Dembet, F. Derie, J. Dexter, G. Duvert, M. Ebert, A. Eckart, F. Eisenhauer, M. Esselborn, P. Fédou, G. Finger, P. Garcia, C. E. Garcia Dabo, R. Garcia Lopez, E. Gendron, R. Genzel, S. Gillessen, F. Gonte, P. Gordo, M. Grould, U. Grözinger, S. Guieu, P. Haguenaue, O. Hans, X. Haubois, M. Haug, F. Haussmann, T. Henning, S. Hippler, M. Horrobin, A. Huber, Z. Hubert, N. Hubin, C. A. Hummel, G. Jakob, A. Janssen, L. Jochum, L. Jocou, A. Kaufer, S. Kellner, S. Kendrew, L. Kern, P. Kervella, M. Kiekebusch, R. Klein, Y. Kok, J. Kolb, M. Kulas, S. Lacour, V. Lapeyrère, B. Lazareff, J.-B. Le Bouquin, P. Lèna, R. Lenzen, S. Lévêque, M. Lippa, Y. Magnard, L. Mehrgan, M. Mellein, A. Mérand, J. Moreno-Ventas, T. Moulin, E. Müller, F. Müller, U. Neumann, S. Oberti, T. Ott, L. Pallanca, J. Panduro, L. Pasquini, T. Paumard, I. Percheron, K. Perraut, G. Perrin, A. Pflüger, O. Pfuhl, T. Phan Duc, P. M. Plewa, D. Popovic, S. Rabien, A. Ramírez, J. Ramos, C. Rau, M. Riquelme, R.-R. Rohloff, G. Rousset, J. Sanchez-Bermudez, S. Scheithauer, M. Schöller, N. Schuhler, J. Spyromilio, C. Straubmeier, E. Sturm, M. Suarez, K. R. W. Tristram, N. Ventura, F. Vincent, I. Waisberg, I. Wank, J. Weber, E. Wieprecht, M. Wiest, E. Wiezorrek, M. Wittkowski, J. Woillez, B. Wolff, S. Yazici, D. Ziegler, and G. Zins. First light for GRAVITY: Phase referencing optical interferometry for the Very Large Telescope Interferometer. *Astronomy & Astrophysics*, 602(1874):A94, June 2017. ISSN 0004-6361. doi: 10.1051/0004-6361/201730838.
- A. Guesalaga, B. Neichel, J. O’Neal, and D. Guzman. Mitigation of vibrations in adaptive optics by minimization of closed-loop residuals. *Optics Express*, 21(9):10676, May 2013. ISSN 1094-4087. doi: 10.1364/OE.21.010676.

Bibliography

- O. Guyon. Phase-induced amplitude apodization of telescope pupils for extrasolar terrestrial planet imaging. *Astronomy and Astrophysics*, 404(1):379–387, June 2003. ISSN 00046361. doi: 10.1051/0004-6361:20030457.
- S. Y. Haffert, R. J. Harris, A. Zanutta, F. A. Pike, A. Bianco, E. Redaelli, A. Benoît, D. G. MacLachlan, C. A. Ross, I. Gris-Sánchez, M. D. Trappen, Y. Xu, M. Blaicher, P. Maier, G. Riva, B. Siquin, C. Kulcsár, N. A. Bharmal, E. Gendron, L. Staykov, T. J. Morris, S. Barboza, N. Muench, L. Bardou, L. Prengère, H.-F. Raynaud, P. Hottinger, T. Anagnos, J. Osborn, C. Koos, R. R. Thomson, T. A. Birks, I. A. G. Snellen, and C. U. Keller. Diffraction-limited integral-field spectroscopy for extreme adaptive optics systems with the multicore fiber-fed integral-field unit. *Journal of Astronomical Telescopes, Instruments, and Systems*, 6(04):1–55, Dec. 2020. ISSN 2329-4124. doi: 10.1117/1.JATIS.6.4.045007.
- S. Halverson, A. Roy, S. Mahadevan, and C. Schwab. "Modal noise" in single-mode fibers: A cautionary note for high precision radial velocity instruments. *Astrophysical Journal Letters*, 814(2):L22, 2015. ISSN 20418213. doi: 10.1088/2041-8205/814/2/L22.
- C. R. Harris, K. J. Millman, S. J. van der Walt, R. Gommers, P. Virtanen, D. Cournapeau, E. Wieser, J. Taylor, S. Berg, N. J. Smith, R. Kern, M. Picus, S. Hoyer, M. H. van Kerkwijk, M. Brett, A. Haldane, J. F. del Río, M. Wiebe, P. Peterson, P. Gérard-Marchant, K. Sheppard, T. Reddy, W. Weckesser, H. Abbasi, C. Gohlke, and T. E. Oliphant. Array programming with NumPy. *Nature*, 585(7825):357–362, Sept. 2020. ISSN 0028-0836, 1476-4687. doi: 10.1038/s41586-020-2649-2.
- N. C. Harris, Y. Ma, J. Mower, T. Baehr-Jones, D. Englund, M. Hochberg, and C. Galland. Efficient, compact and low loss thermo-optic phase shifter in silicon. *Optics Express*, 22(9):10487, May 2014. ISSN 10944087. doi: 10.1364/oe.22.010487.
- R. J. Harris, L. Labadie, U. Lemke, D. G. MacLachlan, R. R. Thomson, S. Reffert, and A. Quirrenbach. Performance estimates for spectrographs using photonic reformatters. *Advances in Optical and Mechanical Technologies for Telescopes and Instrumentation II. Proc. SPIE*, 9912:99125Q, July 2016. ISSN 1996756X. doi: 10.1117/12.2232731.
- W. D. Heacox and P. Connes. Optical fibers in astronomical instruments. *The Astronomy and Astrophysics Review*, 3(3-4):169–199, 1992. ISSN 0935-4956, 1432-0754. doi: 10.1007/BF00872526.
- E. Hecht. *Optics, 4th Edition*. Addison-Wesley, New York, 2002. ISBN 978-0-8053-8566-3.
- P. Hinz, P. Arbo, V. Bailey, T. Connors, O. Durney, S. Esposito, W. Hoffmann, T. Jones, J. Leisenring, M. Montoya, M. Nash, M. Nelson, T. McMahon, E. Pinna, A. Puglisi, A. Skemer, M. Skrutskie, and V. Vaitheeswaran. First AO-corrected interferometry with LBTI: Steps towards routine coherent imaging observations. *Optical and Infrared Interferometry III*, 8445(September 2012):84450U, Sept. 2012. ISSN 0277786X. doi: 10.1117/12.926746.

- P. Hottinger, R. J. Harris, P.-I. Dietrich, M. Blaicher, M. Glück, A. Bechter, J.-U. Pott, O. Sawodny, A. Quirrenbach, J. Crass, and C. Koos. Micro-lens arrays as tip-tilt sensor for single mode fiber coupling. In R. Geyl and R. Navarro, editors, *Advances in Optical and Mechanical Technologies for Telescopes and Instrumentation III*, volume 1070629, page 77. SPIE, July 2018. ISBN 978-1-5106-1965-4. doi: 10.1117/12.2312015.
- P. Hottinger, R. J. Harris, P.-I. I. Dietrich, M. Blaicher, A. Bechter, J. Crass, M. Glück, J.-U. Pott, N. A. Bharmal, A. Basden, T. J. Morris, C. Koos, O. Sawodny, and A. Quirrenbach. Focal plane tip-tilt sensing for improved single-mode fiber coupling using a 3d-printed microlens-ring. In *Proceedings of AO4ELT6*, pages 1–7, Dec. 2019.
- P. Hottinger, R. J. Harris, J. Crass, P.-I. Dietrich, M. Blaicher, A. Bechter, B. Sands, T. Morris, A. G. Basden, N. A. Bharmal, J. Heidt, T. Anagnos, P. L. Neureuther, M. Glück, J. Power, J.-U. Pott, C. Koos, O. Sawodny, and A. Quirrenbach. On-sky results for the integrated microlens ring tip-tilt sensor. *JOSA B*, 38(9):2517–2527, Sept. 2021. ISSN 1520-8540. doi: 10.1364/JOSAB.421459.
- J. D. Hunter. Matplotlib: A 2D Graphics Environment. *Computing in Science and Engineering*, 9:90–95, May 2007. doi: 10.1109/MCSE.2007.55.
- N. Jovanovic, F. Martinache, O. Guyon, C. Clergeon, G. Singh, T. Kudo, V. Garrel, K. Newman, D. Doughty, J. Lozi, J. Males, Y. Minowa, Y. Hayano, N. Takato, J. Morino, J. Kuhn, E. Serabyn, B. Norris, P. Tuthill, G. Schworer, P. Stewart, L. Close, E. Huby, G. Perrin, S. Lacour, L. Gauchet, S. Vievard, N. Murakami, F. Oshiyama, N. Baba, T. Matsuo, J. Nishikawa, M. Tamura, O. Lai, F. Marchis, G. Duchene, T. Kotani, J. Woillez, U. O. F. The, and O. O. F. The. The Subaru Coronagraphic Extreme Adaptive Optics system: Enabling high-contrast imaging on solar-system scales. *Publications of the Astronomical Society of the Pacific*, 127(955): 890–910, 2015. ISSN 00046280. doi: 10.1086/682989.
- N. Jovanovic, N. Cvetojevic, B. Norris, C. Betters, C. Schwab, J. Lozi, O. Guyon, S. Gross, F. Martinache, P. Tuthill, D. Doughty, Y. Minowa, N. Takato, and J. Lawrence. Demonstration of an efficient, photonic-based astronomical spectrograph on an 8-m telescope. *arXiv*, 421(4):3641–3648, 2017a. ISSN 1094-4087. doi: 10.1051/0004-6361/201630351.18.
- N. Jovanovic, C. Schwab, O. Guyon, J. Lozi, N. Cvetojevic, F. Martinache, S. Leon-Saval, B. Norris, S. Gross, D. Doughty, T. Currie, and N. Takato. Efficient injection from large telescopes into single-mode fibres: Enabling the era of ultra-precision astronomy. *Astronomy and Astrophysics*, 604:A122, Aug. 2017b. ISSN 14320746. doi: 10.1051/0004-6361/201630351.
- N. Jovanovic, P. Gatkine, N. Anugu, R. Amezcuca-Correa, R. B. Thakur, C. Beichman, C. Bender, J.-P. Berger, A. Bigioli, J. Bland-Hawthorn, G. Bourdarot, C. M. Bradford, R. Broeke, J. Bryant, K. Bundy, R. Cheriton, N. Cvetojevic, M. Diab, S. A. Diddams, A. N. Dinkelaker, J. Duis, S. Eikenberry, S. Ellis, A. Endo, D. F. Figer, M. Fitzgerald,

Bibliography

- I. Gris-Sanchez, S. Gross, L. Grossard, O. Guyon, S. Y. Haffert, S. Halverson, R. J. Harris, J. He, T. Herr, P. Hottinger, E. Huby, M. Ireland, R. Jenson-Clem, J. Jewell, L. Jocou, S. Kraus, L. Labadie, S. Lacour, R. Laugier, K. Lawniczuk, J. Lin, S. Leifer, S. Leon-Saval, G. Martin, F. Martinache, M.-A. Martinod, B. A. Mazin, S. Minardi, J. D. Monnier, R. Moreira, D. Mourard, A. S. Nayak, B. Norris, E. Obrzud, K. Perraut, F. Reynaud, S. Sallum, D. Schiminovich, C. Schwab, E. Serbayn, S. Soliman, A. Stoll, L. Tang, P. Tuthill, K. Vahala, G. Vasisht, S. Veilleux, A. B. Walter, E. J. Wollack, Y. Xn, Z. Yang, S. Yerolatsitis, Y. Zhang, and C.-L. Zou. 2023 Astrophotonics Roadmap: Pathways to realizing multi-functional integrated astrophotonic instruments. *J. Phys. Photonics*, 2023, under review.
- A. Kolmogorov. The Local Structure of Turbulence in Incompressible Viscous Fluid for Very Large Reynolds' Numbers. *Akademiia Nauk SSSR Doklady*, 30:301–305, Jan. 1941. ISSN 0002-3264.
- T. Kotani, M. Tamura, H. Suto, J. Nishikawa, A. Ueda, M. Kuzuhara, M. Omiya, J. Hashimoto, T. Kurokawa, T. Kokubo, T. Mori, Y. Tanaka, M. Konishi, T. Kudo, T. Hirano, B. Sato, S. Jacobson, K. Hodapp, D. Hall, M. Ishizuka, H. Kawahara, Y. Ikeda, T. Yamamuro, H. Ishikawa, K. Hosokawa, N. Kusakabe, J.-I. Morino, S. Nishiyama, N. Jovanovic, W. Aoki, T. Usuda, N. Narita, E. Kokubo, Y. Hayano, H. Izumiura, E. Kambe, M. Ikoma, Y. Hori, H. Genda, A. Fukui, Y. Fujii, H. Harakawa, M. Hayashi, M. Hidai, M. Machida, T. Matsuo, T. Nagata, M. Ogi-hara, H. Takami, N. Takato, H. Terada, J. Kwon, D. Oh, K. Kashiwagi, T. Nakajima, H. Baba, and G. Olivier. The infrared Doppler (IRD) instrument for the Subaru telescope: Instrument description and commissioning results. *Ground-based and Airborne Instrumentation for Astronomy VII*, 1070211(July 2018):37, July 2018. ISSN 1996756X. doi: 10.1117/12.2311836.
- L. Labadie. A report on the status of astrophotonics for optical/IR interferometry and beyond. In A. Mérand, S. Sallum, and J. Sanchez-Bermudez, editors, *Optical and Infrared Interferometry and Imaging VIII*, page 38. SPIE, Aug. 2022. ISBN 978-1-5106-5347-4. doi: 10.1117/12.2635904.
- J.-B. Le Bouquin, J.-P. Berger, B. Lazareff, G. Zins, P. Haguenaer, L. Jocou, P. Kern, R. Millan-Gabet, W. Traub, O. Absil, J.-C. Augereau, M. Benisty, N. Blind, X. Bonfils, P. Bourget, A. Delboulbe, P. Feautrier, M. Germain, P. Gitton, D. Gillier, M. Kieckebusch, J. Kluska, J. Knudstrup, P. Labeye, J.-L. Lizon, J.-L. Monin, Y. Magnard, F. Malbet, D. Maurel, F. Ménard, M. Micallef, L. Michaud, G. Montagnier, S. Morel, T. Moulin, K. Perraut, D. Popovic, P. Rabou, S. Rochat, C. Rojas, F. Roussel, A. Roux, E. Stadler, S. Stefl, E. Tatulli, and N. Ventura. PIONIER: A 4-telescope visitor instrument at VLTI. *Astronomy & Astrophysics*, 535:A67, Nov. 2011. ISSN 0004-6361, 1432-0746. doi: 10.1051/0004-6361/201117586.
- D. Lee and J. R. Allington-Smith. An experimental investigation of immersed gratings. *Monthly Notices of the Royal Astronomical Society*, 312(1):57–69, Feb. 2000. ISSN 0035-8711. doi: 10.1046/j.1365-8711.2000.03151.x.

- M. Lippa, S. Gillessen, N. Blind, Y. Kok, Ş. Yazıcı, J. Weber, O. Pfuhl, M. Haug, S. Kellner, E. Wieprecht, F. Eisenhauer, R. Genzel, O. Hans, F. Haußmann, D. Huber, T. Kratschmann, T. Ott, M. Plattner, C. Rau, E. Sturm, I. Waisberg, E. Wiezorrek, G. Perrin, K. Perraut, W. Brandner, C. Straubmeier, and A. Amorim. The metrology system of the VLTI instrument GRAVITY. *Optical and Infrared Interferometry and Imaging V*, 9907:990722, Aug. 2016. ISSN 1996756X. doi: 10.1117/12.2232272.
- J. Lozi, O. Guyon, N. Jovanovic, S. Goebel, P. Pathak, N. Skaf, A. Sahoo, B. Norris, F. Martinache, M. M'Diaye, B. A. Mazin, A. Walter, P. Tuthill, T. Kudo, H. Kawahara, T. Kotani, M. Ireland, N. Cvetojevic, E. Huby, S. Lacour, S. Vievard, T. D. Groff, J. K. Chilcote, J. Kasdin, J. Knight, Y. Minowa, C. Clergeon, N. Takato, M. Tamura, T. Currie, H. Takami, M. Hayashi, F. Snik, and D. Doelman. SCEXAO, an instrument with a dual purpose: Perform cutting-edge science and develop new technologies. In D. Schmidt, L. Schreiber, and L. M. Close, editors, *Adaptive Optics Systems VI*, number July, page 270. SPIE, July 2018a. ISBN 978-1-5106-1959-3. doi: 10.1117/12.2314282.
- J. Lozi, O. Guyon, N. Jovanovic, N. Takato, G. Singh, B. Norris, H. Okita, T. Bando, and F. Martinache. Characterizing vibrations at the Subaru Telescope for the Subaru coronagraphic extreme adaptive optics instrument. *Journal of Astronomical Telescopes, Instruments, and Systems*, 4(04):1, 2018b. ISSN 23294221. doi: 10.1117/1.jatis.4.4.049001.
- B. Macintosh, J. R. Graham, P. Ingraham, Q. Konopacky, C. Marois, M. Perrin, L. Poyneer, B. Bauman, T. Barman, A. S. Burrows, A. Cardwell, J. Chilcote, R. J. De Rosa, D. Dillon, R. Doyon, J. Dunn, D. Erikson, M. P. Fitzgerald, D. Gavel, S. Goodsell, M. Hartung, P. Hibon, P. Kalas, J. Larkin, J. Maire, F. Marchis, M. S. Marley, J. McBride, M. Millar-Blanchaer, K. Morzinski, A. A. A. Norton, B. R. Oppenheimer, D. D. D. D. Palmer, J. Patience, L. Pueyo, F. Rantakyro, N. Sadakuni, L. Saddlemyer, D. Savransky, A. Serio, R. Soummer, A. Sivaramakrishnan, I. Song, S. Thomas, J. K. Wallace, S. Wiktorowicz, S. Wolff, R. J. D. Rosa, D. Dillon, R. Doyon, J. Dunn, D. Erikson, M. P. Fitzgerald, D. Gavel, S. Goodsell, M. Hartung, P. Hibon, P. Kalas, J. Larkin, J. Maire, F. Marchis, M. S. Marley, J. McBride, M. Millar-Blanchaer, K. Morzinski, A. A. A. Norton, B. R. Oppenheimer, D. D. D. D. Palmer, J. Patience, L. Pueyo, F. Rantakyro, N. Sadakuni, L. Saddlemyer, D. Savransky, A. Serio, R. Soummer, A. Sivaramakrishnan, I. Song, S. Thomas, J. K. Wallace, S. Wiktorowicz, and S. Wolff. First light of the Gemini Planet Imager. *Proceedings of the National Academy of Sciences of the United States of America*, 111(35):12661–12666, Sept. 2014. ISSN 10916490. doi: 10.1073/pnas.1304215111.

Bibliography

- M. A. Martinod, D. Mourard, P. B erio, K. Perraut, A. Meilland, C. Bailet, Y. Bresson, T. ten Brummelaar, J. M. Clausse, J. Dejonghe, M. Ireland, F. Millour, J. D. Monnier, J. Sturmman, L. Sturmman, and M. Tallon. Fibered visible interferometry and adaptive optics: FRIEND at CHARA. *Astronomy & Astrophysics*, 618:A153, Oct. 2018. ISSN 0004-6361, 1432-0746. doi: 10.1051/0004-6361/201731386.
- D. Mawet, P. Wizinowich, R. Dekany, M. Chun, D. Hall, S. Cetre, O. Guyon, J. K. Wallace, B. Bowler, M. Liu, G. Ruane, E. Serabyn, R. Bartos, J. Wang, G. Vasisht, M. Fitzgerald, A. Skemer, M. Ireland, J. Fucik, J. Fortney, I. Crossfield, R. Hu, and B. Benneke. Keck Planet Imager and Characterizer: Concept and phased implementation. In E. Marchetti, L. M. Close, and J.-P. V eran, editors, *Adaptive Optics Systems V*, volume 9909, page 99090D, July 2016. ISBN 978-1-5106-0197-0. doi: 10.1117/12.2233658.
- J. Milli, D. Mouillet, J.-L. Beuzit, J.-F. Sauvage, T. Fusco, P. Bourget, M. Kasper, K. Tristram, C. Reyes, J. H. Girard, A. Telle, C. Pannetier, F. Cantalloube, Z. Wahhaj, D. Mawet, A. Vigan, and M. N'Diaye. Low wind effect on VLT/SPHERE: Impact, mitigation strategy, and results. In D. Schmidt, L. Schreiber, and L. M. Close, editors, *Adaptive Optics Systems VI*, page 83. SPIE, July 2018. ISBN 978-1-5106-1959-3. doi: 10.1117/12.2311499.
- S. Minardi, R. J. Harris, and L. Labadie. Astrophotonics: Astronomy and modern optics. *The Astronomy and Astrophysics Review*, 29(1):6, Dec. 2021. ISSN 0935-4956. doi: 10.1007/s00159-021-00134-7.
- F. Mitschke. *Fiber Optics*. Springer Berlin Heidelberg, Berlin, Heidelberg, 2016. ISBN 978-3-662-52762-7. doi: 10.1007/978-3-662-52764-1.
- Nanoscribe. Nanoscribe GmbH & Co. KG. www.nanoscribe.com.
- R. J. Noll. Zernike polynomials and atmospheric turbulence. *JOSA*, 66:207–211, 1976. ISSN 0030-3941.
- B. Norris and J. Bland-hawthorn. Astrophotonics - The Rise of Integrated Photonics in Astronomy. (May):26–33, 2019.
- B. Norris, J. Wei, C. Betters, A. Wong, and S. Leon-Saval. All-fibre focal-plane wavefront sensor. In *14th Pacific Rim Conference on Lasers and Electro-Optics (CLEO PR 2020)*, page PDP1, Washington, D.C., 2020a. Optica Publishing Group. ISBN 978-0-646-82504-5. doi: 10.1364/CLEOPR.2020.PDP_1.
- B. R. M. Norris, N. Cvetojevic, T. Lagadec, N. Jovanovic, S. Gross, A. Arriola, T. Gretzinger, M.-A. Martinod, O. Guyon, J. Lozi, M. J. Withford, J. S. Lawrence, and P. Tuthill. First on-sky demonstration of an integrated-photonics nulling interferometer: The GLINT instrument. *Monthly Notices of the Royal Astronomical Society*, 491(3):4180–4193, Jan. 2020b. ISSN 0035-8711. doi: 10.1093/mnras/stz3277.

- B. R. M. Norris, J. Wei, C. H. Betters, A. Wong, and S. G. Leon-Saval. An all-photonic focal-plane wavefront sensor. *Nature Communications*, 11(1):5335, Dec. 2020c. ISSN 2041-1723. doi: 10.1038/s41467-020-19117-w.
- I. R. Parry. The Astronomical Uses of Optical Fibers. In *Fiber Optics in Astronomy III*, volume 152, page 3, 1998. ISBN 1-886733-72-4.
- F. A. Pepe, S. Cristiani, R. Rebolo Lopez, N. C. Santos, A. Amorim, G. Avila, W. Benz, P. Bonifacio, A. Cabral, P. Carvas, R. Cirami, J. Coelho, M. Comari, I. Coretti, V. De Caprio, H. Dekker, B. Delabre, P. Di Marcantonio, V. D’Odorico, M. Fleury, R. García, J. M. Herreros Linares, I. Hughes, O. Iwert, J. Lima, J.-L. Lizon, G. Lo Curto, C. Lovis, A. Manescau, C. Martins, D. Mégevand, A. Moitinho, P. Molaro, M. Monteiro, M. Monteiro, L. Pasquini, C. Mordasini, D. Queloz, J. L. Rasilla, J. M. Rebordão, S. Santana Tschudi, P. Santin, D. Sosnowska, P. Spanò, F. Tenegi, S. Udry, E. Vanzella, M. Viel, M. R. Zapatero Osorio, and F. Zerbi. ESPRESSO: The Echelle spectrograph for rocky exoplanets and stable spectroscopic observations. In I. S. McLean, S. K. Ramsay, and H. Takami, editors, *SPIE Astronomical Telescopes + Instrumentation*, page 77350F, San Diego, California, USA, July 2010. doi: 10.1117/12.857122.
- C. Petit, J.-M. Conan, C. Kulcsár, H.-F. Raynaud, and T. Fusco. First laboratory validation of vibration filtering with LQG control law for Adaptive Optics. *Optics Express*, 16(1):87, Jan. 2008. ISSN 1094-4087. doi: 10.1364/OE.16.000087.
- C. Petit, J.-F. Sauvage, T. Fusco, A. Sevin, M. Suarez, A. Costille, A. Vigan, C. Soenke, D. Perret, S. Rochat, A. Barrufolo, B. Salasnich, J.-L. Beuzit, K. Dohlen, D. Mouillet, P. Puget, F. Wildi, M. Kasper, J.-M. Conan, C. Kulcsár, and H.-F. Raynaud. SPHERE eXtreme AO control scheme: Final performance assessment and on sky validation of the first auto-tuned LQG based operational system. In E. Marchetti, L. M. Close, and J.-P. Véran, editors, *Adaptive Optics Systems IV*, volume 9148, page 91480O. SPIE, Aug. 2014. ISBN 978-0-8194-9616-4. doi: 10.1117/12.2052847.
- F. A. Pike, A. Benoît, D. G. MacLachlan, R. J. Harris, I. Gris-Sánchez, D. Lee, T. A. Birks, and R. R. Thomson. Modal noise mitigation for high-precision spectroscopy using a photonic reformatter. *Monthly Notices of the Royal Astronomical Society*, 497(3):3713–3725, Sept. 2020. ISSN 0035-8711. doi: 10.1093/mnras/staa1950.
- E. Pinna, S. Esposito, P. Hinz, G. Agapito, M. Bonaglia, A. Puglisi, M. Xompero, A. Riccardi, R. Briguglio, C. Arcidiacono, L. Carbonaro, L. Fini, M. Montoya, and O. Durney. SOUL: The Single conjugated adaptive Optics Upgrade for LBT. In E. Marchetti, L. M. Close, and J.-P. Véran, editors, *Adaptive Optics Systems V*, volume 9909, page 99093V, July 2016. ISBN 978-1-5106-0197-0. doi: 10.1117/12.2234444.
- E. H. Por and S. Y. Haffert. The Single-mode Complex Amplitude Refinement (SCAR) coronagraph. *Astronomy & Astrophysics*, 635(Guyon 2005):A55, Mar. 2020. ISSN 0004-6361. doi: 10.1051/0004-6361/201731616.

Bibliography

- E. H. Por, S. Y. Haffert, V. M. Radhakrishnan, D. S. Doelman, M. van Kooten, and S. Bos. High Contrast Imaging for Python (HCIPy): An open-source adaptive optics and coronagraph simulator. In D. Schmidt, L. Schreiber, and L. M. Close, editors, *Adaptive Optics Systems VI*, page 152, Austin, United States, July 2018. SPIE. ISBN 978-1-5106-1959-3 978-1-5106-1960-9. doi: 10.1117/12.2314407.
- L. A. Poyneer, D. W. Palmer, B. Macintosh, D. Savransky, N. Sadakuni, S. Thomas, J.-P. Véran, K. B. Follette, A. Z. Greenbaum, S. Mark Ammons, V. P. Bailey, B. Bauman, A. Cardwell, D. Dillon, D. Gavel, M. Hartung, P. Hibon, M. D. Perrin, F. T. Rantakyö, A. Sivaramakrishnan, and J. J. Wang. Performance of the Gemini Planet Imager’s adaptive optics system. *Applied Optics*, 55(2):323, Jan. 2016. ISSN 0003-6935. doi: 10.1364/AO.55.000323.
- H. M. Presby, A. F. Benner, and C. A. Edwards. Laser micromachining of efficient fiber microlenses. *Applied Optics*, 29(18):2692–2695, June 1990. ISSN 2155-3165. doi: 10.1364/AO.29.002692.
- F. Rigaut. Astronomical Adaptive Optics. *Publications of the Astronomical Society of the Pacific*, 127(958):1197–1203, Dec. 2015. ISSN 00046280. doi: 10.1086/684512.
- F. Roddier. Adaptive optics in astronomy. *aoa*, 1999.
- T. J. Rodigas, K. B. Follette, A. Weinberger, L. Close, and D. C. Hines. Polarized Light Imaging of the Hd 142527 Transition Disk With the Gemini Planet Imager: Dust Around the Close-in Companion. *The Astrophysical Journal*, 791(2):L37, 2014. ISSN 2041-8213. doi: 10.1088/2041-8205/791/2/L37.
- S. Rodriguez, A. Rakich, J. Hill, O. Kuhn, T. Brendel, C. Veillet, D. W. Kim, and H. Choi. Implementation of a laser-truss based telescope metrology system at the Large Binocular Telescope. In R. Rascher and D. W. Kim, editors, *Optical Manufacturing and Testing XIII*, page 58. SPIE, Aug. 2020. ISBN 978-1-5106-3780-1. doi: 10.1117/12.2576438.
- C. Ruilier. Degraded light coupling into single-mode fibers. In R. D. Reasenberg, editor, *Astronomical Interferometry*, volume 3350, page 319, July 1998. doi: 10.1117/12.317094.
- C. Ruilier and F. Cassaing. Coupling of large telescopes and single-mode waveguides: Application to stellar interferometry. *Journal of the Optical Society of America A*, 18(1):143, Jan. 2001. ISSN 1084-7529. doi: 10.1364/JOSAA.18.000143.
- S. Shaklan and F. Roddier. Coupling starlight into single-mode fiber optics. *Applied Optics*, 27(11):2334, June 1988. ISSN 0003-6935. doi: 10.1364/AO.27.002334.
- G. Sivo, C. Kulcsár, J.-M. Conan, H.-F. Raynaud, É. Gendron, A. Basden, F. Vidal, T. Morris, S. Meimon, C. Petit, D. Gratadour, O. Martin, Z. Hubert, A. Sevin, D. Perret, F. Chemla, G. Rousset, N. Dipper, G. Talbot, E. Younger, R. Myers, D. Henry,

- S. Todd, D. Atkinson, C. Dickson, and A. Longmore. First on-sky SCAO validation of full LQG control with vibration mitigation on the CANARY pathfinder. *Optics Express*, 22(19):23565, Sept. 2014. ISSN 1094-4087. doi: 10.1364/OE.22.023565.
- J. Stürmer, A. Seifahrt, C. Schwab, and J. L. Bean. Rubidium-traced white-light etalon calibrator for radial velocity measurements at the cm s^{-1} level. *Journal of Astronomical Telescopes, Instruments, and Systems*, 3(2):025003, June 2017. ISSN 2329-4124. doi: 10.1117/1.JATIS.3.2.025003.
- Szu-Ming Yeh, Sun-Yuan Huang, and Wood-Hi Cheng. A new scheme of conical-wedge-shaped fiber endface for coupling between high-power laser diodes and single-mode fibers. *Journal of Lightwave Technology*, 23(4):1781–1786, Apr. 2005. ISSN 0733-8724. doi: 10.1109/JLT.2005.844511.
- V. I. Tatarski, R. A. Silverman, and N. Chako. Wave Propagation in a Turbulent Medium. *Physics Today*, 14:46, Jan. 1961. ISSN 0031-9228. doi: 10.1063/1.3057286.
- The Astropy Collaboration, T. P. Robitaille, E. J. Tollerud, P. Greenfield, M. Droettboom, E. Bray, T. Aldcroft, M. Davis, A. Ginsburg, A. M. Price-Whelan, W. E. Kerzendorf, A. Conley, N. Crighton, K. Barbary, D. Muna, H. Ferguson, F. Grollier, M. M. Parikh, P. H. Nair, H. M. Günther, C. Deil, J. Woillez, S. Conseil, R. Kramer, J. E. H. Turner, L. Singer, R. Fox, B. A. Weaver, V. Zabalza, Z. I. Edwards, K. Azalee Bostroem, D. J. Burke, A. R. Casey, S. M. Crawford, N. Dencheva, J. Ely, T. Jenness, K. Labrie, P. L. Lim, F. Pierfederici, A. Pontzen, A. Ptak, B. Refsdal, M. Servillat, and O. Streicher. Astropy: A community Python package for astronomy. *Astronomy & Astrophysics*, 558:A33, Oct. 2013. ISSN 0004-6361, 1432-0746. doi: 10.1051/0004-6361/201322068.
- The Astropy Collaboration, A. M. Price-Whelan, B. M. Sipócz, H. M. Günther, P. L. Lim, S. M. Crawford, S. Conseil, D. L. Shupe, M. W. Craig, N. Dencheva, A. Ginsburg, J. T. VanderPlas, L. D. Bradley, D. Pérez-Suárez, M. de Val-Borro, (Primary Paper Contributors), T. L. Aldcroft, K. L. Cruz, T. P. Robitaille, E. J. Tollerud, (Astropy Coordination Committee), C. Ardelean, T. Babej, Y. P. Bach, M. Bachetti, A. V. Bakanov, S. P. Bamford, G. Barentsen, P. Barmby, A. Baumbach, K. L. Berry, F. Biscani, M. Boquien, K. A. Bostroem, L. G. Bouma, G. B. Brammer, E. M. Bray, H. Breytenbach, H. Buddelmeijer, D. J. Burke, G. Calderone, J. L. C. Rodríguez, M. Cara, J. V. M. Cardoso, S. Cheedella, Y. Copin, L. Corrales, D. Crighton, D. D’Avella, C. Deil, É. Depagne, J. P. Dietrich, A. Donath, M. Droettboom, N. Earl, T. Erben, S. Fabbro, L. A. Ferreira, T. Finethy, R. T. Fox, L. H. Garrison, S. L. J. Gibbons, D. A. Goldstein, R. Gommers, J. P. Greco, P. Greenfield, A. M. Groener, F. Grollier, A. Hagen, P. Hirst, D. Homeier, A. J. Horton, G. Hosseinzadeh, L. Hu, J. S. Hunkeler, Ž. Ivezić, A. Jain, T. Jenness, G. Kanarek, S. Kendrew, N. S. Kern, W. E. Kerzendorf, A. Khvalko, J. King, D. Kirkby, A. M. Kulkarni, A. Kumar, A. Lee, D. Lenz, S. P. Littlefair, Z. Ma, D. M. Macleod, M. Mastropietro, C. McCully, S. Montagnac, B. M. Morris, M. Mueller, S. J. Mumford, D. Muna, N. A. Murphy,

Bibliography

- S. Nelson, G. H. Nguyen, J. P. Ninan, M. Nöthe, S. Ogaz, S. Oh, J. K. Parejko, N. Parley, S. Pascual, R. Patil, A. A. Patil, A. L. Plunkett, J. X. Prochaska, T. Rastogi, V. R. Janga, J. Sabater, P. Sakurikar, M. Seifert, L. E. Sherbert, H. Sherwood-Taylor, A. Y. Shih, J. Sick, M. T. Silbiger, S. Singanamalla, L. P. Singer, P. H. Sladen, K. A. Sooley, S. Sornarajah, O. Streicher, P. Teuben, S. W. Thomas, G. R. Tremblay, J. E. H. Turner, V. Terrón, M. H. van Kerkwijk, A. de la Vega, L. L. Watkins, B. A. Weaver, J. B. Whitmore, J. Woillez, V. Zabalza, and (Astropy Contributors). The Astropy Project: Building an Open-science Project and Status of the v2.0 Core Package. *The Astronomical Journal*, 156(3):123, Aug. 2018. ISSN 1538-3881. doi: 10.3847/1538-3881/aabc4f.
- G. A. Tyler and D. L. Fried. Image-Position Error Associated With a Quadrant Detector. *Journal of the Optical Society of America*, 72(6):804–808, 1982. ISSN 00303941. doi: 10.1364/JOSA.72.000804.
- A. Vigan, J.-L. Beuzit, K. Dohlen, D. Mouillet, G. Otten, E. Muslimov, M. Philipps, R. Dorn, M. Kasper, I. Baraffe, A. Reiners, and U. Seemann. Bringing high-spectral resolution to VLT/SPHERE with a fiber coupling to VLT/CRIRES+. In H. Takami, C. J. Evans, and L. Simard, editors, *Ground-Based and Airborne Instrumentation for Astronomy VII*, page 115. SPIE, July 2018. ISBN 978-1-5106-1957-9. doi: 10.1117/12.2313681.
- T. A. Wright, S. Yerolatsitis, K. Harrington, R. J. Harris, and T. A. Birks. All-fibre wavefront sensor. *Monthly Notices of the Royal Astronomical Society*, 514(4):5422–5428, July 2022. ISSN 0035-8711. doi: 10.1093/mnras/stac1658.
- T. Young. I. The Bakerian Lecture. Experiments and calculations relative to physical optics. *Philosophical Transactions of the Royal Society of London*, 94:1–16, Dec. 1804. ISSN 0261-0523. doi: 10.1098/rstl.1804.0001.
- Zemax-OpticStudio. Zemax OpticStudio. www.zemax.com.